Università degli Studi di Palermo

AREA RICERCA E TRASFERIMENTO TECNOLOGICO
SETTORE DOTTORATI E CONTRATTI PER LA RICERCA
U. O. DOTTORATI DI RICERCA

PhD Course of Biomedicine Neuroscience and Advanced Diagnostic

Department of Biomedicine Neuroscience and Advanced Diagnostic

SSD: BIO/16

ENGINEERING THERMOPLASTIC ORGAN-ON-CHIP PLATFORM FOR RELIABLE IN-VITRO MODELLING

PhD STUDENT

Dr. MARIA TESTA

THE COORDINATOR

Dr. FABIO BUCCHIERI

TUTOR

Dr. FABIO BUCCHIERI

CO TUTOR

Dr. VINCENZO LA CARRUBBA

CYCLE XXXVIII

ACADEMIC YEAR 2024/2025

Πάντες ἄνθρωποι τοῦ εἰδέναι ὀρέγονται φύσει.

All men by nature strive for knowledge.
— *Aristotle, Metaphysics* I, 1

INDEX

ABSTRACT

The drug discovery pipeline remains one of the most resource-intensive and failure-prone processes in biomedical research. Despite unprecedented advances in genomics and high-throughput screening, more than 80% of drug candidates still fail during clinical development, predominantly due to lack of efficacy or unexpected toxicity. Traditional two-dimensional (2D) cultures lack the physiological complexity of native tissues, while animal models are limited by interspecies differences, high costs, and ethical concerns. These limitations underscore the urgent need for predictive *in vitro* models that can recapitulate the cellular and microenvironmental dynamics of human organs. In this context, Organ-on-Chip (OoC) technologies are emerging as powerful alternatives, integrating microfluidics, biomaterials, and tissue engineering to provide dynamic, reproducible, and physiologically relevant platforms for drug testing and disease modelling.

This doctoral research aimed to design, fabricate, and validate a new generation of OoC devices based on thermoplastic polymers, specifically polymethyl methacrylate (PMMA), combined with electrospun polylactic acid (PLA) scaffolds and hydrogels. The integration of scaffolds into microfluidic devices was conceived to mimic extracellular matrix–like properties, enabling long-term co-cultures, guiding cell morphology, and supporting physiologically relevant responses under flow. Importantly, the choice of thermoplastics—widely used in biomedical devices—addresses key translational challenges of PDMS-based devices, including small-molecule absorption, poor scalability, and lack of regulatory compatibility.

The fabrication workflow was centered on rapid prototyping via CO_2 laser micromachining and multilayer thermal bonding. Process parameters were systematically optimized to preserve PMMA transparency, minimize thermal damage, and ensure robust sealing with commercial microfluidic connectors. Electrospun PLA scaffolds with either random or aligned architectures were integrated as culture substrates. Structural, thermal, and surface analyses demonstrated that scaffold morphology and porosity were largely preserved post-bonding, while fiber alignment provided a tunable handle on mechanical and biological properties. Plasma treatments further enhanced hydrophilicity and scaffold–device integration.

Three proof-of-concept applications were developed and validated:

I. **Liver-on-Chip (LoC)**: a dual-chamber device for studying chronic, low-dose exposure of hepatocytes to tumor-derived extracellular vesicles. The platform recapitulated key features of pre-metastatic niche formation, with hepatocytes acquiring mesenchymal-like traits under continuous vesicle perfusion, highlighting its potential for modelling tumor–organ cross-talk.

II. **Tumor-on-Chip (ToC)**: a breast cancer model integrating stromal fibroblasts to investigate tumor–stroma interactions and therapeutic resistance. The system reproduced the protective role of CAFs against olaparib–dinaciclib treatment, consistent with *in vivo* xenograft data, thereby validating its translational relevance for preclinical oncology.

III. **Brain-on-Chip (BoC)**: a platform designed to study selective drug–cell interactions in neural co-cultures. By combining neuronal and microglial cells on scaffold substrates, the BoC demonstrated selective uptake of myelin-derived nanovesicles by microglia under physiologically relevant flow, providing a new tool for neuropharmacological research.

IV. **ISO-compliant dual-scaffold platform** – a multilayer thermoplastic microfluidic device designed according to ISO 22916:2022 standards for microfluidic interoperability. The system integrates an aligned electrospun PLA membrane and an *in situ* ionically crosslinked alginate hydrogel within a single architecture, enabling the co-culture of endothelial and tumor cells under controlled conditions. The device demonstrated excellent structural integrity, hydrogel confinement, and cellular viability over 72 hours, establishing a foundation for scalable, standardized OoC manufacturing and regulatory translation.

Taken together, these projects establish thermoplastic, scaffold-integrated OoC platforms as versatile and reproducible systems for modelling organ-specific physiology and pathology. From an engineering perspective, the workflow—based on rapid prototyping, commercial connectors, and scalable materials—addresses critical challenges of standardization and industrial translation. From a biological standpoint, the integration of PLA scaffolds provided an extracellular matrix–like environment that preserved morphology, promoted co-culture interactions, and enabled physiologically relevant readouts.

This work contributes to the broader effort of aligning OoC development with international standards (ISO 23494, ISO 10993, CEN/CENELEC FGOoC roadmap),

fostering reproducibility, interoperability, and regulatory adoption. By bridging static 2D assays, animal models, and clinically relevant outcomes, the proposed platforms advance the case for OoCs as predictive preclinical tools. Future directions include the incorporation of primary and iPSC-derived cells, integration of vascular and immune compartments, coupling to multi-organ systems for PK/PD studies, and embedding real-time sensors for quantitative monitoring.

In conclusion, this thesis demonstrates that scaffold-integrated thermoplastic Organ-on-Chip systems represent a significant step forward in preclinical research, offering scalable, ethical, and physiologically meaningful alternatives to animal testing. By combining engineering innovation with biological validation, these platforms pave the way for more predictive drug discovery pipelines and personalized therapeutic strategies.

1 Introduction

The escalating demand for more representative and predictive models in pharmacological and toxicological research has propelled researcher to develop innovative microfluidic platforms promising a more accurate comprehension of organ-level responses to diverse stimuli, drugs, and diseases [1]. Drug discovery and development is a long, complex, and costly process that remains characterized by high attrition rates despite technological progress in biomedical research. On average, the development of a new molecular entity requires more than a decade of research and billions of dollars in investment, yet the probability of success from the initial discovery phase to market approval remains strikingly low [2].

The drug development pipeline typically progresses through sequential stages starting from preclinical research, Phase I–III clinical trials (Phase I), regulatory submission (Phase II), and post-marketing surveillance (Phase III). However, each stage is associated with significant attrition.

A landmark study by Hay et al. (2014), which analysed over 4,000 compounds and 7,300 development paths, reported that only 10.4% of drug candidates entering Phase I trials ultimately achieved FDA approval [3]. Success rates differ markedly by phase: approximately 64% of drugs advance from Phase I to Phase II, but only 32% succeed in Phase II, which is widely considered the most challenging stage due to the need to demonstrate therapeutic efficacy in larger patient populations. Phase III shows moderately higher success (around 60%), while the likelihood of FDA approval after submission of a New Drug Application or Biologic License Application (BLA) reaches 83%.

Overall, however, more than 80% of investigational drugs still fail during clinical testing, with approximately 60% of these failures attributable to lack of efficacy and nearly 30% to safety and toxicity issues (Figure 1).

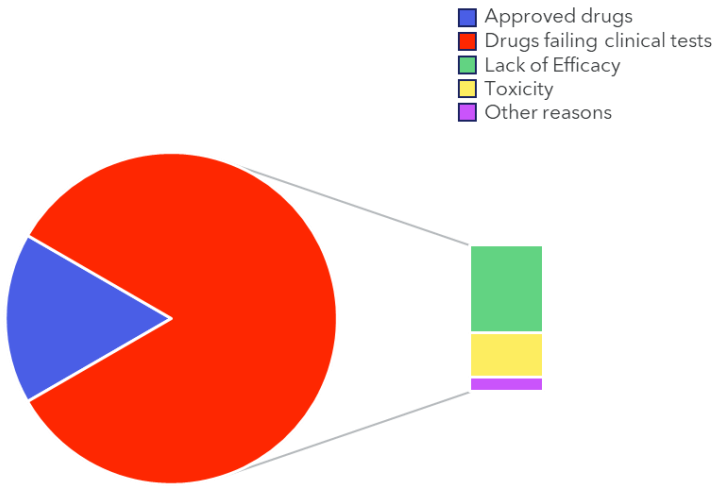

Figure 1 Clinical trial outcomes for investigational drugs. The vast majority of drug candidates fail during clinical testing, with only ~10–20% ultimately receiving FDA approval. Among failed compounds, approximately 60% are discontinued due to lack of efficacy, 30% due to toxicity, and the remainder for other reasons (e.g., pharmacokinetics or commercial viability).

Despite continuous growth in biomedical knowledge and technological advances, R&D productivity has paradoxically declined. Since the sequencing of the human genome, the number of compounds in development has increased by 62% and R&D expenditures have doubled, yet the annual number of approved new drugs has not increased proportionally. This phenomenon, often referred to as *Eroom's Law* (the inverse of Moore's Law), highlights that drug discovery is becoming slower and more expensive over time. DiMasi et al. (2016) estimated that the average cost of developing a single approved drug exceeds $2.6 billion, when accounting for both direct costs and the high rate of failure across the pipeline [4].

The economic inefficiency of drug discovery is further underscored by therapeutic area–specific disparities. Oncology, for instance, exhibits the lowest likelihood of approval, with only 6.7% of cancer drugs entering Phase I eventually receiving FDA approval, reflecting both the biological complexity of tumors and the limitations of current preclinical models [5] [6]. By contrast, infectious disease [7] and cardiovascular drugs [8] show comparatively higher success probabilities.

Taken together, these findings emphasize the urgent need for more predictive preclinical models that can bridge the translational gap between bench research and human clinical outcomes. The high cost and low efficiency of the current drug discovery paradigm provide a strong rationale for the exploration of innovative *in vitro* approaches, such as three-

dimensional (3D) cell culture and **Organ on Chip (OoC)** technologies, that aim to reduce late-stage failures and accelerate the delivery of effective therapies to patients.

These discrepancies markedly reduce the predictive value of 2D models in drug discovery and translational medicine, thereby reinforcing the need for more physiologically relevant 3D culture systems. Animal models, on the other hand, provide the advantage of systemic physiology but still fail to reproduce human-specific responses due to interspecies differences. Moreover, they are costly, ethically debated, and characterized by low throughput, further underscoring the necessity of alternative approaches [9]. To address these limitations and, at the same time, to enable the recreation of functional organs and tissues, several types of 3D models have been developed:

Multicellular spheroids spontaneously aggregate into spherical clusters where gradients of oxygen, nutrients, and metabolites generate proliferative, quiescent, and necrotic zones, thereby closely mimicking the physiology of solid tumors [10] [11].

Organoids, derived from stem cells or patient biopsies, recapitulate tissue organization and heterogeneity, offering powerful tools for disease modelling and personalized medicine. However, they often lack vascularization and still suffer from limited reproducibility [12] [13].

Engineered scaffolds, fabricated from natural or synthetic biomaterials, enable precise control over elasticity, porosity, and architecture, guiding cell adhesion and differentiation. Nonetheless, they still face challenges such as homogeneous cell seeding and long-term viability [14].

Hydrogels, owing to their high water content and tunable composition, provide ECM-like environments that support cell encapsulation and tissue regeneration. Yet, diffusion limitations and degradation kinetics often complicate reproducibility.

Cell sheet engineering allows the stacking of confluent cellular layers while preserving endogenous ECM and cell–cell junctions, resulting in functional tissues with promising

regenerative applications, though scalability and vascularization remain limiting factors [15].

Despite these remarkable advances in tissue engineering and 3D culture systems, there is still no single standardized approach capable of faithfully reconstructing and modelling the full complexity of human organs and tissues *in vitro* [16]. As a result, research in this field remains open and continuously evolving, paving the way for the emergence of Organ-on-Chip technologies as a promising alternative.

1.1 General overview of Organ-on-Chip technologies

The escalating demand for more representative and predictive models in pharmacological and toxicological research has propelled researcher to develop innovative microfluidic platforms promising a more accurate comprehension of organ-level responses to diverse stimuli, drugs, and diseases [17]. The continuous search for physiologically relevant *in vitro* models has driven the development of Organ-on-Chip (OoC) technologies, which combine advances in microfluidics, tissue engineering, and biomaterials science to recreate organ-level functions in miniaturized devices [18], [19]. Diverging from traditional 2D plate culture, this emerging technology allow to recreate a microphysiological systems (MPS), establishing physiologically relevant microenvironments, fostering enhanced cell longevity, function, and physiologically accurate responses [7].

Building on this concept, Organ-on-Chip (OoC) platforms represent a further evolution of MPS, in which microfluidic flow is exploited to sustain cellular homeostasis, generate controlled gradients, reproduce key biomechanical cues such as shear stress, and support the co-culture of multiple human cell types. These unique capabilities make OoC devices particularly promising for reducing the gap between preclinical *in vitro* testing and clinical translation [20], [21].

An OoC is essentially a micro-engineered device, typically composed of one or more microchannels, in which living cells are cultured within a controlled microenvironment that allows continuous perfusion of culture medium. This configuration not only ensures a dynamic supply of nutrients and oxygen with simultaneous removal of waste products but also enables the precise delivery of physical and biochemical stimuli.

Infact, OoC platforms exhibit many critical and defining characteristics like the 3D nature and arrangements of the tissues on the platforms, the integration of multiple cell types and the presence of biomechanical forces such as stretch forces or shear forces, that regulate cell shape and signal transduction [22].

The field emerged in the late 2000s with the first lung-on-chip [23], which successfully recapitulated the alveolar–capillary interface and breathing motions within a micro-engineered platform, marking a paradigm shift from traditional static cultures toward MPs capable of mimicking dynamic tissue–tissue interfaces.

For decades, early OoC devices relied primarily on simple 2D cell cultures, either seeded directly onto the flat surfaces of microchannels or grown on porous polymer membranes separating adjacent compartments. While these configurations enabled the first demonstrations of dynamic culture under perfusion, they were inherently limited in their ability to reproduce the three-dimensional (3D) architecture and cell–cell/cell–matrix interactions that govern tissue organization and function *in vivo* [24].

Membrane-based OoC systems feature a basement membrane with a thin and porous membrane offering a cohesive cell substrate and separation between tissues in various organs. Different cells can be seeded on both sides of a membrane or even migrate across it, depending on the membrane's thickness and the pore features enabling cell communication and contact. Membranes serve as essential living barriers, crucial for preserving cells and fluids within a confined space while facilitating the migration and exchange of substances through their pores. Despite their function as drivers of mechanical stimuli it's essential to differentiate between the membrane's separatory function and its contribution to supporting cell culture, specifically in the context of cell-scaffold interactions. Cell adhesion depends on several parameters, including membrane material, surface chemistry, and topography. The ECM's topography should be closely mimicked, as it influences behaviour such as migration and specialization [25]. Continuous efforts have recently been made to include ECM-like structures for 3D cell cultures or even co-cultures in microfluidic device [26].

Over the past two decades, significant progress has been made to overcome these limitations. A major step forward has been the integration of biomimetic scaffolds and extracellular matrix (ECM)-like materials into OoC platforms, moving the field from "cells-on-a-chip" toward fully functional "organs-on-a-chip" [24]. Approaches such as hydrogels, electrospun fibers, and 3D-printed scaffolds have been introduced to recreate the biochemical, mechanical, and topographical cues of native tissues. These substrates not only

support cell adhesion and viability but also promote polarization, differentiation, and long-term functionality, enabling more physiologically relevant modelling of organ-specific functions and disease mechanisms. Importantly, scaffold-integrated OoCs provide enhanced opportunities for multi-cell type co-culture, vascularization, and spatial organization, thereby addressing some of the most critical shortcomings of earlier microfluidic devices.

The continuous evolution of OoC platforms has expanded their application from single-organ models to increasingly complex multi-organ systems, often referred to as body-on-chip. Early devices focused on reproducing essential physiological features of single organs such as the lung [27–30], liver [31,32], heart [33], kidney [34], or gut [35,36], providing more predictive models for drug metabolism, toxicity testing, and disease mechanisms than conventional *in vitro* systems. For instance, lung-on-chip models have been used to replicate the alveolar–capillary barrier under cyclic mechanical stretch, while liver-on-chip devices maintain hepatocyte functionality for weeks under dynamic perfusion, enabling accurate assessments of drug-induced liver injury.

Beyond organ-specific models, coupled multi-organ platforms allow the recreation of systemic processes such as absorption, distribution, metabolism, and excretion (ADME) [37]. Examples include fluidically linking liver, kidney, and intestine chips to predict human pharmacokinetics with remarkable accuracy or connecting liver and heart chips to reproduce clinically relevant drug–drug interactions . More sophisticated assemblies, such as platforms mimicking the female reproductive cycle or metastatic cancer spread across multiple organs, highlight the potential of OoCs to capture complex physiological and pathophysiological dynamics.

A particularly promising frontier lies in personalized medicine. Organ chips lined with patient-derived cells, including induced pluripotent stem cell (iPSC)-derived tissues, enable the modelling of inter-individual variability, rare genetic disorders, and comorbidities. Such systems could be used to stratify patient subpopulations (e.g., male vs. female, young vs. elderly), optimize drug dosing, and design targeted clinical trials, thereby increasing the likelihood of therapeutic success. When combined with computational pharmacokinetic/pharmacodynamic (PK/PD) modelling, multi-organ chips represent a powerful tool to tailor treatments, minimize adverse effects, and ultimately move toward a “patient-on-a-chip” paradigm [38]. The implementation of such advanced concepts, however, ultimately depends on the underlying design and fabrication of the OoC platform itself. In fact, the choice of material plays a pivotal role in defining not only the biocompatibility and stability of the device, but also its manufacturability, reproducibility,

and scalability toward industrial translation. A careful material selection therefore becomes the foundation for enabling complex functions—ranging from the co-culture of multiple cell types to long-term perfusion and integration with sensors—that are essential for personalized medicine applications.

1.1.1 Material Strategies for Organ-on-Chip Platforms

The choice of material for Organ-on-Chip (OoC) fabrication is a critical determinant of device functionality, microfabrication strategy, read-outs, and biocompatibility. A typical OoC platform is composed of different materials or surface modifications tailored to the specific application, and the selection process often represents a trade-off between desired biological performance, accessibility to fabrication facilities, and scalability toward industrial production (Table 1) [39]. Several materials are being explored for microfluidic device fabrication, including elastomers such as polyester elastomers, thermoplastic elastomers, and thermoplastic materials such as poly(methyl methacrylate) (PMMA), polycarbonate (PC), cyclic olefin copolymer (COC), polystyrene (PS), and polylactic acid (PLA) [40], as well as natural polymers.

Historically, the gold-standard material of choice has been polydimethylsiloxane (PDMS), a thermocurable elastomer widely adopted due to its optical transparency, biocompatibility, gas permeability, and ease of prototyping via soft lithography. PDMS enabled the rapid spread of OoC research within academic environments, supporting the first generation of lung-, gut-, and liver-on-chip platforms. However, several drawbacks limit its broader application, particularly in industrial and regulatory settings. These include the absorption of hydrophobic small molecules, the leaching of uncured oligomers, high evaporation rates, unstable surface treatments, and channel deformation under prolonged perfusion. Furthermore, PDMS molding remains difficult to automate at large scale, slowing down translation from research to market.

Table 1 Overview of materials commonly employed for Organ-on-Chip fabrication. Adapted from Chak Ming Leung et al. [41].

Materials	***Advantages***	***Drawbacks***	***Experimental model***
PDMS	Gas-permeability Optical transparency Elasticity Biocompatibility	Absorption of small molecules Difficulty in mass production	Disease modelling Mechanical and chemical stimuli Electrode patterning
Thermoplastics	Optical transparency Mass production Cost-effective Low absorption	Rigidity Difficulty in producing complex structures Low permeability	Drug screening Large-scale experimentations
3D printing resins	High mechanical and thermal properties Low cost Complexity and design freedom	Autofluorescence Opacity Toxicity Low permeability Surface roughness	3D design modelling Rapid prototyping
Glass	Optical transparency Inert Biocompatibility Low autofluorescence	Laborious fabrication Fragile Expensive	Electrode patterning
Silicon	Low absorption Generation of high-resolution channels on the nanoscale	Laborious fabrication due to need for clean-room facilities Expensive	On-chip sensors Formation of diffusive barriers

Thermoplastics (PMMA, PC, COC, PS) stand out for their robustness, low drug absorption, and optical properties comparable to PDMS, while also being compatible with mass production processes. Importantly, these polymers are already widely used in biomedical devices, ensuring biocompatibility and regulatory acceptance. Polylactic acid (PLA), a biodegradable thermoplastic derived from renewable sources, has also gained increasing attention [40], particularly when processed into electrospun scaffolds that mimic the extracellular matrix (ECM)[42].

In parallel, glass and silicon have been employed in OoC fabrication due to their high precision and chemical resistance. Glass is optically transparent and inert, making it ideal for imaging applications, but its processing is expensive and requires advanced facilities. Silicon, with its heritage in microelectronics, allows the fabrication of intricate

microstructures but is less biocompatible and non-transparent, limiting its use in biological applications.

Overall, a comparative overview underscores the ongoing transition from PDMS toward thermoplastics and hybrid materials, driven by the need for scalable, reproducible, and regulatorily compliant platforms [43]. In this context, thermoplastics have emerged as particularly promising materials for OoC fabrication, not only because of their low absorption and compatibility with large-scale production, but also due to the wide range of microfabrication techniques that can be applied to them. These include injection molding, hot embossing, laser micromachining, and additive manufacturing, each offering specific advantages in terms of precision, throughput, and cost-effectiveness. A closer examination of thermoplastic processing methods is therefore warranted to highlight their central role in bridging the gap between academic prototyping and industrial adoption of OoC devices.

1.1.2 Focus on Microfabrication Techniques for Thermoplastics

The transition from PDMS to thermoplastics in Organ-on-Chip (OoC) fabrication has been largely driven by the broader range of scalable and standardized manufacturing techniques available for these polymers. Unlike PDMS, which relies predominantly on soft lithography and manual assembly, thermoplastics can be processed through industrially established technologies, thereby bridging the gap between academic prototyping and mass production [44]. One of the most widespread methods is injection molding, which allows the replication of complex microchannel geometries with high fidelity and reproducibility. Once the initial mold is fabricated, injection molding offers very low cost per unit, making it highly suitable for large-scale industrial production and commercialization of OoC devices. Hot embossing represents another scalable strategy in which a heated mold is pressed onto a thermoplastic substrate to imprint microstructures. This approach provides high-resolution features and is compatible with a wide range of thermoplastics such as PMMA, COC, and PC. Compared to injection molding, hot embossing is better suited for medium-scale production and for iterative prototyping phases where tool costs need to be minimized.

For rapid prototyping in academic or pre-industrial contexts, laser micromachining has emerged as a versatile and cost-effective method [45]. Using CO_2 or UV lasers, microchannels and reservoirs can be patterned with high precision directly on thermoplastic

sheets, which are then bonded to form multilayer devices [46]. This approach was successfully used to integrate electrospun PLA scaffolds into PMMA chips, enabling biomimetic architectures for tissue culture with reduced drug absorption compared to PDMS [47].

An alternative rapid strategy is cut-and-assemble prototyping, in which thermoplastic sheets are patterned using laser cutters or CNC milling and subsequently stacked to create multilayer OoC systems. This benchtop method is highly flexible, inexpensive, and allows fast design iteration, making it particularly attractive for academic groups and early-stage research.

Finally, 3D printing technologies (such as stereolithography, fused deposition modeling, and two-photon polymerization) have expanded the OoC fabrication repertoire[48]. While still facing challenges of resolution, autofluorescence, and biocompatibility of commercial resins, 3D printing offers unparalleled design freedom and the possibility to integrate complex geometries[49], vascular-like networks, and modular plug-and-play architectures. Emerging hybrid approaches combine 3D printing with electrospinning or soft lithography, opening new avenues for scaffold integration and multi-material devices.

Taken together, these microfabrication strategies demonstrate that thermoplastics are not only advantageous materials from a biological perspective but also enablers of scalable, reproducible, and customizable fabrication workflows. Their versatility in both prototyping and industrial contexts highlights their central role in the ongoing evolution of OoC platforms toward standardized and commercially viable solutions

1.2 Emerging International Standards for Organ-on-Chip Technologies

The effective translation of Organ-on-Chip (OoC) platforms into industrial, clinical, and regulatory settings depends heavily on the establishment of standards that ensure reproducibility, interoperability, and quality assurance [50]. Despite the remarkable progress of the field, the lack of harmonized frameworks for terminology, material qualification, experimental design, and data management still hampers their full translational impact [51].

At the international level, the ISO/TS 23494 series introduce a provenance information model for biological materials and data, covering the entire life cycle from acquisition to analysis (ISO, 2023a). This standard enables traceability and validation via structured, machine-actionable metadata. Upcoming parts of the series (ISO/DIS 23494-2 and 23494-

3) will extend the model to domain-specific stages such as sample acquisition and processing (ISO, 2023b; NIST, 2023). Additionally, ISO 22916:2022 establishes interoperability requirements for microfluidic devices, laying the foundation for modular, “plug-and-play” OoC integration.

In Europe, the CEN/CENELEC Focus Group on Organ-on-Chip (FGOoC), working with EUROoCS and the Joint Research Centre (JRC), published a comprehensive standardization roadmap in 2024. Developed with contributions from more than 120 experts, the roadmap highlights material qualification, sterilization protocols, and cell identity/functionality as top priorities. It also recommends aligning with ISO technical committees to foster global harmonization. The roadmap further proposes the establishment of a dedicated European technical committee on microphysiological systems to consolidate efforts and feed into international ISO initiatives (CEN-CENELEC, 2024a; CEN-CENELEC, 2024b; JRC, 2025) [50].

From a translational perspective, robust implementation of these standards requires well-defined protocols across the OoC workflow—including fabrication, flow control, cell seeding, readout calibration, and inter-operator reproducibility testing. The use of thermoplastics with low drug absorption (e.g., PMMA, COC) has been recognized as a way to minimize variability and enhance data reliability, while ISO 10993 biocompatibility assessments remain essential for regulatory approval [51].

Equally important is the adoption of digital provenance pipelines that capture metadata, experimental conditions, and outcomes in a FAIR-compliant way. Such pipelines enhance reproducibility, support benchmarking, and facilitate adherence to Good Laboratory Practice (GLP), thereby strengthening the regulatory credibility of OoC-generated data.

Beyond formal standardization, the field is also moving toward open platform approach**es**. The Translational Organ-on-Chip Platform (TOP), developed within the hDMT consortium, exemplifies this strategy. TOP introduces a modular framework based on a fluidic circuit board (FCB) and interchangeable microfluidic building blocks (MFBBs), analogous to printed circuit boards in electronics. By adopting standardized footprints (e.g., microscope slide and microtiter plate formats) and connector dimensions, TOP enables researchers and companies to combine modules from different providers into interoperable multi-organ systems. Importantly, the platform balances openness with proprietary innovation, allowing developers to integrate proprietary modules into a standardized environment. This dual approach fosters collaboration across academia and industry, lowers

barriers for new users, and accelerates the path from academic proof-of-concept to industrial-grade systems [50].

Looking forward, next-generation OoC development will increasingly converge with enabling technologies such as biofabrication, multimodality imaging, and artificial intelligence (AI).

These domains promise to amplify human-relevant biomimicry, deliver high-content and high-throughput readouts, and support automated, unbiased data analysis. However, their successful integration depends on early, systematic standardization and open interfaces to avoid fragmentation and ensure interoperability.

Finally, widespread adoption of harmonized norms and user-friendly platforms could significantly democratize OoC usage. By lowering the technical barrier, standards would empower biological researchers and laboratory technicians to operate these devices without requiring advanced engineering expertise. This would bridge the gap between biologists and engineers, allowing daily use of OoCs in diverse research environments, as highlighted by recent surveys showing that commercial OoC systems are becoming increasingly robust and accessible, while self-made devices remain complex and less standardized.

The conceptual framework discussed above is summarized in Figure 2, which illustrates the role of standardization as the central driver connecting enabling technologies (biofabrication, imaging, AI), validation of representative models, and regulatory/industrial implementation.

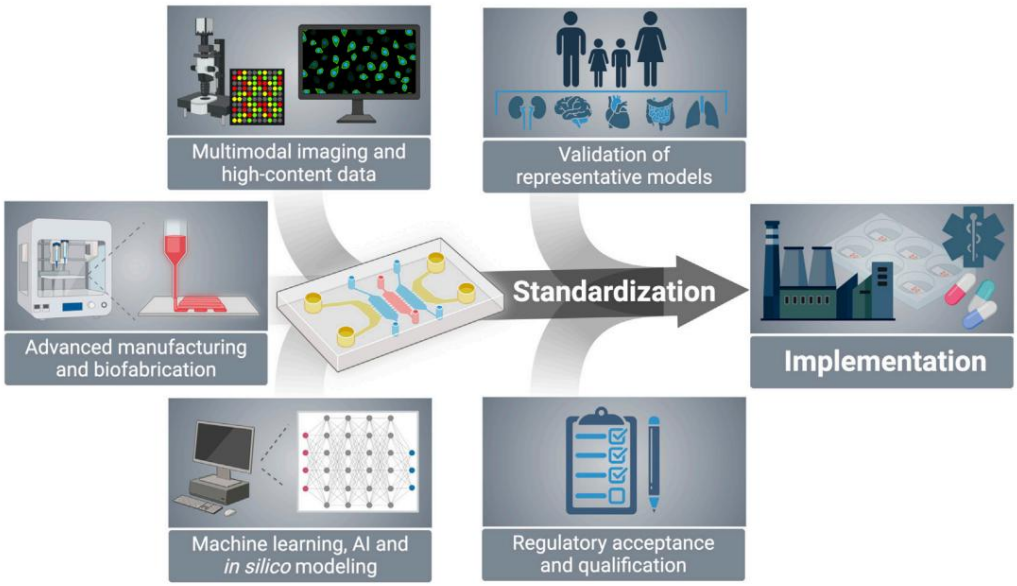

Figure 2 Standardization as a central element for Organ-on-Chip development. The scheme highlights how advanced technologies such as biofabrication, multimodal imaging, and artificial intelligence converge with validation, regulatory acceptance, and industrial implementation, with standardization acting as the key driver. Adapted from J. Meneses et al. [50].

1.3 Aim and Scope of This Work

The overall aim of this doctoral research was to design, fabricate, and validate innovative Organ-on-Chip (OoC) platforms integrating scaffolds for the development of physiologically relevant *in vitro* models. Conventional two-dimensional (2D) cultures and animal models are still widely employed in preclinical research, yet both approaches suffer from intrinsic limitations: 2D cultures fail to capture the complexity of tissue architecture, while animal models are affected by interspecies differences, high costs, and ethical concerns. These limitations highlight the urgent need for alternative platforms that combine reproducibility, scalability, and biomimicry while contributing to the reduction of animal use in research.

Although polydimethylsiloxane (PDMS) has long dominated OoC prototyping, the present work establishes its foundations in the standardization of rapid prototyping strategies based on thermoplastic materials. The core objective of the project was the development of scaffold-integrated OoC devices incorporating biopolymeric porous substrates to support the culture of different tissues. The fabrication workflow was primarily based on CO_2 laser micromachining of polymeric sheets combined with multilayer thermal bonding, enabling fast production, design flexibility, and high reproducibility. The research activities carried out within this doctoral project were structured around four main objectives, as schematically

summarized in Figure 3. These objectives cover the optimization of scaffolds, the development of thermoplastic polymers and processes for OoC fabrication, the integration and characterization of scaffolds within microfluidic platforms, and finally the optimization of cell culture strategies for biological validation

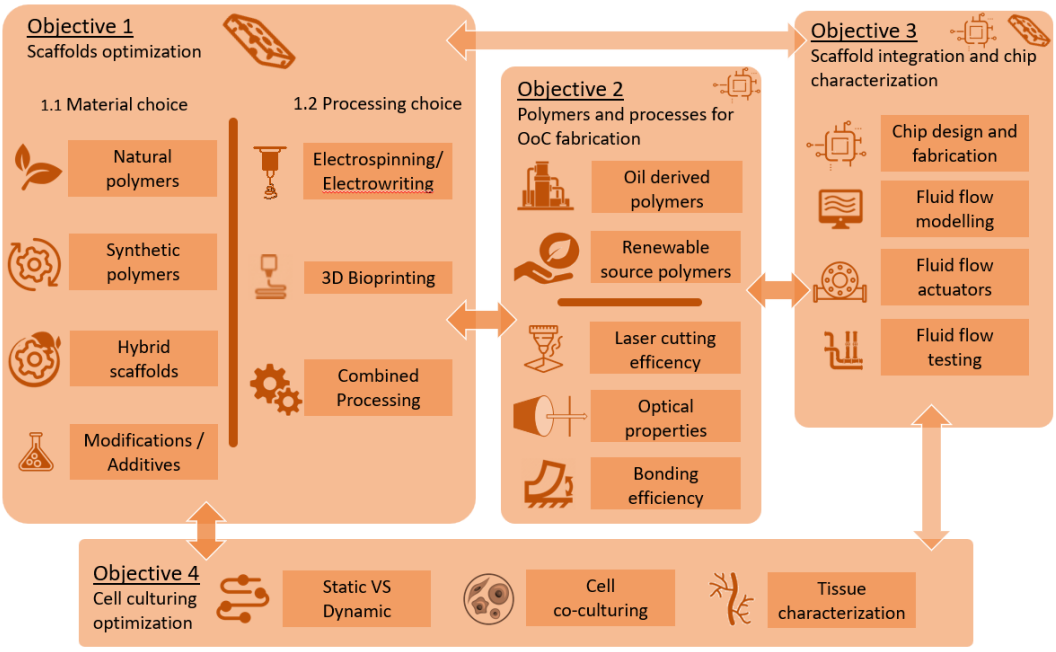

Figure 3 Schematic representation of the main objectives of the PhD proposal.

Different processing techniques were explored to generate 2D or 3D scaffolds, including electrospinning and hydrogel casting. Their mechanical properties were investigated by uniaxial tensile tests and correlated with porosity and pore architecture, while spectroscopic and wettability analyses further characterized their surface properties. Preliminary bioactivity and cytocompatibility were assessed in static cultures to identify optimal combinations of materials and processing routes for specific tissue models.

Particular focus was placed on the development of thermoplastic devices using polymethyl methacrylate (PMMA), chosen for its optical transparency, processability, and compatibility with industrial workflows. CO_2 laser micromachining was systematically optimized to maximize transparency and minimize thermal damage. The impact of processing parameters on polymer crystallinity was analyzed using differential scanning calorimetry (DSC) and X-ray diffraction (XRD), while UV–Vis spectroscopy quantified optical transmission on PMMA. Laser cutting quality was assessed by scanning electron

microscopy (SEM) to identify optimal input parameters (laser power, scanning speed, pulse frequency). Surface modification by dry chemistry was implemented to improve bonding performance, which was then evaluated through burst pressure measurements.

Once fabrication parameters and material properties were optimized, the third objective was the design and production of microfluidic platforms. The devices were modelled via CAD and assembled in multilayer configurations. Electrospun PLA scaffolds and hydrogels were integrated either as membranes or 3D compartments, with specific deposition techniques designed to minimize structural damage or contamination. Scaffold morphology was analyzed before and after chip assembly to evaluate any alteration induced by fabrication or bonding.

Fluid dynamics within the microchannels was managed through perfusion with syringe pumps or peristaltic pumps, where controlled flow rates generate shear stresses that play a crucial role in regulating cell differentiation and tissue development. Computational fluid dynamics (CFD) simulations were performed to predict fluid behaviour and iteratively refine chip design, ensuring that flow conditions remained physiologically relevant.

This thesis encompasses four complementary applications:

- **Liver-on-Chip (LoC):** a dual-chamber platform to model chronic, low-dose exposure of hepatocytes to colorectal cancer-derived extracellular vesicles (EVs), overcoming the limitations of conventional static cultures that rely on acute, high-dose stimulation.
- **Tumor-on-Chip (ToC):** a microfluidic device supporting breast cancer cells and stromal populations (e.g., cancer-associated fibroblasts, CAFs) to investigate tumour–microenvironment interactions and drug resistance mechanisms, with proof-of-concept drug testing.
- **Brain-on-Chip (BoC):** a modular system for assessing drug selectivity across distinct neural cell populations, enabling co-cultures of neurons and microglia under physiologically relevant flow conditions.
- **ISO-compliant dual-scaffold platform** – a multilayer thermoplastic microfluidic device designed according to ISO 22916:2022 standards for microfluidic interoperability.

Through these case studies, the thesis demonstrates how microfluidics, combined with electrospun scaffolds and/or hydrogels, can generate versatile, reproducible, and scalable OoC platforms. Beyond providing biological insights, the goal is to deliver robust preclinical tools for drug testing, bridging the translational gap between conventional *in vitro* systems, animal models, and clinical applications.

Building upon recent technological advances and international efforts toward standardization, the research pursued two main objectives over the past three years:

I. **Innovative fabrication approaches** — developing rapid prototyping strategies (e.g., CO_2 laser micromachining, cut-and-assemble bonding) to design cost-effective and reproducible thermoplastic devices as alternatives to PDMS-based chips. These methods enabled the integration of electrospun PLA scaffolds and hydrogels, creating structurally and functionally biomimetic microenvironments.

II. **Standardization and industrial translation** — aligning fabrication and validation workflows with ISO 23494, ISO 10993, and the 2024 CEN/CENELEC FGOoC roadmap, to ensure reproducibility across batches, interoperability with laboratory infrastructure, and scalability toward industrial manufacturing.

The central hypothesis of this thesis is that thermoplastic OoC platforms integrating biomimetic scaffolds can provide physiologically relevant and reproducible microenvironments, while simultaneously meeting requirements for standardization and large-scale adoption.

The doctoral research was originally structured into four main objectives, spanning scaffold optimization, development of polymers and fabrication processes, scaffold integration within microfluidic devices, and biological validation through cell culture optimization. Figure 4 reports the initial project timeline, as presented in the doctoral application, which outlined the planned progression of the activities across the three years. According to this schedule, scaffold optimization and polymer processing were prioritized in the first year, while chip integration and characterization were planned from the second year onwards, culminating with biological validation during the third year. An extensive literature review supported the entire project, providing the conceptual and methodological framework for the experimental work

Project phase	First year				Second year				Third year			
	M - 3	M - 6	M - 9	M - 12	M - 3	M - 6	M - 9	M - 12	M - 3	M - 6	M - 9	M - 12
Extensive Literature Review												
Scaffold optimization												
Polymer and processes for OoC fabrication												
Scaffold integration and chip characterization												
Cell culturing optimization												

Figure 4 Project schedule

The central vision of this doctoral research was the development of thermoplastic Organ-on-Chip (OoC) platforms that combine biomimetic scaffolds, rapid prototyping strategies, and advanced manufacturing approaches to generate physiologically relevant *in vitro* models. The conceptual framework behind this work can be effectively summarized in Figure 5, which illustrates the interconnection between the technological, biological, and translational dimensions of the project.

At the technological level, the use of CO_2 laser micromachining enables rapid, versatile, and low-cost prototyping of thermoplastic devices, while advanced manufacturing and biofabrication approaches allow the integration of biopolymeric scaffolds that mimic the architecture and functionality of native extracellular matrix. These innovations not only enhance the structural and functional biomimicry of the platforms but also improve their scalability and reproducibility, paving the way for potential industrial translation.

From a biological perspective, the integration of aligned and random electrospun scaffolds supports long-term cell culture under dynamic flow, enabling live imaging and high-content data acquisition. This allows the monitoring of cell behavior in real time and under controlled microphysiological conditions, providing a powerful tool for studying disease mechanisms and evaluating drug selectivity.

Finally, at the translational level, the research contributes to the broader effort of moving toward regulatory acceptance of OoC devices as standardized, reliable alternatives to animal testing. By aligning with current guidelines and roadmaps, these platforms can be envisioned as future components of drug development pipelines, potentially reducing reliance on animal models while increasing the predictive power of preclinical studies.

In this way, the graphical abstract (Figure 5) encapsulates the overarching aim of the thesis: to bridge the gap between innovative engineering solutions and biomedical

applications, ultimately advancing the field of *in vitro* modelling toward reproducibility, scalability, and clinical relevance.

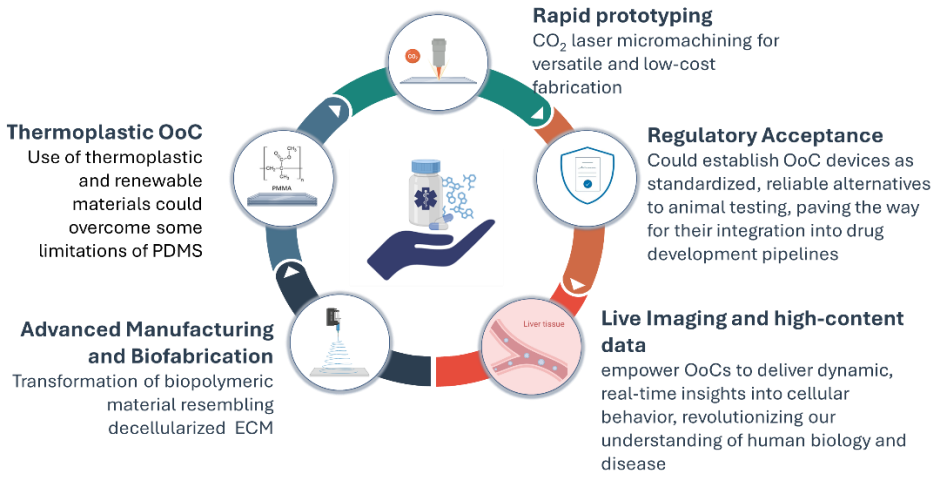

Figure 5 Graphical abstract summarizing the main aims of this doctoral research. The scheme highlights the integration of thermoplastic materials, rapid prototyping, scaffold biofabrication, live imaging, and regulatory acceptance as key enablers for the development and translation of Organ-on-Chip platform

1.4 Thesis Structure

The structure of this doctoral thesis was designed to guide the reader through a coherent and progressive exploration of the research activities — from the conceptual framework to the experimental validation and final translational implications. The organization of the chapters reflects the multidisciplinary nature of the project, which integrates material science, microengineering, and cell biology to develop reliable and standardized Organ-on-Chip platforms.

Chapter 1 introduces the scientific background and motivation behind the study. It outlines the current limitations of conventional 2D cultures and animal models, discusses the evolution of Organ-on-Chip technologies, and reviews the emerging international standards that are shaping the field. This introductory framework establishes the rationale for developing thermoplastic-based OoC systems as scalable, reproducible, and ethically sustainable alternatives for preclinical research.

Chapter 2 details the materials and methodologies adopted throughout the work, with a primary focus on the engineering aspects of the research. It describes the fabrication and

characterization of electrospun scaffolds and hydrogels, the design and rapid prototyping of thermoplastic microfluidic devices through CO_2 laser micromachining, and the optimization of bonding and sealing strategies. This chapter also includes computational fluid dynamics (CFD) analyses and mechanical tests aimed at ensuring the structural integrity and performance of the devices under dynamic conditions. Biological protocols and validation strategies are only introduced in the later chapters, allowing this section to concentrate on theengineering technological foundations of the work.

Chapter 3 presents the results of the optimization and characterization of fabrication parameters and material properties, addressing the main engineering challenges encountered during the development of thermoplastic-based Organ-on-Chip (OoC) platforms. The chapter focuses on achieving high optical transparency, mechanical robustness, and reliable bonding performance, while ensuring compatibility with biological applications. It includes the systematic analysis of laser micromachining parameters, bonding strength, optical transmittance, and sealing efficiency, establishing the technological foundation for the subsequent biological validation of the devices.

Chapters 4 to 7 illustrate four representative case studies that demonstrate the versatility and progressive technological maturity of the developed platforms:

• the **Liver-on-Chip (LoC)**, designed to model chronic, low-dose exposure of hepatocytes to colorectal cancer–derived extracellular vesicles, overcoming the limitations of conventional static cultures that rely on acute stimulation;

• the **Tumor-on-Chip (ToC)**, integrating breast cancer and stromal cells to investigate tumor–stroma interactions and mechanisms of drug resistance. This platform reflects an increased design awareness, incorporating commercial connectors to enhance usability and reproducibility while laying the groundwork for ISO-compliant device architectures. It also represents a more advanced application stage, as co-cultures were successfully performed directly within the microfluidic environment;

• the **Brain-on-Chip (BoC)**, enabling dynamic co-cultures of neurons and microglia to assess drug selectivity and neuroinflammatory responses under physiologically relevant flow conditions;

• and the **ISO-compliant dual-scaffold platform**, a standardized thermoplastic device developed in accordance with ISO 22916:2022, demonstrating interoperability, robustness, and scalability toward industrial production.

Each case study is structured to present the rationale, design, fabrication, and biological validation of the corresponding device, collectively illustrating how engineering methodologies can be effectively translated into physiologically relevant and standardized *in vitro* models.

Chapter 8 concludes the thesis by summarizing the key findings and discussing their broader scientific and technological implications. It emphasizes the contribution of this research to the standardization and scalability of Organ-on-Chip technologies and outlines future perspectives, including sensor integration, industrial implementation, and regulatory alignment.

Overall, the thesis follows a clear trajectory from concept to validation, showing how rapid prototyping, scaffold biofabrication, and standardization converge toward the creation of physiologically relevant and reproducible microphysiological systems. This structured approach highlights the synergy between engineering innovation and biomedical application, paving the way for the industrial and translational adoption of thermoplastic Organ-on-Chip platforms.

2 Materials and Methods

Poly(lactic acid) (PLA; grade 2002D, NatureWorks, Minnetonka, MN, USA) was used as the polymeric matrix for the fabrication of electrospun scaffolds. Acetone (Ac) and chloroform (TCM) (Sigma Aldrich, Saint Louis, MO, USA) were employed as solvents for PLA dissolution.

Microfluidic devices were fabricated from polymethyl methacrylate (PMMA; Clarex, Nitto Jushi Kogyo Co. Ltd., Tokyo, Japan; supplied by Weatherall Ltd., Wendover, UK) sheets of varying thicknesses (0.2, 0.5, 1, 2, and 3 mm), selected according to their specific structural or functional role within the device.

The connection system included male mini-Luer plugs, male mini-Luer fluid connectors (ChipShop®), tubing in silicone or polytetrafluoroethylene (PTFE; 1/16″ OD), as well as microfluidic female Luer-lock fittings and PFA fittings with ETFE ferrules (1/16″ OD) (Darwin Microfluidics, Paris, France). These components were used to establish leak-free connections between the devices and the syringe or peristaltic pumps employed during dynamic culture.

2.1 Fabrication of Electrospun Scaffolds (ESs)

Electrospinning is a fibre fabrication technique that uses a high-voltage electric field to transform a polymer solution into continuous ultrathin filaments. The solution is extruded from a syringe through a metal needle connected to a high-voltage power supply. Under the electric field, electrostatic forces overcome the surface tension of the fluid and deform the droplet into a “Taylor cone”; from this cone emerges a charged jet that elongates rapidly and thins as the solvent evaporates along its path.

The solidifying jet deposits fibres onto a grounded conductive collector (Figure 6), where they can be gathered in random or aligned arrangements depending on the collector configuration and speed.

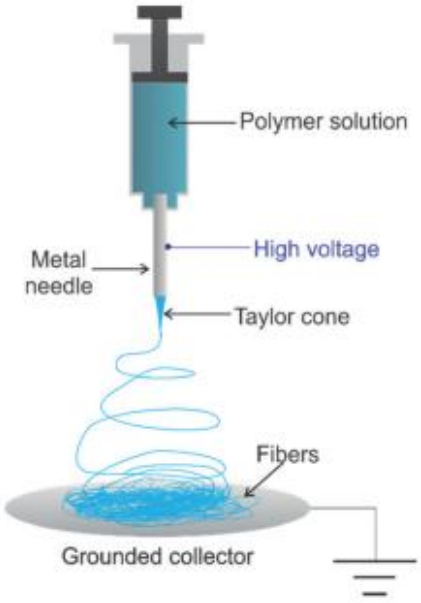

Figure 6 Schematic representation of the electrospinning setup used for scaffold fabrication. A polymer solution is extruded through a metal needle while a high-voltage electric field is applied between the needle tip and a grounded collector. The electrical forces overcome surface tension to form a Taylor cone at the needle tip, from which a charged jet emerges, stretches and solidifies into ultrafine fibres that deposit on the collector.

For this purpose, PLA (grade 2002D, NatureWorks, Minnetonka, MN, USA) was dissolved at 10 wt% in a solvent mixture of chloroform and acetone (2:1 v/v). The solution was prepared under continuous magnetic stirring at room temperature and left overnight to ensure complete homogenization.

The polymer solution was then loaded into a 10 mL glass syringe fitted with a stainless steel needle (20-gauge) and connected to a syringe pump operating at a controlled flow rate of 0,7 mL/h. Electrospinning was performed using a NF-103 electrospinning apparatus (MECC Co., Ltd., Fukuoka, Japan) with operating parameters derived from previously optimized settings [52]: an applied voltage of 17 kV and a needle-to-collector distance of 15 cm (Figure 7). Fiber deposition was collected on a grounded rotating drum (10 cm in length, 10 cm in diameter) covered with aluminum foil.

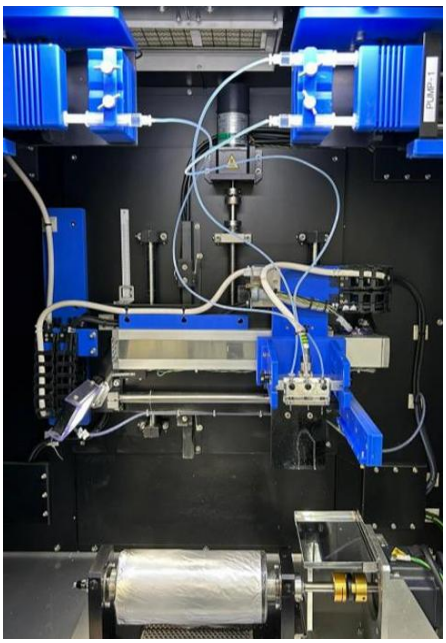

Figure 7. View of the electrospinning apparatus used for fibrous scaffold fabrication. The instrument integrates programmable syringe pumps (top) connected to a spinneret, a high-voltage power supply, and a multi-axis translation stage. A rotating cylindrical collector covered with aluminium foil (bottom) serves as the target for fibre deposition, allowing controlled production of aligned or randomly oriented fibres

For the fabrication of random fibre mats (R-PLA), the rotating drum was operated at 100 rpm, while for aligned fibre mats (A-PLA) the speed was increased to 4000 rpm to promote fibre stretching and orientation along the rotation axis. Each electrospinning run lasted 300 minutes and produced fibrous mats of approximately 20 × 30 cm, with an average thickness of ~70 µm for R-PLA scaffolds and ~30 µm for A-PLA scaffolds. After collection, the electrospun mats were dried for 48 hours under a fume hood to remove residual solvents. At the end of the electrospinning and drying process, large PLA fibrous mats were obtained, exhibiting a continuous and flexible structure (Figure 8).

Figure 8 Representative image of an electrospun PLA fibrous mat (~20 × 30 cm) after 180 min of electrospinning and 48 h drying under a fume hood.

Before use, the electrospun PLA membranes were treated in a cold plasma reactor (AP-300 Plasma System, Nordson, CA, USA) under conditions of 50 W for 30 s (Figure 9). The treatment was repeated twice to ensure exposure of both membrane surfaces. Since the functionalization effect of air plasma gradually diminishes over time, all subsequent processing and characterization of the PLA mats were carried out within 30 minutes of treatment [53].

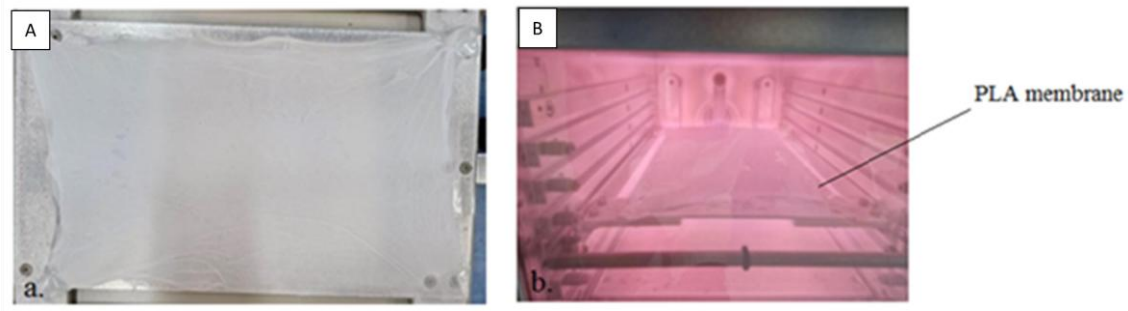

Figure 9 (A) Electrospun PLA scaffold stretched on a support frame before plasma treatment. (B) Interior view of the cold-plasma reactor during oxygen plasma functionalisation; the pink glow indicates the plasma, and the PLA membrane is highlighted by the arrow.

The functionalized mats were subsequently cut *via* laser cutter into specimens of appropriate size for devices integration. Table 2 summarizes the laser power and cutting parameters used to process the electrospun membranes into samples suitable for incorporation into the devices.

Table 2 Laser parameters used to cut electrospun membrane samples into circular and rectangular sections for integration into organ on chip and insert like devices. The table reports the laser power, cutting speed applied for each sample geometry.

	Power [%]	Speed [mm/sec]
PLA membrane	5	350

2.2 Fabrication of Alginate-Based Hydrogels

Sodium alginate hydrogels were prepared by ionic crosslinking with calcium chloride ($CaCl_2$). Briefly, sodium alginate was dissolved in phosphate-buffered saline (PBS) without salts—since the presence of ions could interfere with alginate solubility through ionic exchange—to obtain a 2.5% (w/v) solution. The mixture was placed on a magnetic stirrer and homogenized for approximately 3 h at room temperature. For subsequent experiments, the solution was diluted 1:1 with PBS, resulting in a final alginate concentration of 1.25% (w/v). Crosslinking was achieved using $CaCl_2$ solutions at different concentrations. A 1% (w/v) solution was prepared in distilled water for hydrogel formation in multiwell plates, while a 3% (w/v) solution was employed during the fabrication of hydrogels in mechanical testing molds.

For mold-based hydrogels, filter paper was first soaked in $CaCl_2$ 3% (w/v) and placed in a Petri dish together with the mechanical testing mold. The alginate solution (1.25% w/v) was then injected into the mold using a syringe and left to react for 5 min. Subsequently, a second filter paper saturated with $CaCl_2$ 3% was positioned on top of the mold to complete crosslinking, which proceeded for an additional 15 min. After this time, the filter paper was removed, and the crosslinked hydrogel was carefully extracted from the mold. The hydrogels were washed three times with distilled water to eliminate unreacted ions, and cylindrical discs of defined size were obtained using a biopsy punch (Figure 10). The discs were then stored in Petri dishes filled with distilled water until further use.

Figure 10 Representative image of a crosslinked alginate hydrogel disc obtained after ionic gelation with $CaCl_2$. The disc shows homogeneous morphology and integrity, allowing easy handling and transfer without structural damage.

2.3 Microfluidics Design and Fabrication

Considerable effort was devoted to reproducing scaffold-integrated microfluidic devices using rapid prototyping techniques, which remain less explored in the literature compared to the PDMS-based approaches that are still regarded as the gold standard.

The design of the Organ-on-Chip (OoC) platforms was guided by the need for modularity, reproducibility, and compatibility with the intended biological assays. Each device was conceived for a specific biological target, aiming to reproduce physiologically relevant fluid dynamics while integrating an electrospun scaffold and/or an hydrogel. In certain configurations, the ES served a dual role: acting both as a substrate for cell culture and as a semipermeable partition between two adjacent culture/perfusion chambers.

Building on the earliest approaches and prototypes, the designs presented in this work progressively evolved from simple microfluidic devices equipped with screw connections and custom fittings—ensuring high sealing performance and resistance to elevated pressures—[3] to more advanced ISO-compliant platforms [4] thereby enhancing usability and accessibility not only for engineers but also for researchers in biology, biotechnology, and related fields. These later designs integrate standardized microfluidic connectors, facilitating reliable fluid handling, modularity, and compatibility with existing microfluidics accessories. Such a transition not only improved device robustness and reproducibility but also represented an essential step toward alignment with industrial and regulatory requirements, thereby enhancing the translational potential of the developed OoC systems.

To enable rapid prototyping with thermoplastic materials, pre-formed sheets of poly(methyl methacrylate) (PMMA) with thicknesses ranging from 0.2 to 3 mm were employed. Three-dimensional modelling was first carried out using Autodesk Fusion 360 (Autodesk, San Rafael, CA, USA), which allowed the rational design of inlets, outlets, and fluid volumes, as well as the integration of connectors and other required components.

Based on these layouts, each PMMA sheet was laser-patterned and engineered so that, once stacked in the prescribed order, the layers formed one or more culture chambers connected by microchannels with dedicated inlets and outlets for continuous perfusion of culture medium. This multilayer assembly ensured precise alignment and functional reproducibility of the devices.

An example of a final microfluidic platform made with Autodesk Fusion 360, highlighting the internal fluidic volumes, mini-luer connectors, and male-luer plugs, is shown in Figure 11.

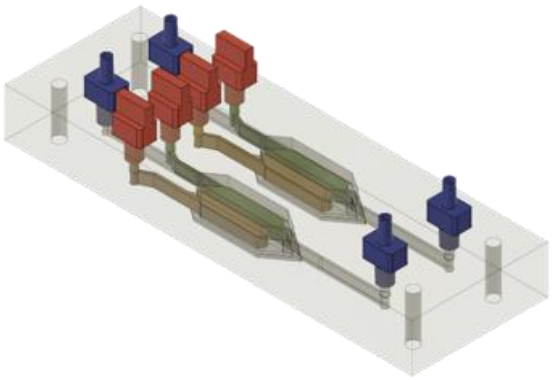

Figure 11 Example of a microfluidic device highlighting the internal fluidic volumes. The image also shows the integration of mini-Luer connectors and male Luer plugs used for fluid connection and occlusion.

This multilayer architecture, combined with the optical transparency, mechanical rigidity and low absorption of small compounds of the thermoplastic material, supports a range of microfluidic layouts tailored to different experimental models (Tumor- [54], Liver- [55]or Brain-on-Chip).

The rationale behind the layout of each individual layer and the overall architecture will be presented in the chapters dedicated to each device.

After generating the three-dimensional model of the final device, it was sliced according to the thicknesses of commercially available PMMA sheets. Each layer was then exported as a two-dimensional *.dxf* file. Figure 12 illustrates an example of the slicing process for a microfluidic device.

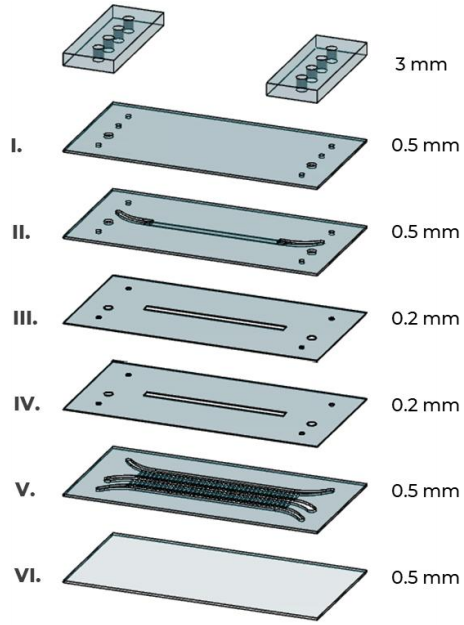

Figure 12 Exploded view of the device illustrating the six PMMA layers (I–VI) obtained after slicing of the 3D model. Each layer was designed with a specific thickness (0.2–0.5 mm) according to its structural and functional role within the device, while the uppermost layer (3 mm) accommodates the inlet/outlet ports. The sequence highlights the internal microchannels, alignment holes, and the position of the electrospun scaffold integrated during assembly.

These design files in *.dxf* formats were subsequently imported into Autolaser, the control software of the CO_2 laser cutter, which allowed fine adjustment of laser power and speed to execute the required cutting and engraving operations (Figure 13).

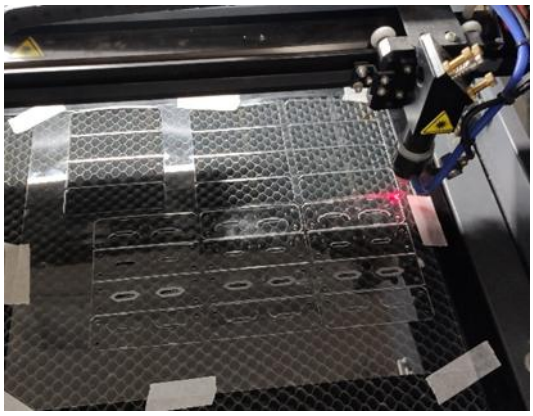

Figure 13 Laser cutter in operation during the micromachining of PMMA sheets. The laser beam, controlled via Autolaser software, was used to cut and engrave the predefined microfluidic layouts exported as .dxf files.

Following micromachining, PMMA layers were cleaned *via* a two-step process. All layers were sealed in a bag containing a 70/30 (v/v) solution of ethanol and distilled water and immersed in an ultrasonic bath for approximately two minutes to remove particulate debris.

A second cleaning step was carried out to improve the surface finish of the engraved regions. Solvent vapour polishing was performed by suspending the PMMA substrates above a chloroform bath contained in a 100 mm diameter, 6 mm high glass Petri dish. Chloroform was added until reaching a level 2 mm below the support on which the engraved layers were placed. The samples were exposed to solvent vapours for 3 minutes, following an adapted protocol previously described in the literature [56] (Figure 14). Including the time required for positioning and handling of the layers, the entire polishing step lasted approximately 5 minutes.

Figure 14 Solvent vapour polishing of engraved PMMA layers. The laser-machined substrates were suspended above a chloroform bath in a glass Petri dish to expose the engraved regions to solvent vapours, thereby restoring surface smoothness and optical clarity.

After the cleaning steps, the PMMA layers were aligned using customized aluminium jigs with positioning pins to ensure precise stacking. Small drops of PMMA solution were applied between layers to facilitate pre-assembly, and the electrospun PLA scaffold was positioned in the designated recess according to the design (Figure 15A).

The multilayer assembly was then bonded under controlled conditions by thermal pressing at 70 °C under 1200 psi for 180s using a Carver Laboratory Press (Menomonee Falls, WI, USA) [57] (Figure 15B). Figure 15 illustrates the assembly within the alignment jig prior to bonding and the press employed for thermal sealing.

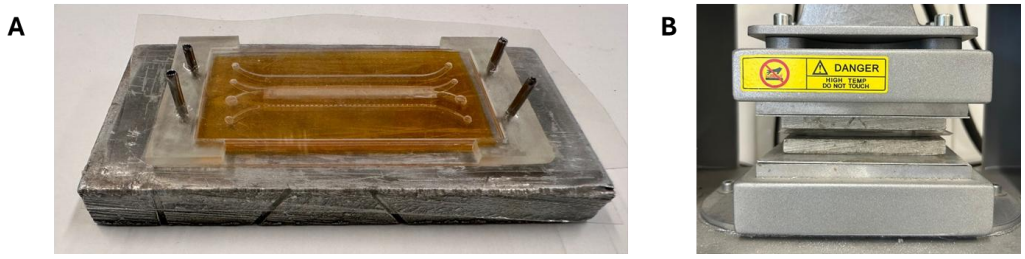

Figure 15 Alignment and thermal bonding of the device. (A) PMMA layers aligned using customized aluminium jigs with positioning pins prior to bonding, with the electrospun PLA scaffold positioned in the recess. (B) Carver Laboratory Press (Menomonee Falls, WI, USA) employed to thermally bond the layers at 70 °C under 1200 psi for 180 s.

A schematic overview of the fabrication workflow is provided in Figure 16, summarizing the key steps of laser micromachining, cleaning, and thermal assembly. The entire process, from PMMA sheet ablation to final bonding, requires approximately 10–15 minutes *per* device, highlighting the efficiency of the adopted rapid prototyping strategy.

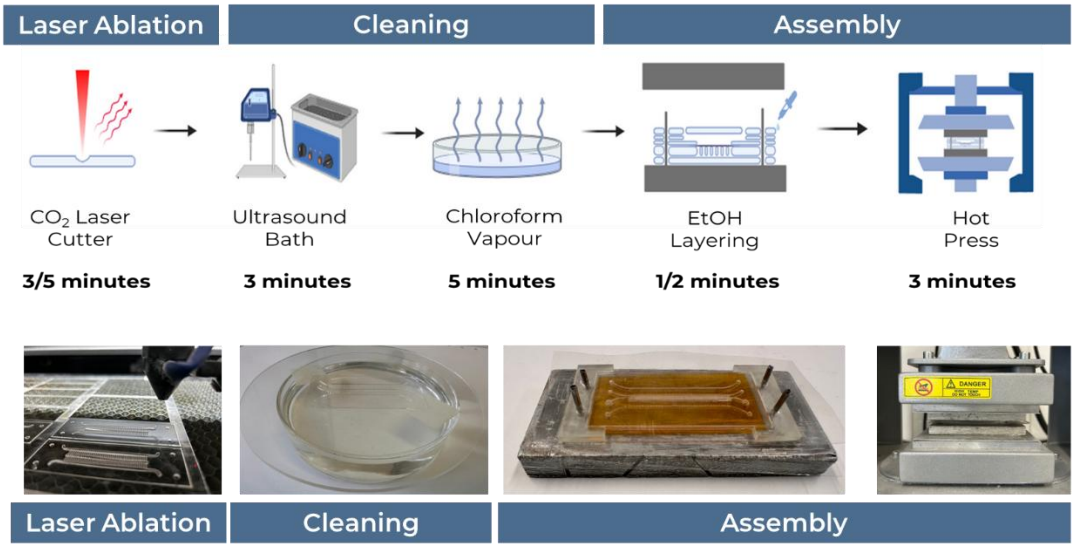

Figure 16 Workflow of device fabrication. The process involves three main stages: (i) laser ablation of PMMA sheets using a CO_2 laser cutter, (ii) cleaning by ultrasonic bath in ethanol solution, chloroform vapour polishing, and (iii) assembly by layer alignment, and thermal bonding using a laboratory press. Representative images of each step are shown below the schematic.

2.4 Fabrication and Device Characterization

Main fabrication and characterization procedures were conducted to assess the structural integrity, optical performance, and fluidic reliability of the PMMA-based microfluidic platforms. These analyses ensured that the developed bonding strategy and device configuration provided the mechanical robustness and transparency required for subsequent biological experiments.

2.4.1 Bonding Test

Before the fabrication and experimental use of the microfluidic devices, the efficiency of the bonding process was evaluated through burst testing. For this purpose, a dedicated design (Figure 17) was employed. The test device consisted of three PMMA layers, each 0.5 mm thick. The middle layer contained a 0.4 mm deep and 10 mm long channel leading into a circular chamber of 4 mm in diameter, sandwiched between the two outer layers. The top layer was also designed to host the microfluidic connections, which were established through ferrule and customized connectors secured to the device with a screw/nut system.

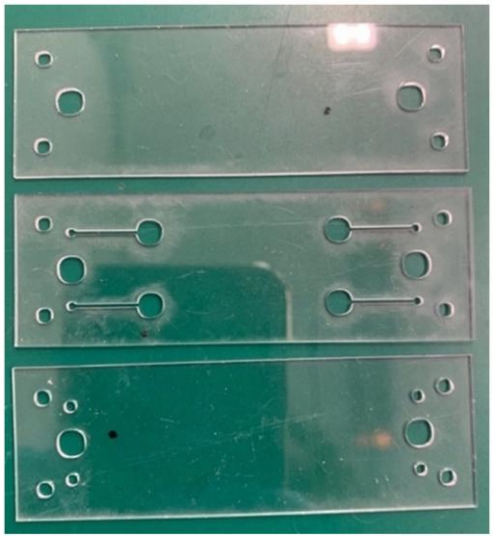

Figure 17 PMMA layers (0.5 mm thick) employed for the fabrication of the burst test device. The middle layer incorporates a microchannel leading to a circular chamber (4 mm diameter), while the external layers provide sealing and host the inlet/outlet ports for tubing connection.

The top and bottom layers incorporated blind channels, enabling a direct assessment of the pressure resistance of the sealed device. One of the most critical requirements of any

microfluidic bonding method is its ability to provide robust sealing, ensuring that channels can sustain increasing pressure without leakage.

A syringe pump was employed to deliver water into the channels at a constant flow rate of 1 mL/min, while a pressure sensor continuously recorded the corresponding pressure values. Once the channel and the chamber were completely filled, the flow was maintained until the pressure exceeded the bonding strength of the device, ultimately resulting in rupture. This experiment enabled the determination of the burst pressure and provided a direct measure of the sealing efficiency of the bonding protocol employed.

2.4.2 PMMA Optical Properties

The optical transparency of PMMA samples was evaluated by UV–Vis spectroscopy (Specord UV-250 Plus, Analytik Jena, Germany). Measurements were performed on single sheets with a thickness of 0.5 mm and on bonded double layers with a total thickness of 1 mm. For all analyses, rectangular specimens (76.2 mm × 25.4 mm, thickness 0.5 mm) were prepared.

UV–Vis spectroscopy is a molecular absorption technique that relies on the interaction of ultraviolet or visible photons with matter. When a photon is absorbed, a molecule undergoes an electronic transition from its ground state to an excited state. In a typical UV–Vis spectrum, the abscissa corresponds to the wavelength, while the ordinate reports either absorbance or transmittance. The resulting spectra are characterised by peaks of different intensity, which reflect the probability of photon absorption at specific wavelengths. In this study, measurements were restricted to the visible region (300–700 nm), and 532 nm was selected as the representative wavelength for transmittance analysis, following previous reports in the literature. Transmittance (T) is defined as the ratio between the transmitted light intensity (I) and the incident light intensity (I_0), and can be expressed as a fraction (0–1) or as a percentage according to the equation (1):

$$T = I/I_0 \times 100 \qquad (1)$$

From this, absorbance (A) can be calculated using the Lambert–Beer law, equation (2):

$$A = \log_{10} (I_0/I) \qquad (2)$$

By analysing both absorbance and transmittance profiles, the optical transparency of PMMA was quantitatively assessed under different processing conditions, enabling direct comparison between untreated sheets and bonded layers.

2.4.3 Sealing Commercial connectors

Before the fabrication and biological use of the microfluidic devices, the efficiency of sealing between the commercial microfluidic connectors and the PMMA layers was evaluated through dedicated sealing tests. The adoption of commercial connectors was preferred over early prototypes based on screw–nut closures and ferrules, in order to improve user-friendliness, reduce handling of the device and associated tubing/pumps, and maintain sterility during dynamic culture experiments in the OoC platforms.

For this purpose, a multi-layer PMMA device was specifically designed and fabricated (Figure 18). The test structure consisted of four layers with distinct roles:

Layers 1 and 2 (combined thickness of 3 mm) accommodated the commercial Male Mini Luer connectors (ChipShop®), which have a total height of ~3 mm. Several inlet/outlet hole diameters (ranging from 2.46 mm to 2.49 mm) were tested to determine the optimal fit ensuring leak-free sealing.

Layer 3 (1 mm thick) contained microchannels measuring 25 × 1 × 1 mm (volume: 25 mm^3), designed to permit fluid flow and allow visual inspection of leakage using coloured water.

Layer 4 (1 mm thick) acted as the bottom sealing sheet, completing the microfluidic structure.

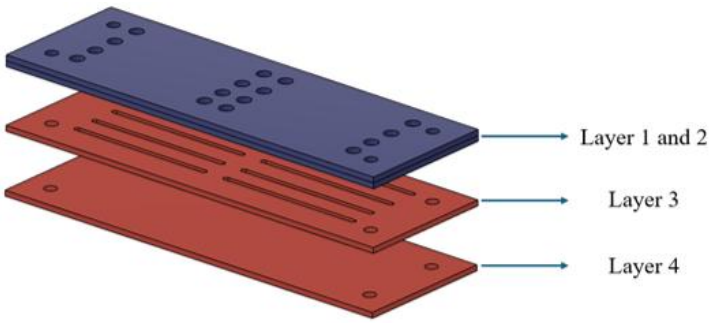

Figure 18 Schematic representation of the slicing and assembly process of the microfluidic device. (A) Exploded view of the individual PMMA layers obtained from the sliced 3D model. (B) Assembled multilayer configuration showing the alignment of microchannels and through-holes. (C) Top view of the final device highlighting the parallel microchannel network

Figure 19 provides a top view of the device, showing the precise diameters tested (2.46–2.49 mm). This prototype enabled the evaluation of sealing performance for different hole dimensions and the identification of the optimal diameter to ensure tight integration of commercial connectors and plugs. The use of this standardized configuration allowed rapid connection/disconnection, enhanced reproducibility, and minimized the risk of leakage during perfusion assays.

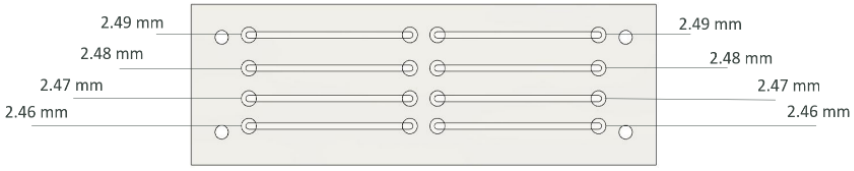

Figure 19 Top view of the fabricated multi-channel device highlighting the range of tested hole diameters (2.46–2.49 mm).

Pressure resistance tests were performed using a LabSmith® pressure sensor (maximum range: 800 kPa). Several 1/16'' PTFE (polytetrafluoroethylene) tubes of equal length were prepared. At one end, each tube was fitted with a short silicone section and a Male Mini Luer connector (ChipShop®), serving as the inlet connection to the device. The opposite end was coupled to a threaded connector (T116 CapTite One-Piece Fitting, LabSmith®) and mounted in a square holder together with the pressure sensor, which was screwed onto a LabSmith® uProcess® breadboard (uPB-05). The pressure sensor was interfaced with the valve manifold (uProcess® 4VM02, LabSmith®) and connected to the USB automation interface (EIB200, LabSmith®) for data acquisition via uProcess® software. On the outlet side of the holder, an identical silicone connection was established. The distal end of this tube was linked to a 12.5 mL Luer-lock syringe (IDEX Health&Science® adapters and flangeless fittings), which was mounted on a syringe pump (NE-300, Dutscher®). Prior to pump loading, syringes were filled with water mixed with food dye to enhance visualization of fluid flow. The entire setup was duplicated to enable two pressure tests to be performed simultaneously (Figure 20).

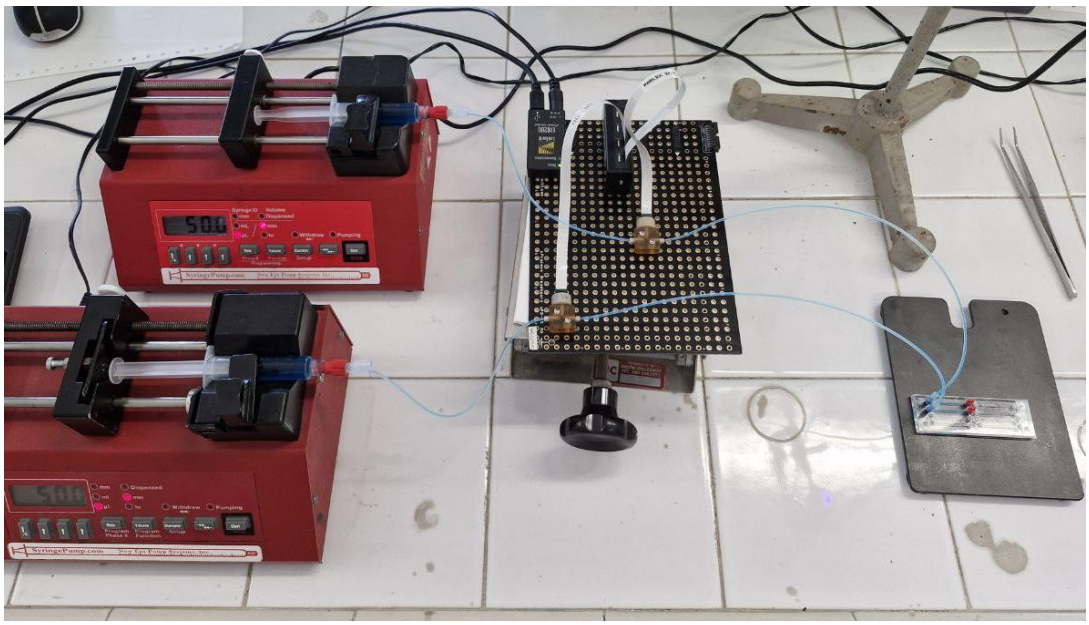

Figure 20 Experimental setup showing syringe pumps connected to the microfluidic device via the LabSmith® uProcess® breadboard with integrated pressure sensors and tubing.

Once the syringes were mounted, liquid was pushed into the device inlet, ensuring the absence of air bubbles in the tubing. Syringe pumps were then activated at a flow rate of 250 µL/min to fill the device from inlet to outlet. The outlets were subsequently sealed with Male Mini Luer plugs (ChipShop®), after which the sensors were calibrated. Pressure measurements were recorded while simultaneously operating the syringe pumps at a flow rate of 50 µL/min. The process was monitored in real time using a Dino-Lite® digital microscope positioned above the device.

2.4.4 Computational Fluid Dynamics Analysis

Fluid dynamic simulations of the microfluidic devices were performed using ANSYS Fluent Academic 2023R3 (Analysis Systems Inc.). The geometries of the fluidic domains were first designed in Autodesk Fusion 360 and exported in *.IGES* format. To simplify the computational model, the electrospun PLA scaffold separating the two chambers was assumed to behave as a solid and impermeable barrier assuming for each conditions cells confluency.

Given the microscale dimensions of the channels, the flow was described by the continuity equation (Eq. 3) and the Navier–Stokes equations for incompressible flow (Eq. 4)

$$\boldsymbol{\rho \frac{dv_i}{dx_i} = 0} \qquad (3)$$

$$\boldsymbol{\rho \frac{dv_i}{dt} + \rho v_j \frac{dv_j}{dx_j} = -\frac{dp}{dx_i} + \mu \frac{d^2 v_i}{dx_j^2}} \qquad (4)$$

where ρ is the fluid density, μ the dynamic viscosity, v_i is the velocity vector, x_i is the position vector, t the time, and p the pressure.

The CFD analysis was implemented to solve Eqs. (3) and (4) in order to evaluate velocity fields, wall shear stresses (WSS), and pressure distributions within the culture chambers. The problem was solved using the finite volume method with a pressure-based solver suitable for laminar, low-Reynolds-number flows with constant fluid density. A mesh sensitivity study was conducted for each chamber geometry.

Tetrahedral meshes were generated and validated to ensure element aspect ratios above 0.95, thus maintaining adequate numerical quality. Pressure–velocity coupling was achieved using the SIMPLE algorithm, which guarantees mass conservation across the entire computational domain.

Boundary conditions were set as follows: inlets defined by fixed volumetric flow rates, outlets set to zero pressure (0 Pa) to represent open boundaries, and walls assigned a no-slip condition. Steady-state simulations were run until convergence was reached, enabling accurate evaluation of flow characteristics inside the devices.

2.5 Accessories and side devices

The three-dimensional geometry of each accessories was modelled in Autodesk Fusion 360™.

2.5.1 Design of the Liver on Chip Connector

Regarding Liver on Chip [55] project (Chapter 4) a connector was engineered to provide a leak-tight interface between the device and the microfluidic tubing supplying and removing media from the culture chambers. The connector design is characterized from ports for the tubing, grooves for gaskets, screw holes and alignment pins (Figure 21).

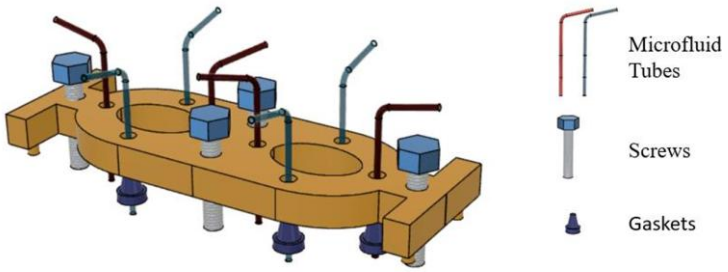

Figure 21 Assembly of the leak-tight connector used in the Liver-on-Chip device. The three-dimensional CAD rendering illustrates the 3D-Printed connector with ports for the microfluidic tubing and alignment pins. The exploded view shows the ancillary components—microfluidic tubes (colour-coded), screws and gaskets—required to form a sealed coupling between the chip and the perfusion system.

Once finalised, the CAD file was exported in *.STL* format and printed using a Formlabs Form 3 stereolithography printer with Clear V4 resin. Post-processing entailed two ten-minute washes in isopropanol to remove residual resin, followed by a fifhteen minute UV post-cure at 60 °C. After removal of the support pins, the connector was ready for use.

2.5.2 Static Culture Device

To benchmark the Organ-on-Chip (OoC) platforms against conventional static culture systems, custom inserts were developed incorporating the same electrospun scaffold (ES) integrated in the device. These inserts enabled static culture on a three-dimensional scaffold

identical to that employed in the perfused configuration, thus allowing a direct comparison between static culture on a commercial insert (e.g., Transwell), static culture on the custom insert, and dynamic culture on the OoC. This strategy allow to disentangle the effects of flow and mechanical cues from those attributable exclusively to the scaffold.

The custom insert was designed in CAD software (Autodesk Fusion 360™, Autodesk, San Rafael, CA, USA) to fit into a standard 24-well cell culture plate. Figure 22 illustrates the final configuration of the insert, showing the body, the integrated electrospun membrane, and the snap-fit closure. The system consists of three main components: a frustum-shaped body, an electrospun PLA membrane, and a snap-fit closure mechanism that secures the membrane between two rings. The modular design allows the membrane assembly to be detached, flipped, and re-clamped, enabling seeding of different cell types on opposite sides of the scaffold (Figure 22 B).

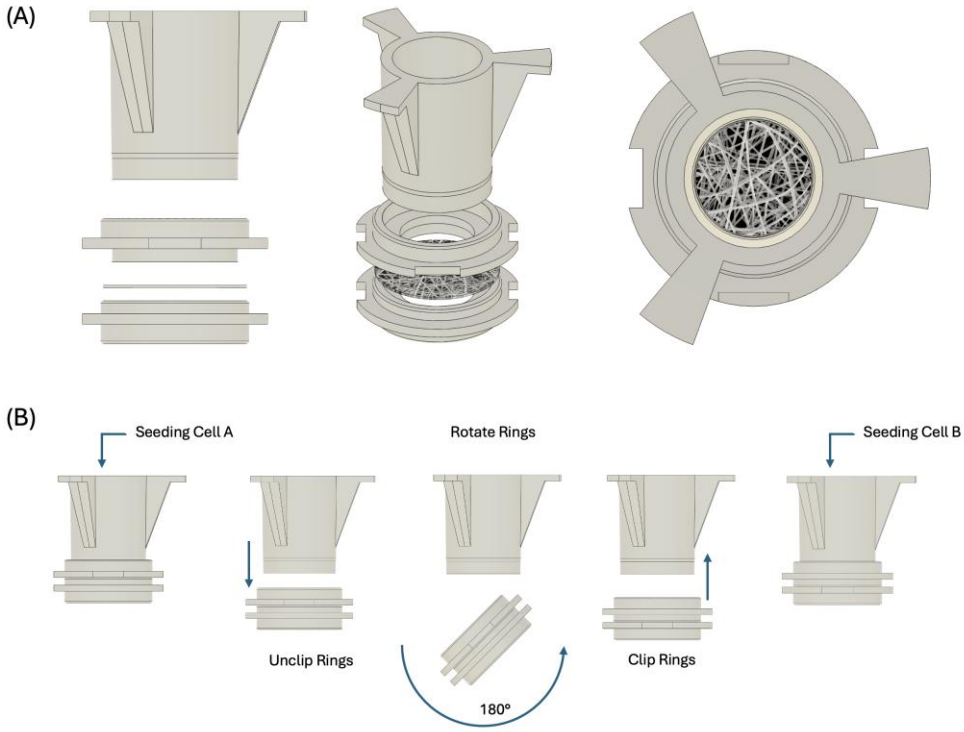

Figure 22 Design and operation of the custom insert for static culture on electrospun scaffolds. (A) CAD representation of the insert showing its three components: the frustum-shaped body, the snap-fit closure mechanism, and the integrated electrospun membrane. (B) Schematic of the reversible assembly process. After seeding cell type A, the rings can be unclipped, rotated by 180°, and re-clipped, enabling the seeding of cell type B on the opposite side of the membrane.

The effective membrane area is ~0.34 cm², versus 0.33 cm² for the commercial insert. Both the body and closure were fabricated by stereolithography using the same protocol as for the connector.

The design was converted into an *.STL* file and fabricated using a Form 2 3D printer (Formlabs, MA, USA) with Clear Resin V4. Following printing, the parts were cleaned in

isopropyl alcohol for 20 minutes and post-cured in a heated chamber (Form Cure, Formlabs) at 60 °C for 15 minutes, according to the manufacturer's specifications.

Before use, the assembled insert containing the ES was sterilised by immersion in a 70/30 ethanol/water solution for 2 hours, followed by UV irradiation with bactericidal lamps for an additional 1 hours.

2.6 Characterization of Materials and Surfaces

A comprehensive set of physicochemical and morphological analyses was performed to validate the quality of the fabricated devices and the electrospun scaffolds prior to biological testing. The goal was to assess microstructural fidelity, surface properties, and reproducibility across batches, ensuring the suitability of the platforms for cell culture and dynamic perfusion experiments.

2.6.1 Scanning Electron Microscopy (SEM)

The morphological characterization of the electrospun PLA scaffolds was performed by scanning electron microscopy (SEM, Quanta 200 F, FEI, USA)(Figure 23) to evaluate fibre uniformity, distribution, and structural integrity prior to their integration into microfluidic platforms or static culture devices. For SEM preparation, circular specimens (~3 mm in diameter) were excised from the electrospun mats and carefully mounted on aluminium stubs using conductive carbon tape to ensure electrical continuity. To improve imaging resolution and minimize charging effects, the samples were sputter-coated with a thin layer of gold for 120 s under an argon atmosphere (Scancoat Six, Edwards Laboratories, Milpitas, CA, USA). SEM micrographs were acquired at different magnifications (500× to 5000×) to capture both the global scaffold architecture and fibre morphology.

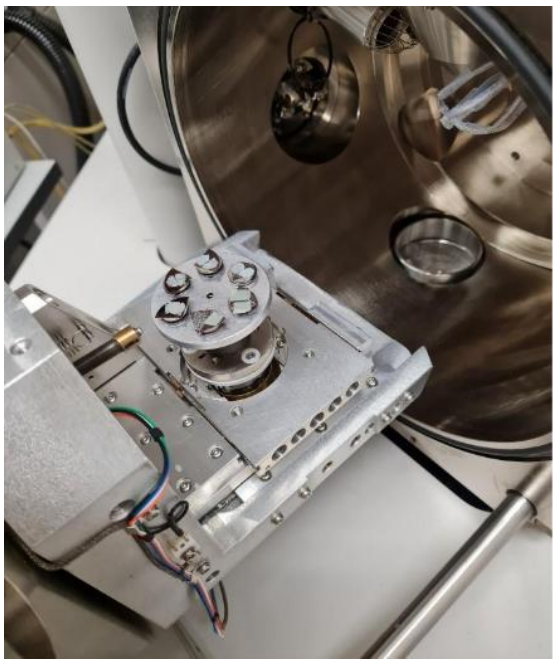

Figure 23 Scanning electron microscope (SEM) sample holder with electrospun PLA scaffold specimens mounted on aluminium stubs and coated for imaging. The system is shown inside the SEM chamber prior to analysis

In addition scaffolds were immediately analysed after fabrication following oxygen plasma treatment and after their integration into the microfluidic devices, where they were exposed to solvents and elevated temperatures due to thermal bonding during the assembly process, as detailed in the following sections.

Quantitative analysis of the images was performed using the DiameterJ plugin in ImageJ, which allowed determination of fibre diameter distribution, mean diameter, and variability across independent scaffold batches. This analysis provided an estimate of the reproducibility of the electrospinning process and enabled the comparison between random and aligned fibre mats.

SEM examination was extended to scaffolds retrieved from platforms and Insert-like devices after cells culture, in order to verify possible structural alterations induced by perfusion, bonding, or cell colonisation within the devices.

A fixation protocol was performed following standard procedures [58]. Briefly, samples were rinsed three times in complete 1X phosphate-buffered saline (PBS) for 3 min each and subsequently fixed in 4% glutaraldehyde for 30 min at 4 °C. After fixation, the specimens were washed in PBS and dehydrated through a graded ethanol series (15%, 30%, 50%, 75%, and 100% v/v), with each step repeated three times for 3 min at room temperature. The dehydrated samples were then air-dried for 12 h under a fume hood, mounted on aluminum stubs with adhesive carbon tape, and sputter-coated with gold for 90 s prior to imaging.

2.6.2 Porosity

The porosity (φ) of the aligned (A-PLA) and random (R-PLA) electrospun scaffolds was determined in order to quantify the fraction of void space within the fibrous mats, a parameter directly related to nutrient and oxygen diffusion as well as to cell infiltration capacity. Porosity was calculated according to the relation expressed in equation (5) [59] which compares the apparent density of the scaffold (ρ_scaffold) with the bulk density of poly(lactic acid) (ρ_PLA), the latter provided by the supplier's technical datasheet.

$$\varphi = 1 - \frac{\rho_{scaffold}}{\rho_{PLA}} \qquad (5)$$

The resulting value of φ is a dimensionless number, expressed as a percentage, that represents the scaffold's overall porosity: higher values indicate a more open microstructure, while lower values correspond to denser fibrous networks.

To obtain reproducible measurements, five independent samples (N = 5) were prepared for each scaffold type. Discs of defined diameter were cut using a CO_2 laser cutter to ensure precision and uniformity of dimensions across all replicates. Each sample was subsequently weighed with a high-precision analytical balance (sensitivity ±0.1 mg), and its volume was estimated from the known geometric dimensions of the cut discs (thickness, diameter, and area). From these measurements, the apparent density of each scaffold was calculated using equation (6), which relates mass to volume. The apparent density values were then compared with the theoretical bulk density of PLA to derive porosity values for both A-PLA and R-PLA scaffolds.

$$\rho_{scaffold} = \frac{M_{scaffold}}{V_{scaffold}} \qquad (6)$$

This methodology allowed us not only to quantify the average porosity but also to evaluate the reproducibility of the electrospinning process across multiple batches. In addition, differences in porosity between aligned and random fibre mats were expected, reflecting the influence of fibre orientation on scaffold packing density and void fraction. Such porosity data, when integrated with SEM-based morphological analysis, provided a comprehensive characterization of scaffold architecture.

2.6.3 Atomic Force Microscopy (AFM)

Atomic force microscopy (AFM) was performed using a Dimension FastScan® AFM system (Bruker BioSpin GmbH, Bruker Cellular Analysis, Inc., Massachusetts, USA) to characterize the surface morphology and nanomechanical properties of obtained aligned electrospun polylactic acid (PLA) scaffolds. The analysis was conducted in contact mode, enabling real-time monitoring of force interactions between the probe and the sample to assess mechanical properties, scaffold reproducibility, and compatibility.

Three scaffold samples (5 mm × 5 mm) were carefully cut and mounted onto glass slides using carbon tape to ensure stability during scanning (Figure 24).

Figure 24 Membrane adhered to the glass slide with carbon tape

A Bruker silicon tip on nitride cantilever (Lev3En, Bruker) was used, with the following specifications: tip radius ~10 nm, thickness: 650 nm, length: 115 µm, width: 25 µm, resonance frequency: 70 kHz, and spring constant: 0.4 N/m. The samples were analyzed in two orientations: parallel to the fiber alignment and perpendicular to it, allowing a comprehensive assessment of topographical and mechanical variations across the scaffold structure.

2.6.4 Mechanical Properties

To investigate the mechanical behaviour of the electrospun scaffolds, tensile tests were performed on both randomly oriented (R-PLA) and aligned (A-PLA) fibre mats. Rectangular specimens (90 × 10 mm) were cut from the electrospun membranes using a CO_2 laser cutter, in order to ensure precise and reproducible sample geometry. Mechanical tests were conducted using a laboratory dynamometer (Zwick, Figure 25), operating under displacement control with a crosshead speed of 1 mm/min. Stress–strain curves were

recorded for each specimen, from which the main mechanical properties were derived, including elongation at break, ultimate tensile strength, and Young's modulus.

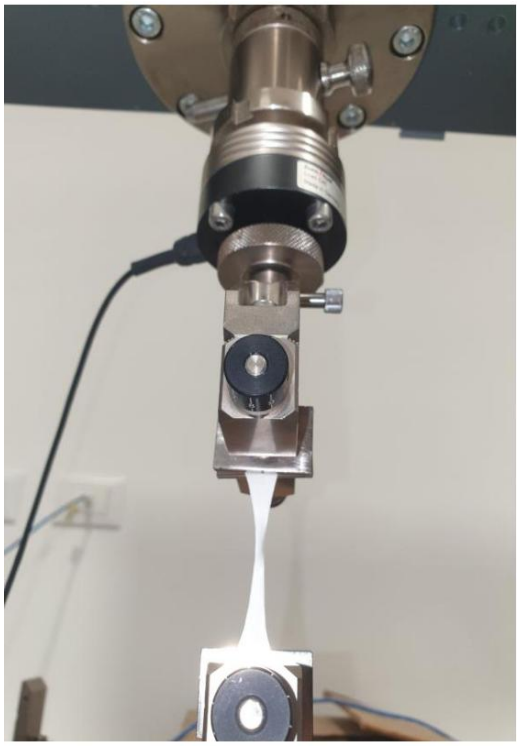

Figure 25Experimental setup for the uniaxial tensile test of electrospun PLA scaffolds. Rectangular specimens (90 × 10 mm) were precisely cut from the fibrous mats using a CO_2 laser cutter to ensure uniform geometry and reproducibility. The picture shows a scaffold sample into the laboratory dynamometer.

This comparative analysis between R-PLA and A-PLA scaffolds was designed to elucidate the influence of fibre orientation on the tensile response of the mats.

Randomly oriented scaffolds were expected to display lower stiffness but greater isotropic deformability, whereas aligned scaffolds were hypothesised to exhibit enhanced stiffness and tensile strength along the fibre axis, consistent with their anisotropic microstructure. Evaluating these parameters was essential to assess scaffold robustness and to determine their suitability for integration into Organ-on-Chip platforms, where mechanical stability under continuous perfusion and handling during assembly represent critical requirements

2.6.5 Water contact angle (WCA)

Wettability of the electrospun scaffolds surfaces was assessed by static water contact angle measurements with an FTA 1000 instrument (First Ten Ångstroms, UK) (Figure 26). A 2 µL droplet of ultrapure water was deposited on each sample, and images were captured within 10 seconds to avoid evaporation artifacts. Measurements were repeated at five independent points per scaffold. Plasma-treated membranes were included in order to evaluate the improvement of hydrophilicity for enhanced cell adhesion.

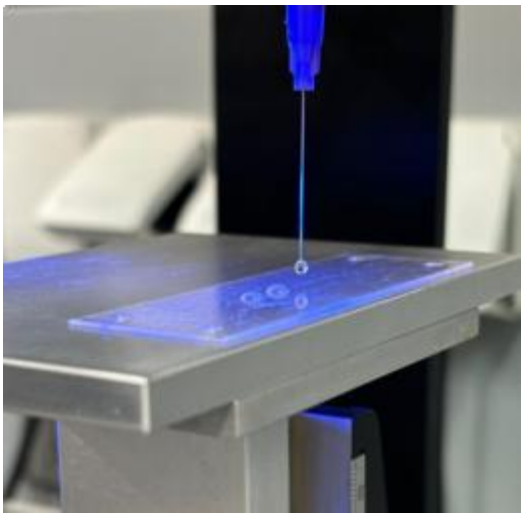

Figure 26 Static water contact angle measurement on ES surface using the FTA 1000 instrument (First Ten Ångstroms, UK).

2.6.6 Fourier-Transform Infrared spectroscopy (FTIR-ATR)

FTIR analysis (Thermo Scientific, Waltham, MA, USA)(Figure27) was performed to confirm the chemical composition of the PLA scaffolds and to detect potential structural modifications after processing and integration inside the microfluidic device. Spectra were collected in the range of 4000–600 cm^{-1} with a resolution of 4 cm^{-1} and 32 scans per sample. Characteristic PLA absorption bands, such as C=O stretching (~1750 cm^{-1}) and C–O stretching (1180–1080 cm^{-1}), were monitored to ensure material integrity.

Figure 27 FTIR analysis of PLA scaffolds performed with a Thermo Scientific spectrometer. Samples were analyzed before and after integration into the microfluidic devices to monitor potential structural modifications.

2.6.7 Differential scanning calorimetry (DSC)

Thermal properties of PLA scaffolds were investigated by differential scanning calorimetry (DSC, Mettler Toledo, Columbus, OH, USA). Samples of 5–10 mg were accurately weighed, sealed in aluminum pans, and analyzed under nitrogen flow. Two consecutive heating cycles were performed, from room temperature up to 200 °C, with a heating rate of 10 °C/min. The glass transition temperature (T_g) and melting temperature (T_m) were determined to evaluate the thermal stability of the scaffolds during the bonding process. The degree of crystallinity (X_c, %) was calculated according to Equation (7):

$$\chi_c\ (\%) = \frac{\Delta H_m - \Delta H_{cc}}{\Delta H^0_{PLA}} \times 100 \qquad (7)$$

where ΔH_m is the melting enthalpy, ΔH_{cc} is the cold crystallization enthalpy, and ΔH^0_{PLA} is the enthalpy of 100% crystalline PLA (93.7 J/g).

2.7 Rheological Characterization

The rheological properties of the polymeric solutions and the corresponding hydrogels were assessed using a Discovery Hybrid Rheometer (HR-10, TA Instruments) equipped with a plate–plate geometry and a Peltier system for precise temperature control (Figure 28). All measurements were carried out at 37 °C to mimic physiological conditions. Samples were prepared as discs with a height of 2 mm and a diameter of 6 cm.

Frequency sweep was conducted on both polymeric solutions and crosslinked hydrogels over the range 0.1–100 Hz at a constant strain of 1%, to evaluate the frequency-dependent viscoelastic response.

For each experimental condition, five independent replicates were analyzed to ensure reproducibility.

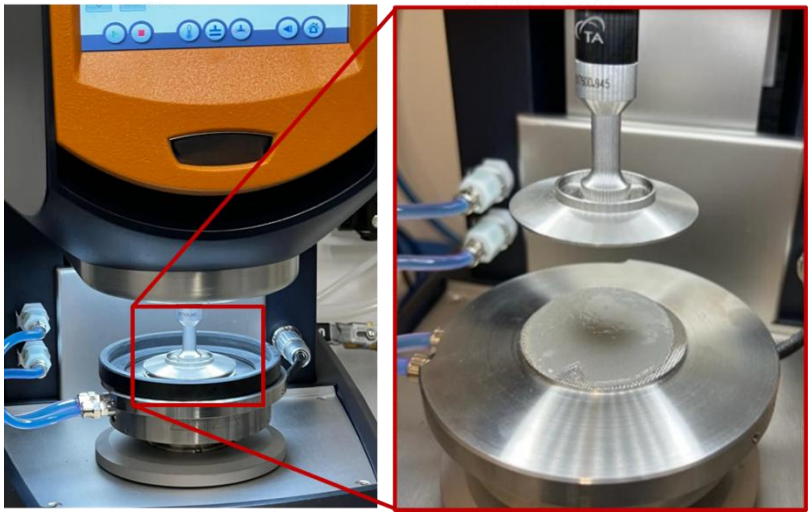

Figure 28Experimental setup for rheological characterization using a Discovery Hybrid Rheometer (HR-10, TA Instruments) equipped with a plate–plate geometry and Peltier cell for temperature control. The zoom highlights the measuring system with the upper plate in contact with the hydrogel sample positioned on the lower plate.

3 Results and Discussion: Fabrication Techniques

This chapter presents the experimental results obtained during the optimization and characterization of thermoplastic-based Organ-on-Chip (OoC) devices, with a focus on poly(methyl methacrylate) (PMMA) substrates and scaffold integration. The discussion is structured around three main aspects: (i) optimization of the laser micromachining process to ensure precise and reproducible microchannel fabrication; (ii) evaluation of the bonding strategy, optical transparency, and pressure resistance of the assembled devices; and (iii) assessment of connector sealing performance using commercial interfacing solutions.

The integration of these findings provides a comprehensive overview of the material's suitability for microfluidic applications, addressing both fabrication-related challenges and functional requirements. The results highlight the interplay between processing parameters and device performance, offering insights into how optimized settings can ensure mechanical robustness, optical quality, and operational reliability. Such considerations are critical for the development of standardized, reproducible, and user-friendly OoC platforms that can be translated into biological applications.

3.1 Laser Micromachining Optimization

Figure 29 reports optical micrographs (Dino-Lite microscope) of the ablated areas obtained at three laser power levels (20%, 40%, and 60%) combined with three scanning speeds (100, 200, and 300 mm s^{-1}). The analysis shows that low power or high scanning speed conditions resulted in shallow kerfs with limited ablation depth, indicating insufficient energy transfer to the substrate. Conversely, higher power and lower speeds generated deeper cuts, but also induced pronounced edge irregularities and local melting, attributable to excessive thermal input. Among the tested conditions, the intermediate setting (40% power at 200 mm s^{-1}) produced the most homogeneous kerf morphology, with well-defined edges and minimal evidence of thermal degradation. These findings highlight the critical role of optimizing the balance between laser power and scan speed to ensure reproducible and high-quality microchannel fabrication in PMMA substrates.

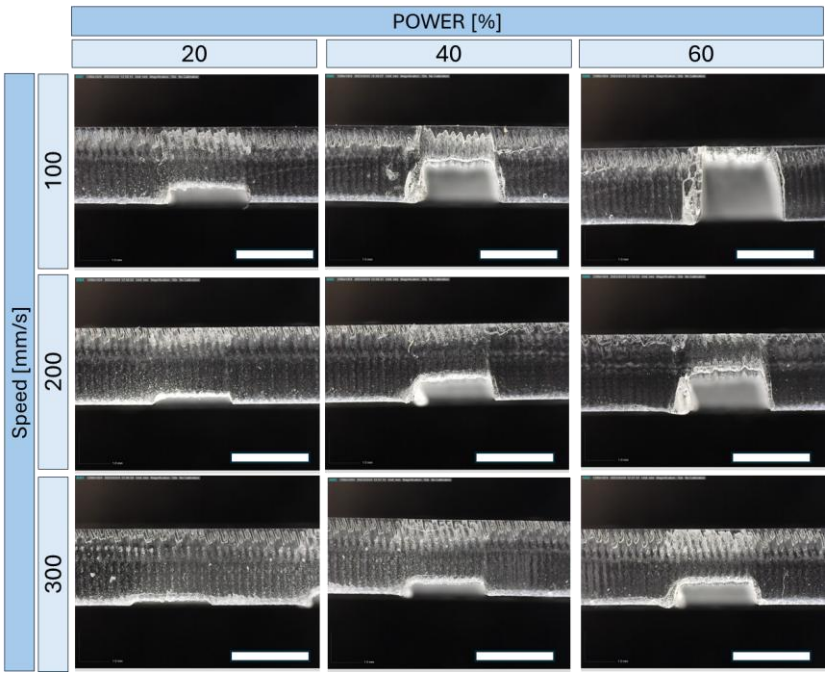

Figure 298 Cross-sectional optical micrographs of PMMA test cuts produced by CO_2 laser micromachining at various power and speed combinations. Columns correspond to power settings (20, 40 and 60 %) and rows to scanning speeds (100, 200 and 300 mm s^{-1}). Images acquired with a Dino-Lite optical microscope show that higher power and lower speed yield deeper but rougher cuts, while lower power and higher speed result in shallower kerfs

Figure 29 shows the quantitative evaluation of ablation depth in PMMA substrates as a function of laser scanning speed and power. As expected, an inverse correlation between scanning speed and ablation depth was observed for all power levels: higher traverse speeds reduced the interaction time between the laser beam and the polymer surface, thereby decreasing the energy delivered per unit area and resulting in shallower kerfs. Conversely, increasing the laser power led to greater penetration depths across all scanning conditions, with the maximum removal achieved at 60% power and 100 mm s^{-1}.

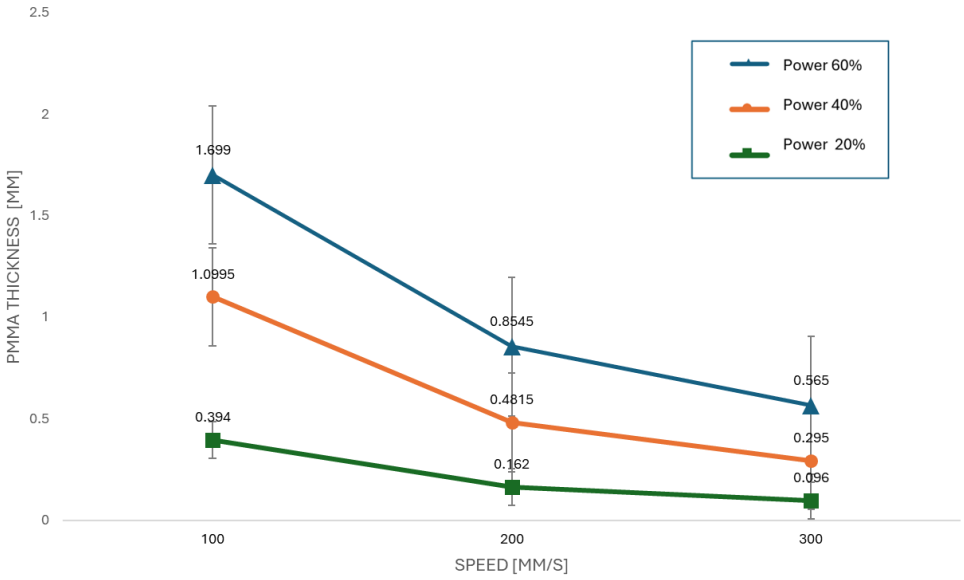

Figure 29 Effect of laser scanning speed and power on the ablation depth of PMMA substrates. Increasing the laser power enhanced material removal, while higher scanning speeds reduced ablation depth due to shorter interaction times. Error bars represent standard deviations (n = 3)

The intermediate regime (40% power, 200 mm s^{-1}), already identified as optimal in terms of kerf morphology (Figure 33), confirmed a balance between sufficient ablation depth and limited variability, with relatively low standard deviations compared to the other tested conditions. At the lowest power (20%), the ablation depth remained below 0.5 mm regardless of scan speed, highlighting the inadequacy of this setting for reproducible channel fabrication.

Overall, the combined analysis of micrographs and quantitative depth measurements demonstrates that both laser power and scanning speed must be carefully optimized to achieve well-defined and reproducible microstructures in PMMA.

3.2 Burst test

The ability of the fabricated devices to withstand internal pressure without leakage or structural failure was first evaluated through burst pressure testing. Figure 30 shows the pressure–time profile obtained for a 0.5 mm-thick PMMA prototype subjected to a constant flow rate of 1 mL/h. The pressure increased steadily with time and reached a plateau at approximately 460 kPa after ~23 s, representing the maximum resistance of the device under the applied conditions.

Figure 30 Burst pressure test of a 0.5 mm-thick PMMA device under a constant flow rate of 1 mL/h. The internal pressure increased progressively with time, reaching a plateau at approximately 460 kPa after ~23 seconds. The maximum resistance observed is significantly higher than typical operating pressures in microfluidic applications, confirming the robustness and sealing efficiency of the bonding strategy.

This threshold is significantly higher than the typical operating pressures in microfluidic systems, which usually range within a few tens of kPa, thereby confirming the suitability of PMMA devices for robust fluidic handling. The results not only validate the mechanical stability of the thermoplastic material but also demonstrate the effectiveness of the thermal bonding strategy in ensuring leakage-free operation. Such performance is particularly relevant in the context of OoC applications, where long-term perfusion and the preservation of sterile conditions are critical.

3.3 Bonding optical quality

The optical performance of PMMA before and after bonding was evaluated by UV–Vis spectroscopy. Figure 31 compares the transmittance spectra of a pristine 1 mm-thick PMMA sheet with those of two thermally bonded 0.5 mm layers. In both cases, the material

effectively blocked UV radiation below 360 nm while maintaining high optical transparency in the visible range, with transmittance values consistently above 91%.

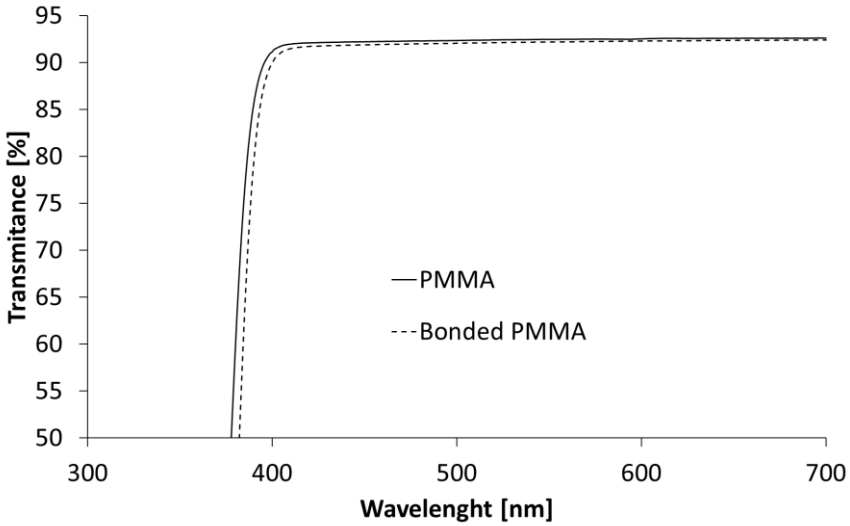

Figure 31 UV–Vis transmittance spectra of pristine PMMA (solid line) and bonded PMMA (dashed line). Both materials exhibit high transparency in the visible range, with only minimal differences after bonding, demonstrating the optical suitability of PMMA for Organ-on-Chip device fabrication.

The bonded configuration exhibited only a minor red-shift of approximately 5 nm, accompanied by a negligible reduction in transmittance (~0.5% at 410 nm). These variations are within the experimental tolerance and do not compromise device usability, indicating that the bonding process does not significantly alter the intrinsic optical properties of the polymer. This finding is particularly relevant for OoC applications, where real-time optical monitoring of cell cultures through phase-contrast or fluorescence microscopy requires substrates with high transparency.

3.4 Connector Sealing Evaluation

The outcomes of the pressure resistance tests are summarized in Figure 36, which reports the pressure profile over time for devices fabricated with different inlet port diameters. Devices with smaller inlet holes (2.46 mm and 2.47 mm) showed poor sealing, with early leakage and maximum pressures below 100 kPa. By contrast, devices with inlet diameters of 2.48 mm and 2.49 mm demonstrated significantly improved resistance, sustaining maximum pressures of 411 kPa and 507 kPa, respectively. These values are well above the

typical requirements for microfluidic applications, confirming the robustness of the bonding strategy.

It is worth noting that these tests were performed using commercial connectors (ChipShop mini plug type), in contrast to the earlier burst test (Figure 32), which employed screw fittings with ferrules. While the latter approach guaranteed high mechanical stability, it required multiple components to be sterilized and manually assembled, making handling more complex. In comparison, the commercial connectors offer a more streamlined and practical solution, requiring only sterile pliers for insertion and minimizing the manipulation steps. The systematic evaluation of different inlet diameters was therefore crucial to identify the optimal match between connector dimensions and applied pressure, ensuring leakage-free performance during operation.

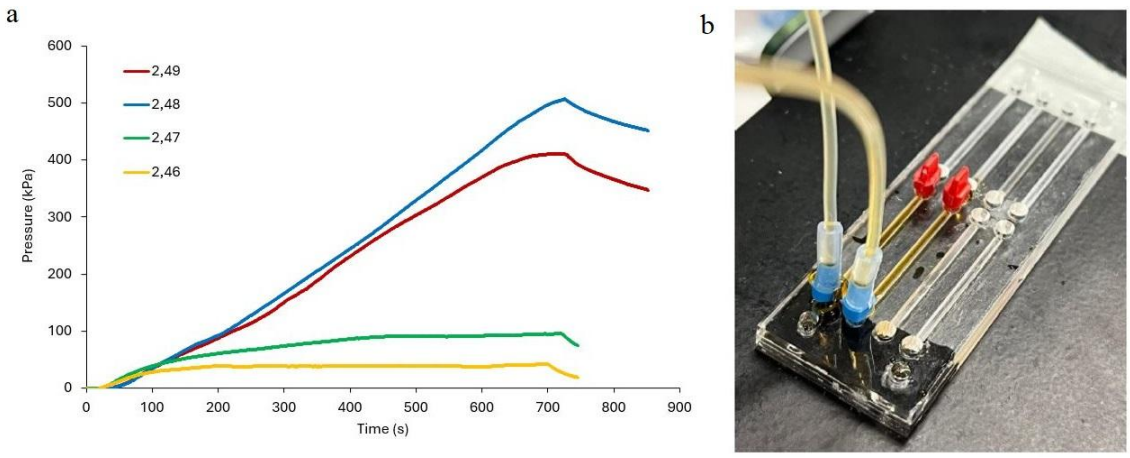

Figure 32 a) Burst test analysis of PMMA devices equipped with commercial connectors (ChipShop). Pressure–time profiles are shown for inlet port diameters of 2.46, 2.47, 2.48, and 2.49 mm. Devices with 2.48 and 2.49 mm diameters demonstrated the highest sealing performance, sustaining maximum pressures above 400 kPa, whereas smaller diameters exhibited early leakage and lower resistance. (b) Photograph of the assembled device during testing, showing connectors and tubing integrated into the microfluidic chip.

Among the tested conditions, the 2.48 mm configuration was selected as the most suitable for subsequent fabrication, providing the best balance between sealing efficiency and reproducibility. Although minor leakage was observed in all samples—most likely due to small misalignments during layer stacking—the 2.48 mm design consistently withstood pressures above 500 kPa. This exceeds by far the pressure range commonly encountered in microfluidic systems, validating the device architecture and confirming its suitability for downstream biological studies.

3.5 Scaffold Morphology

Since the device assembly required a thermal pressing step (70 °C for 180 s in the presence of ethanol), it was first necessary to assess whether this treatment could alter scaffold morphology. Figure 33A and 33B show representative SEM micrographs of electrospun PLA scaffolds with either aligned (A-PLA) or random (R-PLA) fibre orientation, collected immediately after fabrication. In both cases, fibres appeared continuous, smooth, and free of surface defects, with clear evidence of alignment in A-PLA scaffolds obtained using a high-speed rotating collector.

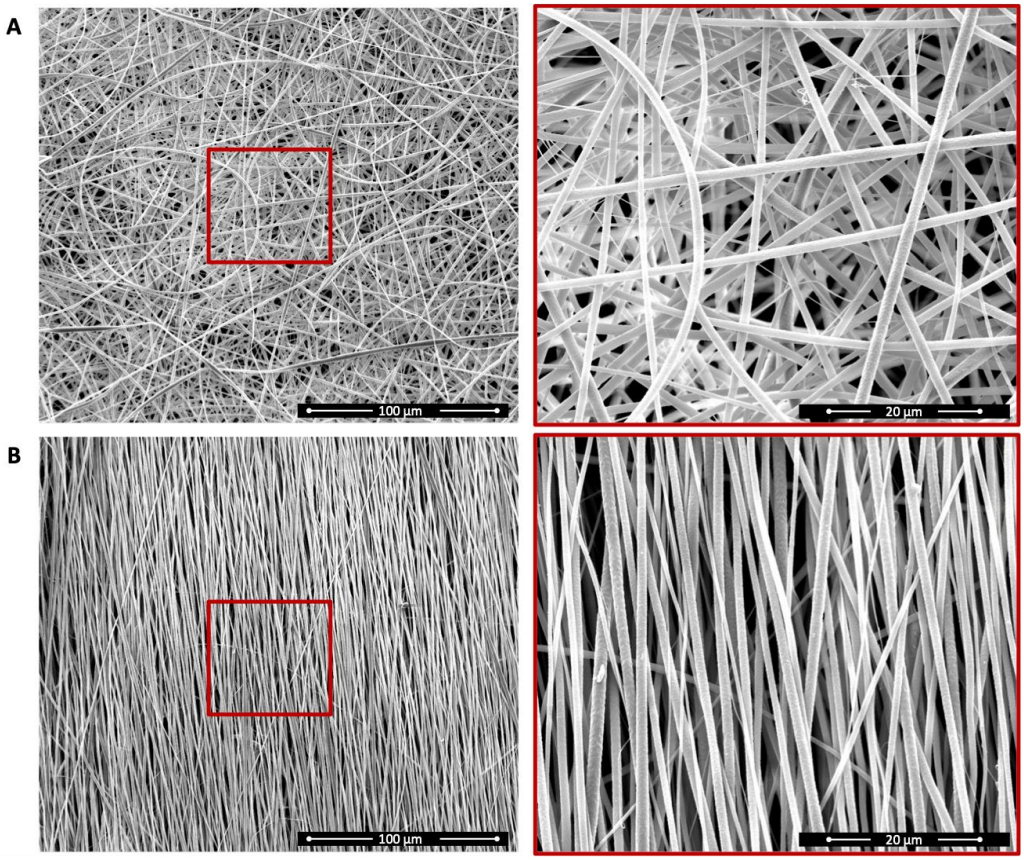

Figure 33 SEM micrographs of electrospun PLA scaffolds with different fibre orientations.
(A) Randomly oriented fibres (R-PLA) displaying a highly entangled structure with heterogeneous pore distribution.
(B) Aligned fibres (A-PLA) obtained using a high-speed rotating collector, showing parallel arrangement and reduced inter-fibre spacing.
Images on the left represent low-magnification views (scale bar = 100 µm), while the corresponding high-magnification details are shown on the right (scale bar = 20 µm).

Quantitative analysis revealed average fibre diameters of 1.29 µm for A-PLA and 1.39 µm for R-PLA. Although modest, this difference is consistent with the additional stretching forces applied during high-speed collection, which promote fibre elongation [61].

Structural differences were also reflected in fibre packing: aligned scaffolds displayed tighter fibre organization and reduced inter-fibre spacing compared to random ones. This was corroborated by porosity analysis, which yielded values of 75.4% ± 3.2% for A-PLA and 63.8% ± 3.8% for R-PLA, confirming that fibre orientation directly influences scaffold architecture.

Following integration into the microfluidic devices, scaffold morphology was further examined (Figure 34). Overall, the electrospun structures retained their microstructural integrity, demonstrating that the selected fabrication process allows scaffold incorporation without major alterations. Minor modifications were nonetheless observed: fibres appeared slightly fused at contact points, likely due to localized thermal or mechanical effects during bonding. In addition, aligned fibres exhibited a more undulated morphology compared to their pre-assembled state. It is unclear whether this waviness originated from the chip assembly process itself or from the disassembly procedure required for SEM imaging. Importantly, average fibre diameters remained unaffected, indicating that scaffold functionality as a biomimetic support was preserved after device fabrication.

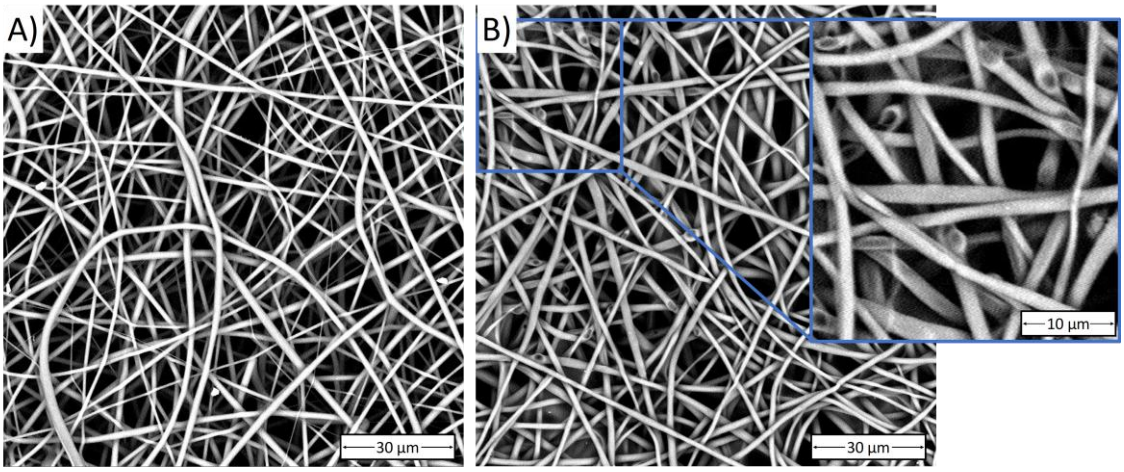

Figure 34 SEM micrographs of electrospun PLA scaffolds after integration into microfluidic devices. (A) Representative view of scaffold morphology showing overall preservation of microstructural integrity. (B) Higher-magnification image highlighting fibre contacts, where slight fusing and localized thermal effects can be observed. The inset provides a closer view (scale bar = 10 µm), evidencing minor fibre undulations while maintaining comparable diameters to pre-assembled scaffolds.

SEM analyses were also performed on aligned electrospun scaffolds, which exhibited comparable morphological outcomes. However, for brevity, these images are presented in the *Brain-on-Chip* chapter, where a direct comparison between aligned and random scaffolds is discussed in the context of the cellular model employed.

3.6 ESs Mechanical Properties

The mechanical behaviour of the electrospun scaffolds was strongly influenced by fibre orientation, as evidenced by the distinct stress–strain profiles obtained for random-fibre (R-PLA) and aligned-fibre (A-PLA) samples.

The stress–strain curves of R-PLA scaffolds (Figure 35) exhibited the typical response of a ductile material, characterised by a relatively low elastic modulus (~80 MPa) and a high strain at break (~60%). The progressive monotonic increase of stress until fracture can be explained by the gradual reorientation of fibres under axial loading: as the load increases, randomly distributed fibres align in the loading direction, enhancing the overall resistance of the scaffold before failure.

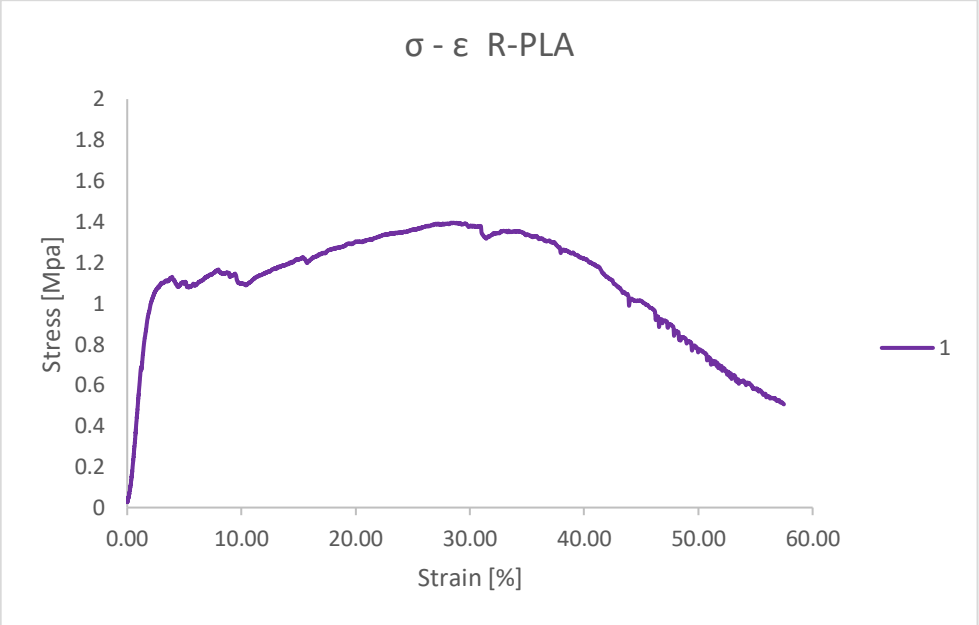

Figure 35 Representative stress–strain curves of random PLA (R-PLA) electrospun scaffolds. These samples exhibited the typical ductile behaviour of randomly oriented fibrous mats, with a relatively low elastic modulus (~80 MPa) and maximum stress below 2 MPa. The curves show a progressive increase in stress up to fracture, with an average strain at break of ~60%, reflecting fibre reorientation and gradual load redistribution during deformation.

In contrast, A-PLA scaffolds (Figure 36) displayed a markedly stiffer and more brittle behaviour, with an elastic modulus of ~700 MPa and an average strain at break of ~37%. Unlike R-PLA, the fibres in A-PLA were already oriented along the direction of the applied load, preventing progressive reorientation during tensile testing. As a result, the stress–strain curve exhibited a pronounced plastic plateau, followed by an abrupt fracture. Notably, the maximum stress sustained by A-PLA scaffolds was approximately tenfold higher than that of R-PLA, further confirming the reinforcing effect of fibre alignment.

Porosity was also evaluated as a factor potentially influencing mechanical behaviour. PLA-R scaffolds exhibited slightly higher porosity (~62%) compared to A-PLA (~50%). However, this modest difference cannot account for the significant variations observed in mechanical performance, indicating that fibre orientation is the dominant parameter governing scaffold mechanics.

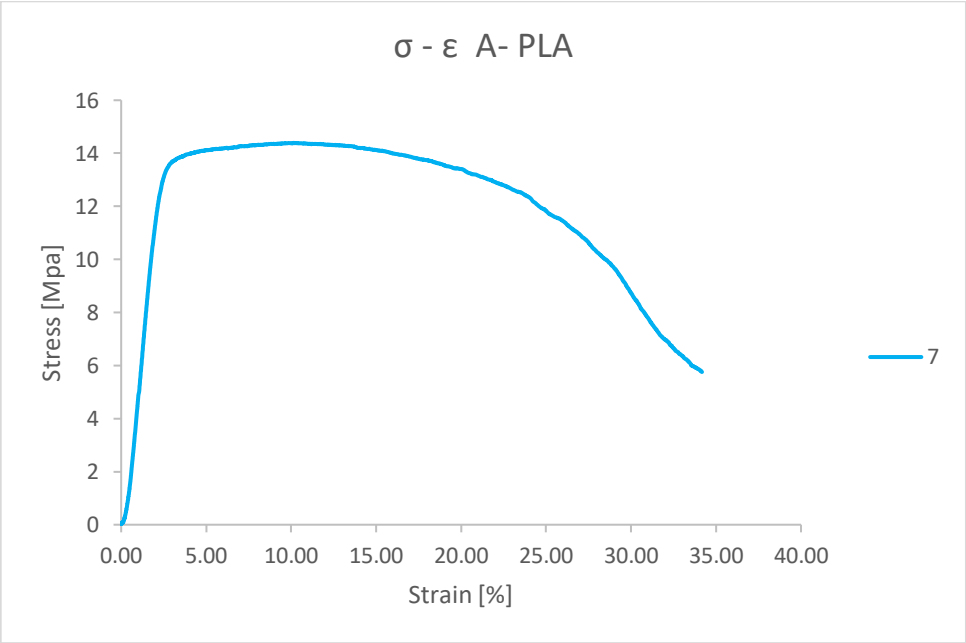

Figure 36 Representative stress–strain curves of aligned PLA (A-PLA) electrospun scaffolds. The samples exhibited a stiff mechanical response, with an average elastic modulus of ~700 MPa and a maximum stress approximately tenfold higher than that of random-fibre scaffolds. The curves are characterised by an initial linear elastic region, followed by a plastic plateau and abrupt fracture at an average strain of ~37%, reflecting the influence of fibre alignment on scaffold mechanics.

Porosity was also considered as a potential factor influencing mechanical behaviour. R-PLA scaffolds showed a porosity of ~62%, slightly higher than A-PLA scaffolds (~50%). However, this modest difference in porosity does not account for the substantial variations observed in mechanical properties. Therefore, it can be concluded that the mechanical performance of the scaffolds is governed primarily by fibre orientation rather than porosity.

3.7 Water contact angle (WCA)

The surface wettability of the electrospun scaffolds was evaluated by water contact angle (WCA) measurements to assess their hydrophilic/hydrophobic character (Figure 37).

Untreated PLA scaffolds displayed a highly hydrophobic behaviour, with an average WCA of 127° ± 8°, in line with the intrinsic properties of the polymer. Upon oxygen plasma treatment, the contact angle was drastically reduced to 0°, as the water droplet was immediately absorbed, confirming the strong increase in surface hydrophilicity induced by plasma functionalisation. However, following scaffold integration into the device through thermal bonding, the WCA increased to 63.1° ± 3.8°, despite the prior plasma activation. This partial loss of wettability can be attributed to the well-documented ageing effect of plasma-treated polymers, where polar functional groups progressively reorient or migrate into the polymer bulk to minimise surface energy [62].

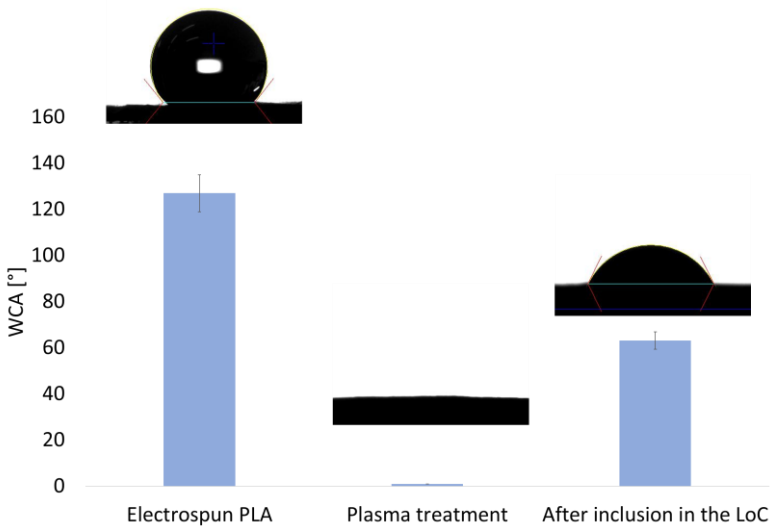

Figure 37 Water contact angle (WCA) measurements of electrospun PLA scaffolds in three conditions: pristine PLA (127° ± 8°), after oxygen plasma treatment (0° due to complete droplet absorption), and after integration into the chip through thermal bonding (63.1° ± 3.8°). Insets show representative images of water droplets on the scaffold surfaces. Results demonstrate the intrinsic hydrophobicity of PLA, the strong hydrophilicity induced by plasma activation, and the partial recovery of hydrophobicity following bonding, consistent with the ageing and surface rearrangement phenomena of plasma-treated polymers.

In the present case, the thermal bonding step at 70 °C—slightly above the glass transition temperature of PLA—likely accelerated this process by enhancing chain mobility and favouring surface rearrangements.

3.8 Fourier-transform infrared spectroscopy (FTIR/ATR)

To qualitatively investigate the effect of thermal bonding in the presence of ethanol on the chemical structure of PLA scaffolds, FT-IR/ATR spectroscopy was performed (Figure 38A). The FT-IR/ATR spectrum of PLA displayed characteristic absorption bands at 1747 cm^{-1}, corresponding to C=O stretching vibrations of the ester groups; at 1180 cm^{-1}, 1129 cm^{-1}, and 1083 cm^{-1}, associated with C–O stretching; and at 1044 cm^{-1}, attributed to O–H bending [63] (Figure 38B).

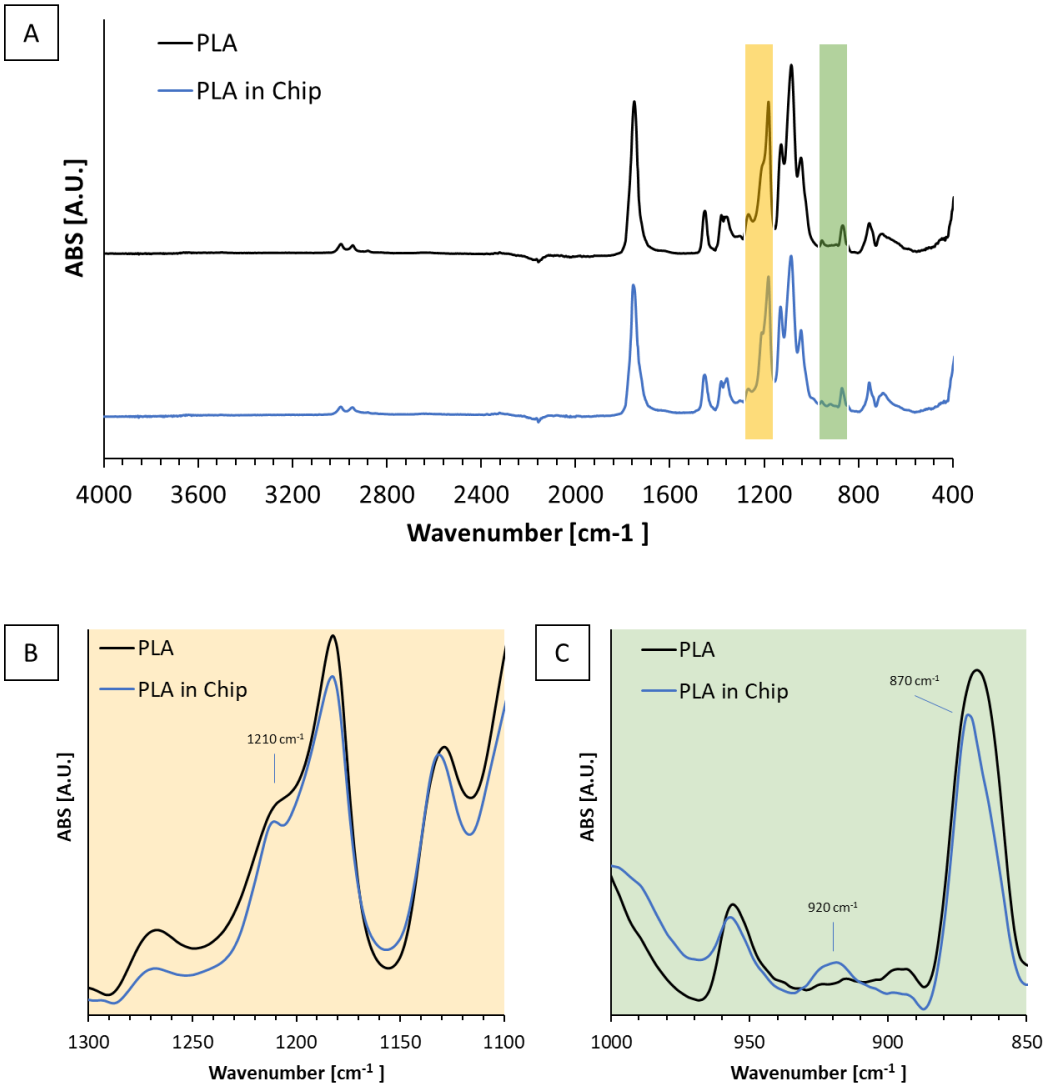

Figure 38 FT-IR/ATR spectra of electrospun PLA scaffolds before and after integration into the device. (A) Full spectra of pristine PLA (black) and PLA after bonding (blue), highlighting characteristic absorption bands. (B) Magnified view of the 1210 cm^{-1} region, where the shoulder at 1207 cm^{-1} in pristine PLA evolves into a defined peak after bonding, indicating increased crystallinity. (C) Magnified view of the 920–870 cm^{-1} region, showing enhanced intensity at 920 cm^{-1} and reduced intensity at 871 cm^{-1}, consistent with a crystalline-to-amorphous shift induced by the assembly process.

Additional absorption bands at 1207 cm^{-1} (alkyl-ketone chain vibrations) and 920 cm^{-1} (flexural C–H bond vibrations) are representative of the crystalline domains of PLA [64]. After integration of the electrospun scaffold within the device, the shoulder at 1207 cm^{-1} became a more defined peak shifted to 1210 cm^{-1}, and the intensity of the 920 cm^{-1} band increased, indicating a higher degree of crystalline organisation (Figure 42C).Conversely, the decrease in intensity at 871 cm^{-1}, which is associated with the amorphous phase of PLA [65], further supports a shift in the crystalline-to-amorphous ratio.

Taken together, these spectroscopic observations demonstrate that the integration process of electrospun PLA scaffolds into the device modifies their crystalline structure, resulting in an overall increase in polymer crystallinity.

3.9 Differential scanning calorimetry (DSC)

The DSC analysis was carried out to evaluate whether the thermobonding procedure adopted for integrating the electrospun PLA scaffolds into the microfluidic devices induced changes in their thermal behaviour (Figure 39). During the first heating ramp, the pristine electrospun PLA exhibited the typical features of a semicrystalline polymer, with a glass transition temperature (Tg) at ~61 °C, a cold crystallization exotherm (Tcc) around 100 °C, and a melting endotherm (Tm) at ~154 °C. After integration into the device, a marked reduction of the Tg and Tcc signals was observed, while the melting peak remained essentially unchanged (Tm ≈ 153 °C).

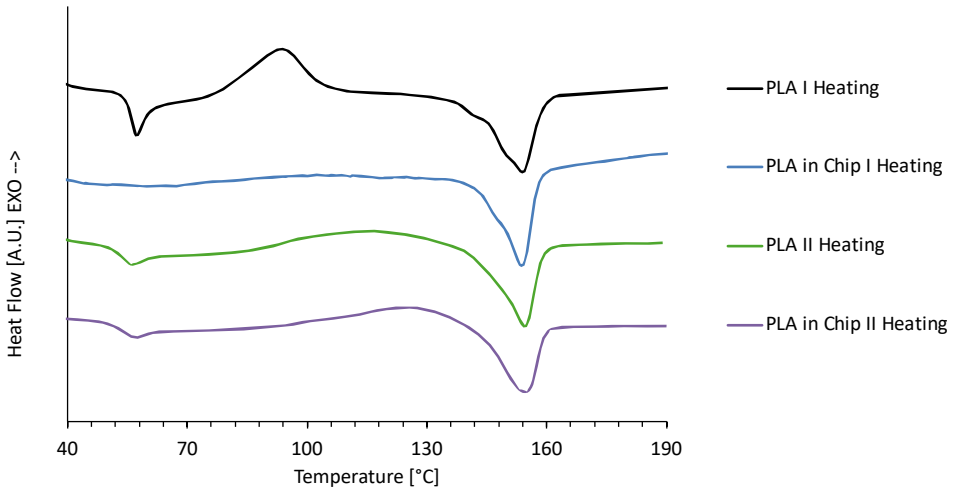

Figure 39 Differential scanning calorimetry (DSC) thermograms of electrospun PLA scaffolds before and after integration into the microfluidic device. The pristine scaffold (purple) shows the typical features of a semicrystalline PLA: glass transition (Tg ~61 °C), cold crystallization (Tcc ~100 °C), and melting (Tm ~154 °C). After integration (green), the cold crystallization peak is strongly reduced, while the melting behaviour remains essentially unchanged. A

second heating ramp (blue) performed to erase the thermal history produced overlapping curves for both pristine and integrated scaffolds, confirming that the bonding process primarily increases crystallinity through physical reorganisation without altering the PLA molecular structure.

This behaviour suggests that the bonding process, which involves simultaneous exposure to heat and ethanol, promotes the growth of crystalline domains within the scaffold. In agreement with literature reports, even short ethanol treatments at moderate temperatures have been shown to suppress cold crystallization in electrospun PLA due to polymer chain plasticization.

Consistently, the scaffolds recovered from sealed devices exhibited a pronounced increase in crystallinity, from ~9.5% in the pristine mats to ~25%, despite only minimal variations in melting enthalpy (~24 J g^{-1}). The quantitative thermal transitions obtained from DSC are summarised in Table 3, which confirms the suppression of cold crystallization and the increase in crystallinity following integration.

Table 3 Thermal properties of PLA electrospun scaffolds before and after integration in the devices..

Sample	***T_g (°C)***	***T_{cc} (°C)***	***T_m (°C)***	***ΔH_{cc} (j/g)***	***ΔH_m (j/g)***	***χ (%)***
First Heating						
PLA	61.50	100.10	154.26	14.83	23.65	9.41
PLA in Chip	-	102.37	153.48	1.39	24.76	24.94
Second Heating						
PLA	56.20	118.40	154.82	5.11	16.87	12.55
PLA in Chip	57.08	126.00	155.09	7.38	20.03	13.50

The second heating ramp, performed to erase the thermal history of the samples, resulted in nearly overlapping thermograms for both pristine and integrated scaffolds. This indicates that the bonding process primarily influences the degree of crystallinity through physical reorganisation of polymer chains, without inducing permanent modifications of the PLA molecular structure.

3.10 Hydrogel Rheology

3.10.1 Frequency Sweep: Polymeric Solution vs. Hydrogel

Figure 40 shows the frequency-dependent viscoelastic behaviour of the polymeric precursor solution (A) and the corresponding ionically crosslinked hydrogel (B). As expected, the polymeric solution exhibited a predominant viscous response, with the loss modulus (G″) higher than the storage modulus (G′), which is typical of polymer solutions before gelation. Conversely, the crosslinked hydrogel displayed a solid-like behavior, characterized by G′ values consistently higher than G″ across the investigated frequency range.

The storage modulus (G′) of the hydrogel remained nearly constant with increasing frequency, indicating a stable elastic network and confirming the efficiency of the ionic crosslinking process. The relatively flat G′ curve and the marked difference between G′ and G″ are indicative of a well-formed, elastic hydrogel structure. Overall, these results confirm that crosslinking significantly enhances the mechanical stiffness and structural integrity of the polymeric matrix, ensuring its suitability for integration within the microfluidic device.

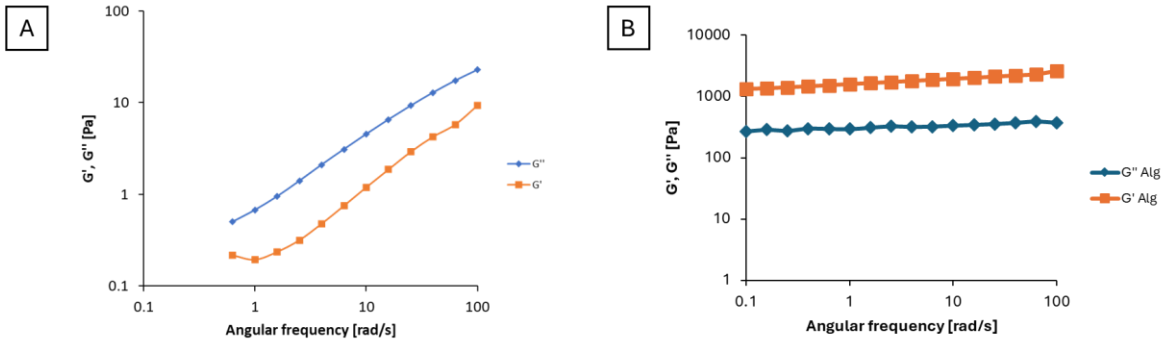

Figure 40 Frequency-dependent storage (G') and loss (G") moduli of (A) the polymeric precursor solution and (B) the ionically crosslinked hydrogel.

Frequency-dependent complex viscosity (η*) of (A) the polymeric precursor solution and (B) the corresponding ionically crosslinked hydrogel are shown in Figure 41. The polymeric solution (Figure 41 A) exhibit a shear-thinning (pseudoplastic) behavior at low frequencies, as evidenced by the decrease in complex viscosity with increasing angular frequency. This behavior is typical of a polymeric solution in which the molecular chains or network structures progressively align along the flow direction, reducing internal resistance.

The viscosity curve tends to flatten at medium frequencies, indicating a pseudo-Newtonian regime in which polymer chains are randomly oriented and the system behaves as a viscous liquid. In contrast, the crosslinked hydrogel (B) displays higher viscosity values and a weaker frequency dependence, consistent with the presence of a stable 3D crosslinked network that resists deformation.

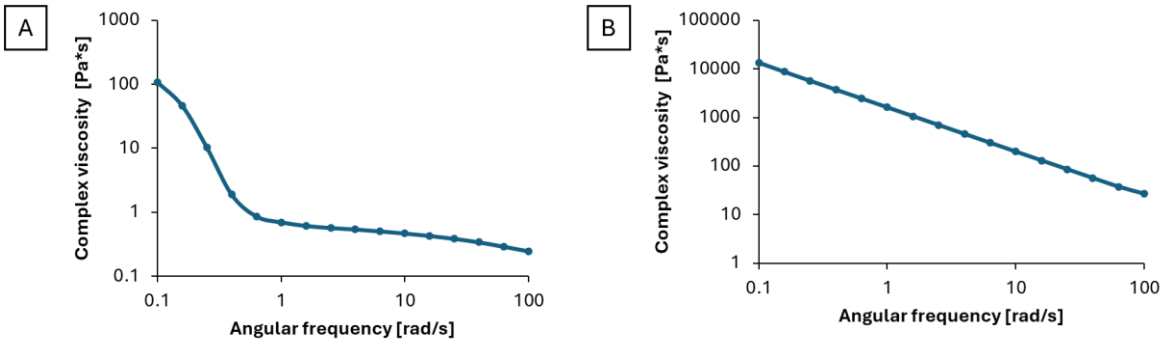

Figure 41 Frequency-dependent complex viscosity (η) of (A) the polymeric precursor solution and (B) the ionically crosslinked hydrogel.*

Overall, the observed rheological profiles confirm that ionic crosslinking markedly enhances structural integrity and mechanical stability, transitioning the material from a predominantly viscous liquid to an elastic solid-like gel suitable for microfluidic integration and long-term biological applications.

4 Liver on Chip

A multicompartment Liver-on-Chip (LoC) platform has been engineered by combining laser-patterned PMMA substrates with an electrospun PLA scaffold that recreates the liver's extracellular matrix morphology [66]. To mimic *in vivo* systemic conditions, a dual-chamber LoC system was developed to model the chronic delivery of colorectal cancer-derived extracellular vesicles (EVs) and investigate their role in the formation of pre-metastatic niches in the human liver. In this configuration, THLE-2 cells were seeded in the upper chamber and were subsequently exposed to EVs perfused through the lower chamber, which diffuse across an electrospun PLA scaffold acting as a porous basement-membrane-like barrier (Figure 46). In extracellular vesicle (EV) research, conventional 2D culture systems require acute, high-dose administrations of EVs to target cells. Such conditions are often criticized during peer review or grant evaluation because they do not reflect the physiological scenario, where cells are exposed to continuous low concentrations of EVs rather than acute stress-inducing doses [67]. To overcome these limitations, 3D dynamic culture platforms provide a more realistic model for chronic EVs delivery. This is particularly relevant in cancer biology, where EVs released from primary tumours contribute to the establishment of pre-metastatic niches (PMNs) that favour colonization of secondary sites [68] (Figure 42A).

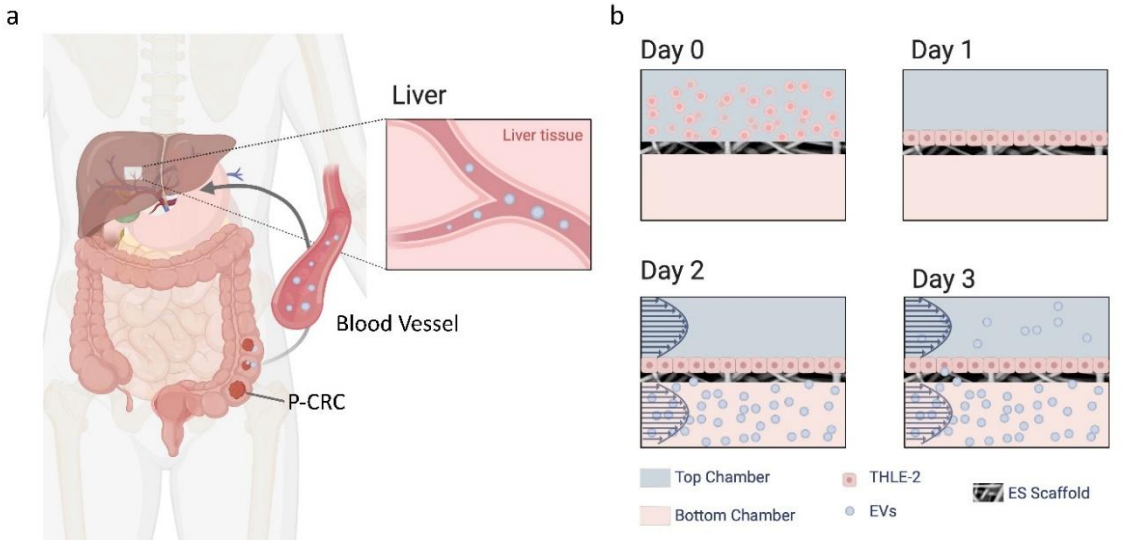

Figure 42. Panel (a) schematically represents the systemic route of colorectal cancer–derived extracellular vesicles (EVs), released from the primary tumour and transported through the bloodstream to the liver, where they can contribute to the formation of a pre-metastatic niche. Panel (b) depicts the experimental design of the dual-chamber LoC system: THLE-2 hepatocytes are seeded in the top chamber, while EVs are perfused through the bottom chamber. The electrospun PLA scaffold functions as a porous basement-membrane-like interface, enabling the progressive diffusion of EVs from the lower to the upper compartment. Over time (Days 0–3), this configuration ensures a chronic and physiologically relevant exposure of hepatocytes to tumour-derived EVs, closely mimicking the in vivo situation.

This configuration supports the continuous delivery of colorectal cancer-derived extracellular vesicles under physiologically relevant flow, exploiting the low absorption, optical clarity and reproducibility of thermoplastics alongside the biomimetic architecture of electrospun fibres.

4.1 Rationale of The LoC

The design of the multicompartment Liver-on-Chip (LoC) platform was conceived to overcome the intrinsic limitations of conventional 2D cultures and static transwell-like systems in modelling complex liver–tumour interactions (Figure 43). Conventional substrates fail to recapitulate the three-dimensional extracellular matrix (ECM) environment and lack the dynamic exchange of metabolites and signaling cues that are fundamental for hepatocyte functionality and response to extracellular vesicles (EVs).

To address these gaps, the LoC integrates a laser-patterned poly(methyl methacrylate) (PMMA) body with an electrospun poly(lactic acid) (PLA) scaffold, which serves a dual function as both a biomimetic ECM-like substrate for hepatocyte culture and as a semi-permeable barrier mimicking the liver basement membrane [69]. The incorporation of PLA microfibres provides a physiologically relevant architecture that enhances hepatocyte differentiation, as confirmed by proteomic analyses, while the use of PMMA ensures low absorption of hydrophobic drugs, high optical clarity and reproducible fabrication via laser micromachining [70].

Separate perfusion in the upper and lower channels permits the independent control of shear stress and nutrient gradients while enabling dynamic administration of EVs and future co-culture.

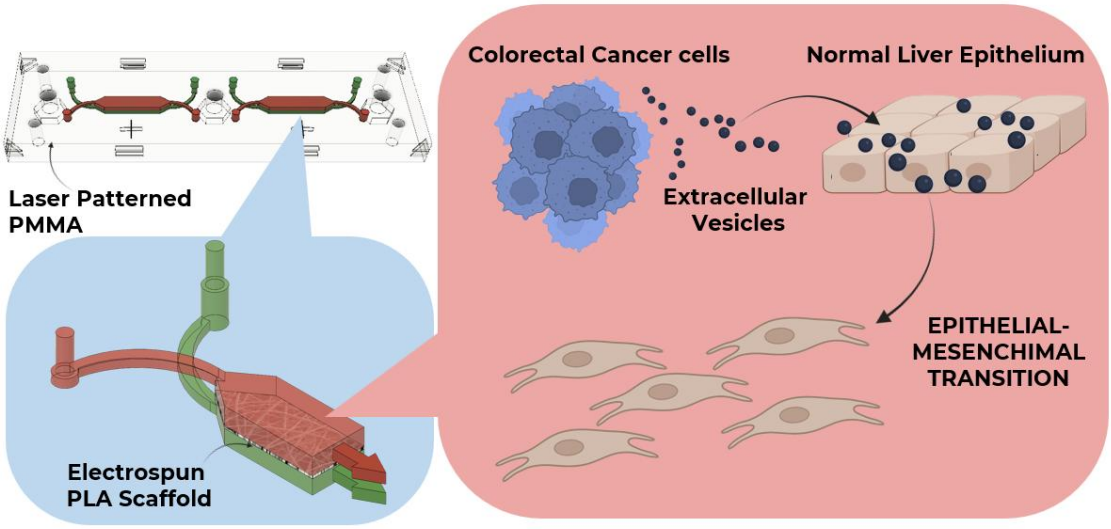

Figure 43 Graphical summary of the Liver-on-Chip experimental concept. Left: exploded view of the multilayer Organ-on-Chip device combining laser-patterned PMMA with an electrospun PLA scaffold to create a perfused 3-D culture chamber. Right: schematic illustration of the biological study, where extracellular vesicles (EVs) released by colorectal cancer cells are delivered through the chip to a normal liver epithelium, triggering an epithelial-to-mesenchymal transition (EMT).

This modular design also facilitates the chronic delivery of tumour-derived extracellular vesicles (EVs) under continuous flow. By placing the scaffold between two microchannels, EV-laden medium can be introduced into one channel while clean medium perfuses the opposite side, creating a controlled gradient across the 3D tissue.

4.2 Liver-on-Chip design and fabrication

The design of the culture chamber of the LoC proposed in this work consists of a top culture chamber cultured with immortalized human hepatocytes, a bottom perfusion chamber where tumour derived EVs are flow injected, and a middle layer composed of a thin R-PLA scaffold interfacing with the top and bottom chamber (Figure 44A). The electrospun scaffold serves both as a separator between the two compartments and as a biomimetic substrate for cell culture. Additionally, it acts as an extra barrier to the passage of EVs from the lower to the upper chamber, mimicking the role of the endothelial layer and the basement membrane, to which hepatocytes adhere *in vivo*.

The microfluidic device incorporates two independent dual-chamber units, enabling duplicate experiments to be carried out within a single platform. Each LoC module consists

of two semi-chambers, each equipped with dedicated inlets and outlets for controlled perfusion (Figure 44B).

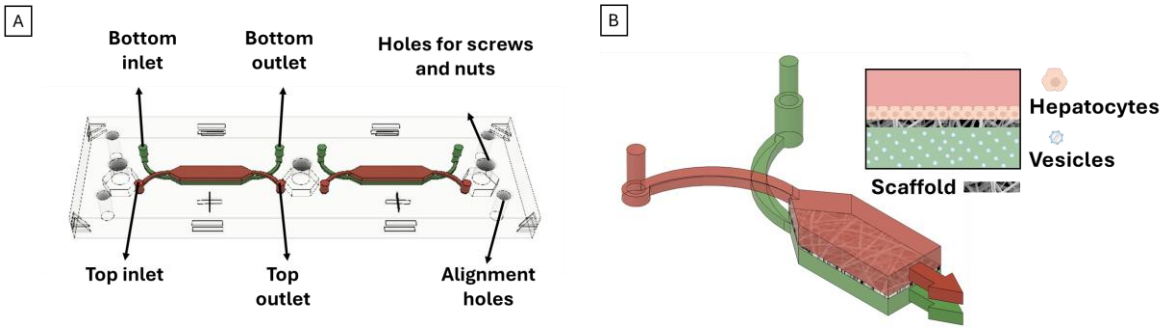

Figure 44 Schematic representation of the Liver-on-Chip (LoC) device developed in this work. (A) Exploded view of the microfluidic architecture, showing the dual-chamber configuration with independent inlets/outlets and alignment features. (B) Sectional view of a single LoC module highlighting the top culture chamber seeded with immortalized human hepatocytes, the bottom perfusion chamber for EV injection, and the intermediate R-PLA electrospun scaffold. The scaffold acts as both a physical separator and a biomimetic substrate, providing a barrier to EV passage while mimicking the basement membrane and endothelial layer to which hepatocytes adhere in vivo.

The hexagonal culture chamber has a total area of 0.417 cm^2, which drops to 0.33 cm^2 when the triangular inlet and outlet regions are excluded—making it comparable to the culture surface of a standard 96-well plate. The upper chamber is 1 mm high and holds 41.7 µL (33 µL excluding the inlet/outlet regions), while the lower chamber is slightly shallower due to a 100 µm recess for the electrospun scaffold and therefore contains 37.5 µL in total or 29.7 µL excluding the triangular regions.

Based on physiological hepatic blood flow—approximately 20.5 mL of blood per millilitre of liver tissue—the chosen volume allows culture of up to 4.6×10^5 hepatocytes, which is an order of magnitude greater than the seeding density used in our experiments (5×10^4 cells per chamber) [71].

To facilitate assembly, the CAD model incorporates alignment holes, screw holes, and "plus" and "minus" symbols to identify inlets and outlets. Figure 45 illustrates the fully assembled LoC with its tubing connectors, ferrules, and screws.

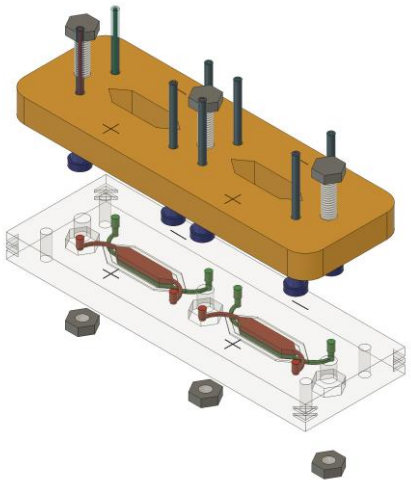

Figure 45 Exploded CAD view of the Liver-on-Chip (LoC) assembly. The design integrates alignment holes, screw holes, and inlet/outlet identifiers ("+" and "–") to facilitate accurate assembly and fluidic connection. The device is secured using screws, nuts, and ferrules, ensuring robust sealing and stable integration of tubing connectors for perfusion experiments.

The CAD device is composed of multiple PMMA layers of different thicknesses and specific functions Figure 46:

I. The first layer (2 mm) contains the inlet and outlet ports for both the upper and lower chambers. To facilitate identification, "+" and "–" signs are engraved on the surface, with "+" indicating access to the upper chamber and "–" indicating access to the lower chamber. Four alignment holes are located at the corners to ensure correct positioning of the layers during assembly.

II. The second layer (0.5 mm) incorporates the inlet/outlet for the lower chamber, the access channels to the upper chamber, and defines the hexagonal geometry of the culture chamber. Rounded corners are included to facilitate device opening.

III. The thirth layer (0.5 mm) contains the lower inlet/outlet and two hexagonal apertures, allowing closure of the scaffolded chamber.

IV. The fourth layer (0.5 mm) features entry holes to the lower chamber and two hexagonal apertures. Engraved areas around each hole improve scaffold adhesion to the surface.

V. The fifth layer (0.5 mm) includes hexagonal apertures and channels for access to the lower chamber. As in the third layer, bevelled corners facilitate handling and opening.

VI. The sixth and final layer (2 mm) serves as the base of the device, sealing the chip.

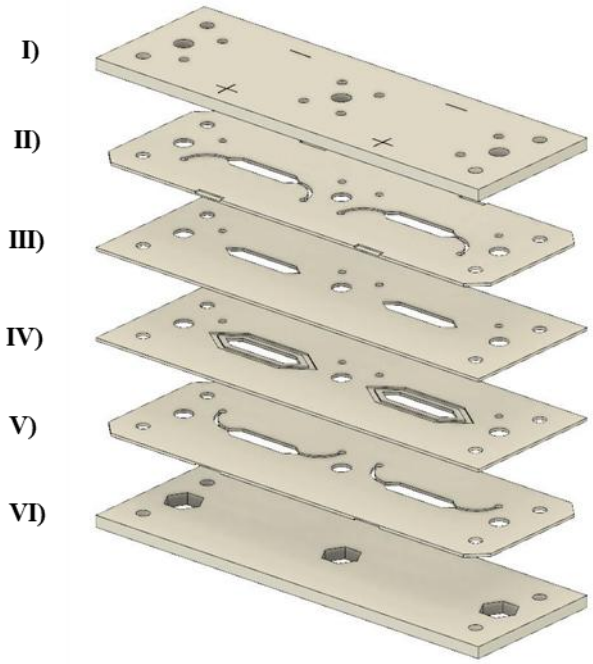

Figure 46 CAD design of the exploded view of the LoC into its six functional layers.

Figure 47 reports the technical drawings of the individual device layers, including the main dimensions, hole diameters and positioning of the channels. Each panel (I–VI) corresponds to one of the intermediate PMMA layers, highlighting the precise measurements of the inlets/outlets, alignment holes, and chamber geometries.

The inclusion of these schematics provides a clear overview of the laser-cutting design used during fabrication and ensures reproducibility of the assembly process. The detailed dimensions also emphasize the progressive evolution of the chamber layout and connector integration across the different layers, facilitating accurate alignment and fluidic sealing once the device is assembled.

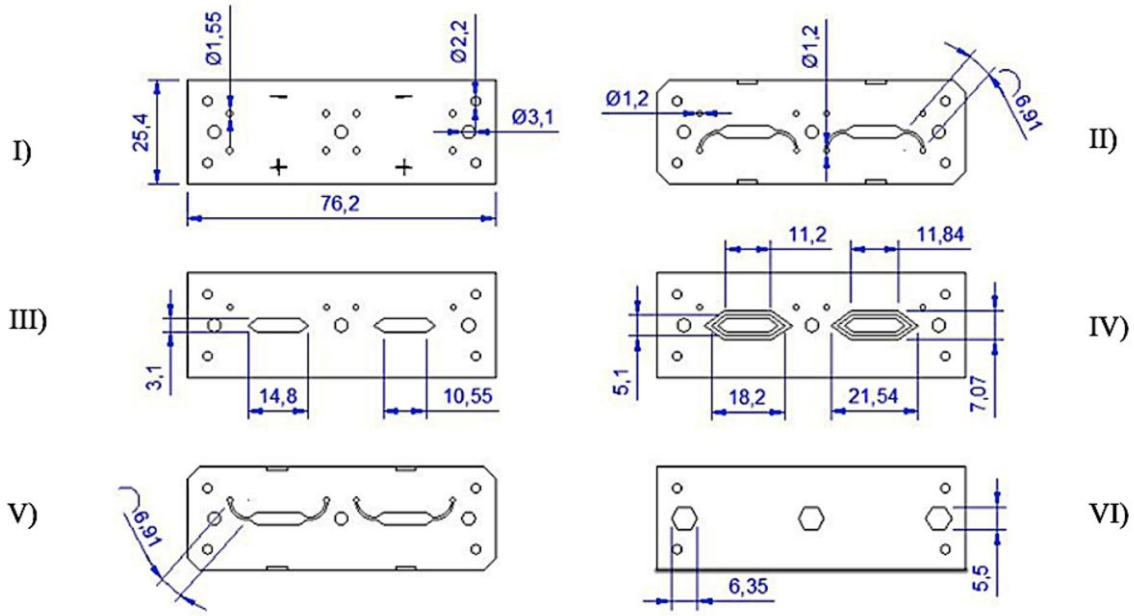

Figure 47 Geometrical details of the six PMMA layers composing the Liver-on-Chip (LoC) device. Dimensions of channels, holes, and alignment features are reported in millimetres (mm).

To perform the fabrication process via laser cutter, the multilayer design of the device was imported into the Autolaser software, which allowed precise control of the CO_2 laser cutter parameters. Figure 48 shows the representation of the device and scaffold layout within the software, where the different cutting and engraving operations are highlighted by colour codes corresponding to specific combinations of laser power and speed. This approach ensured reproducible and accurate machining of the PMMA sheets and membrane, enabling the creation of the inlet/outlet ports, channels, and alignment holes required for assembly.

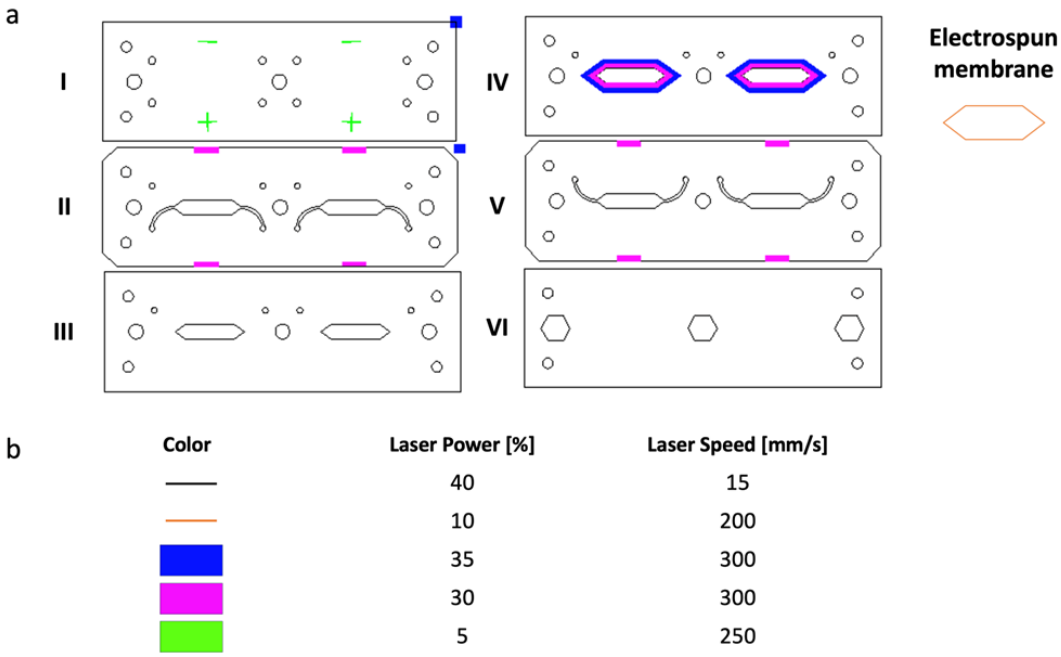

Figure 48 Representation of the chip design imported into Autolaser software for CO_2 laser cutting and engraving. (a) Layout of the six PMMA layers with colour-coded features corresponding to specific operations. (b) Table reporting the laser parameters (power and speed) associated with each colour. The electrospun membrane location is indicated schematically.

Following laser cutting and engraving, the PMMA sheets were obtained as individual layers ready for assembly. Figure 49 shows the resulting layers after processing, highlighting the precision of the cuts and the definition of the microfluidic features, inlets/outlets, and alignment holes

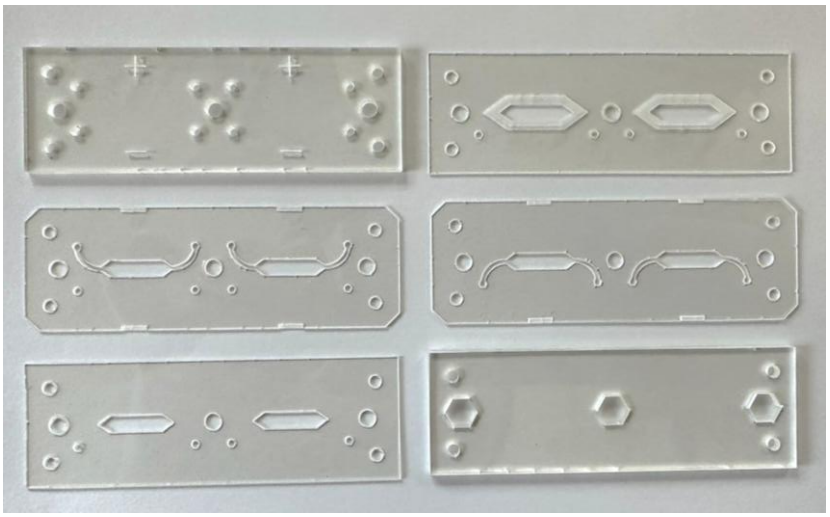

Figure 49 PMMA layers obtained after CO_2 laser cutting and engraving, showing the structural features of the device prior to assembly.

The effect of the cleaning procedure on the engraved regions of the PMMA layer is shown in the micrographs of Fig. 50 These images clearly demonstrate that CO_2 laser engraving generates a uniform layer of PMMA dust and induces surface porosity, as confirmed by the SEM images in the third column (orange arrow). Ultrasonic cleaning in water partially removes the powder, but the engraved regions still appear whitish and less transparent due to residual debris and pores. Vapor treatment with chloroform effectively eliminates the remaining PMMA powder, enhancing the transparency of the engraved areas. However, full optical clarity is not restored, as a residual surface roughness remains.

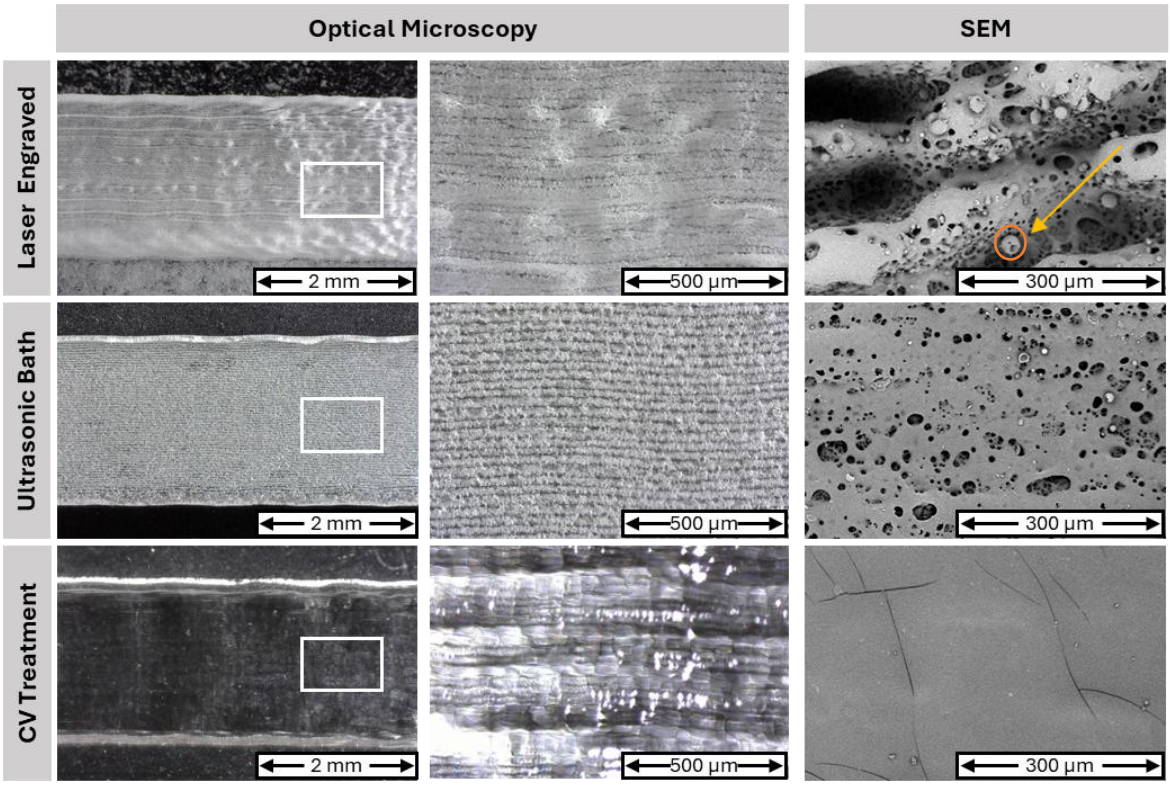

Figure 50 Effect of surface treatments on laser-ablated PMMA. The rows correspond to successive treatment steps after laser engraving: (top) immediately after cutting, the surface displays pronounced striations and pitting; (middle) after an ultrasonic-bath cleaning, debris is removed but the rough, porous texture remains; (bottom) after chloroform-vapour polishing, the surface becomes nearly featureless and transparent as solvent vapour melts and reflows the polymer. Columns show wide-field optical images (left), higher-magnification optical images (centre) and scanning electron micrographs (right); scale bars are as indicated.

This roughness is not due to the presence of PMMA powder, but rather to a micro-pattern left by the laser ablation process itself. This is clearly revealed by the SEM images in the third column, which show a flat and homogeneous surface free of particulate matter. Nonetheless, the transparency of the engraved regions is of limited importance for the

intended application, as these areas only serve to retain the electrospun scaffold within the chip and define the external boundary of the cell culture chamber.

The cleaned layers were then aligned in specific custom-made aluminium mould endowed with metallic pins corresponding to the alignment holes of the PMMA layers. The electrospun scaffold was positioned in the proper layer and then pure ethanol was spread between PMMA layers with a pipette. The bonding was carried out at 70 °C and 100 bar for 3 min in a laboratory hot press as shown in Chapter 2. Figure 51 shows a picture of the device after the assembly process.

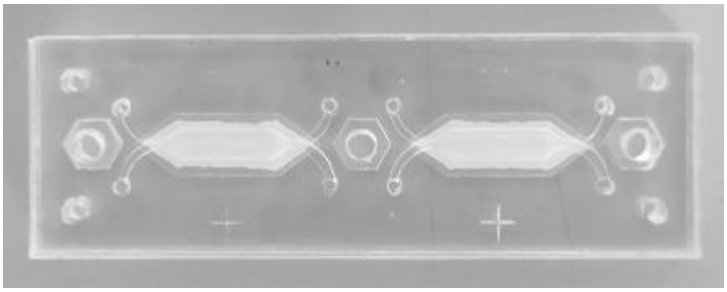

Figure 51 LoC picture after thermal bonding process.

Prior to use, the assembled device was sterilized by immersion in 70/30 ethanol/water solution for 1 hour, followed by 1 hour of UV exposure. The same sterilization procedure was applied to all accessories, including screws, tubing, and connectors, to ensure aseptic conditions.

After sterilization, cells were first seeded and allowed to adhere to the PLA scaffold during an initial static incubation of 24 h, the device was connected to the syringe pump system for dynamic perfusion experiments allowing 48 h of perfused culture. Figure 52 shows the LoC in culture, integrated with the complete microfluidic setup.

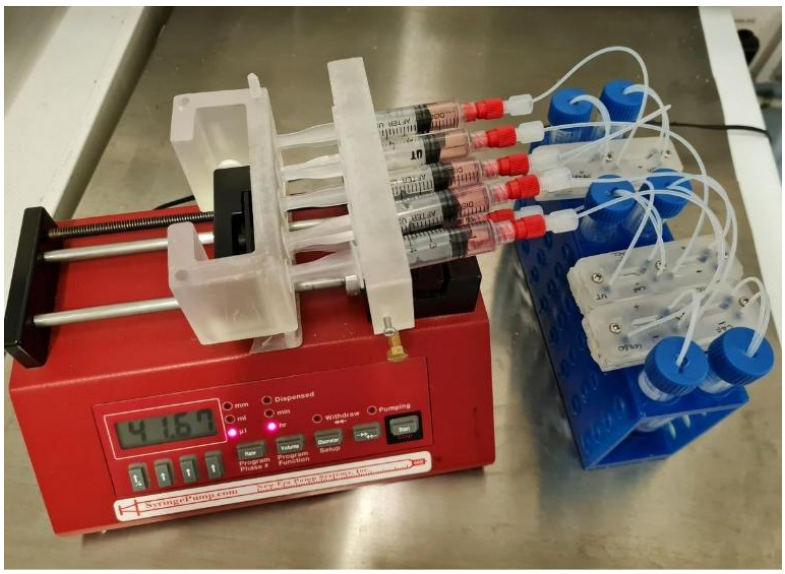

Figure 52 Experimental setup for dynamic culture. The image shows the syringe pump system connected to the assembled Liver-on-Chip devices via sterile tubing and microfluidic connectors. After sterilization (1 h in 70/30 ethanol/water and 1 h under UV light), all components—including syringes, tubing, and screws—were mounted to establish continuous perfusion of culture medium during dynamic experiments.

4.3 Flow Rate and Pressure Analysis in the LoC

CFD simulation was conducted in the fluid volume mesh (Fig. 53a) to evaluate flow velocity, shear stress and pressures at the chosen geometry and flow rate. The flow rate was set at 41.7 µL/h to ensure the renew of the medium in the upper and bottom chamber every hour.

The resulting velocity map (Fig. 53b) shows a uniform profile within the chamber, with constant velocities along its longitudinal axis. According to the no sleep condition at the walls, velocity is minimal at the walls and maximal at the inlets (2.23×10^{-5} m/s) and outlets. It remains quite homogeneous along the culture chamber with an average value of 4.46×10^{-6} m/s. The uniformity of velocity across the scaffold is advantageous, as it ensures that all cells undergo to similar stimulation.

Analysis of the shear stress values (Fig. 53c and 53d) reveals a uniform distribution on the culture surface, with consistent and homogeneous values throughout the system. Similarly to velocity, shear stress is minimal at the walls (2.8×10^{-3} dyne/cm^2) and remains relatively constant on the surface of the scaffold with and average value of 3.01×10^{-3} dyne/cm^2. This uniform distribution of shear stress is beneficial as it ensures that all cells experience similar mechanical stimuli, contributing to a more controlled and reproducible cellular environment [72].

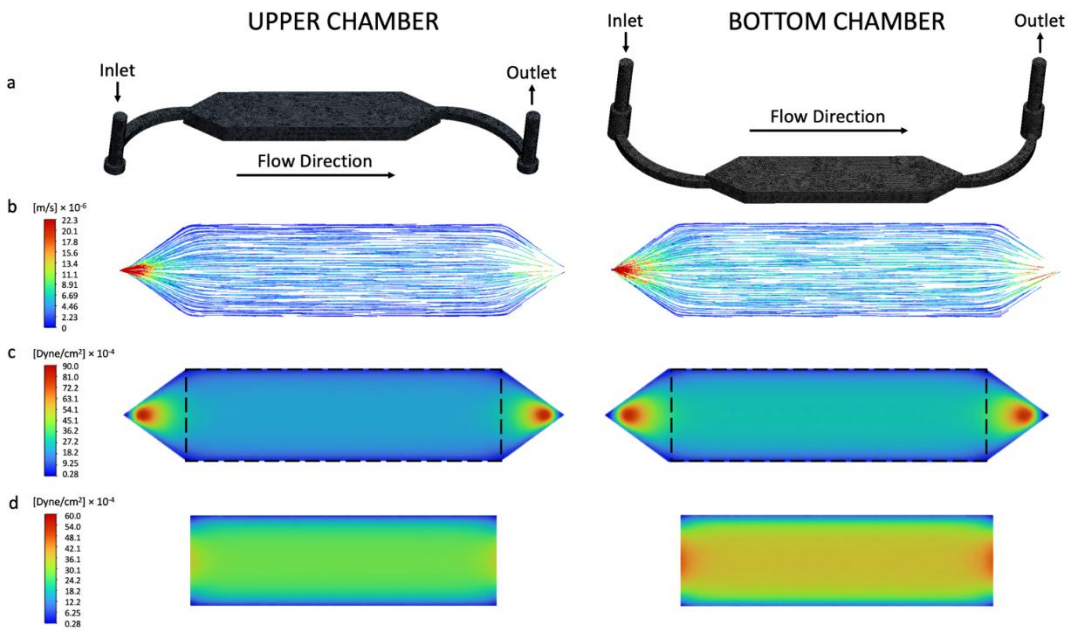

Figure 53 (a) Mesh of the fluid volumes in the LoC chambers and simulated (b) velocity magnitude; and (b),(c) shear stress along the LoC setting a flow rate of 41.7 µL/h.

Furthermore, it was observed that the top chamber exhibits lower values for shear stress compared to the bottom chamber (bottom 3.61×10^{-3} dyne/cm^2; top 3.01×10^{-3} dyne/cm^2). This result was attributed to the slightly different geometry of the two chambers. In fact, while the culture surface is the same, the height of the lower chamber is 0.85 mm while the upper chamber is 1 mm. The difference is ascribed to the presence of the electrospun scaffolds the occupy part of the volume of the bottom chamber according to the CAD design. Additionally, the average shear stress values on the scaffold were 3.2×10^{-3} dyne/cm^2.

A comparison with existing literature analysing hepatocytes indicates that our results are in the range of the commonly adopted wall shear stress (WSS) in LoC for hepatocytes dynamic cultures. In fact, in scientific literature, the wall shear stress imposed on hepatocytes when cultured in LoC platforms range in a wide interval of values from 2.9×10^{-6} dyne/cm^2 to 60 dyne/cm^2 [73].

The pressure profile within the device was experimentally evaluated by perfusing PBS at 37 °C into both the culture and perfusion chambers at a constant flow rate of 41.7 µL/h (Figure 58).

This flow rate was selected to ensure complete renewal of the medium in the culture chamber approximately once per hour, while also providing adequate oxygen supply to the cells. According to Place et al.[74], under standard incubator conditions (37 °C, 5% CO_2,

100% humidity) the dissolved oxygen concentration in cell culture medium is ~0.194 mM. Given an oxygen consumption rate for hepatocytes of 0.8 nM/10^6 cells/s [75], this flow rate is sufficient to sustain up to ~10^7 cells—well above the 5×10^4 THLE-2 cells seeded in our device—even when considering the relatively low oxygen permeability of PMMA [76].

Based on the cross-sectional areas of the two chambers (3.1 mm² for the top chamber and 2.79 mm² for the bottom), the average linear velocities of the perfused medium were calculated as 3.74×10^{-3} mm/s and 4.15×10^{-3} mm/s, respectively. These estimates are in agreement with the computational fluid dynamics (CFD) simulations previously reported by our group [77], which modelled identical device geometries and flow conditions. Wall shear stress (WSS) in the rectangular chambers was further estimated using the Navier–Stokes formulation [35]. For the top chamber, the calculated WSS was ~2×10^{-4} dyne/cm², consistent with the values obtained in our prior CFD analysis [77] and within the broad range of WSS commonly applied in dynamic liver models, from 2.9×10^{-6} to 60 dyne/cm² [78].

To measure pressure drop, four sensors were positioned at the inlets and outlets of both the upper and lower chambers (Figure 54A). Data collected over a 10-hour period (Figure 54B) revealed pressure drops of ~450 Pa across the upper chamber and ~800 Pa across the lower chamber.

The higher resistance observed in the bottom compartment is attributable to its smaller cross-sectional area and longer fluidic path, consistent with its design for extracellular vesicle (EV) perfusion. As a result, a transmembrane pressure of ~175 Pa was established, directed from the bottom toward the top chamber.

Nevertheless, this gradient is insufficient to induce significant convective transport of EVs across the electrospun scaffold. Indeed, both computational and experimental data [77] indicate that only ~0.013 μL/h (0.03% of the applied flow rate in the bottom chamber) could passively cross the scaffold.

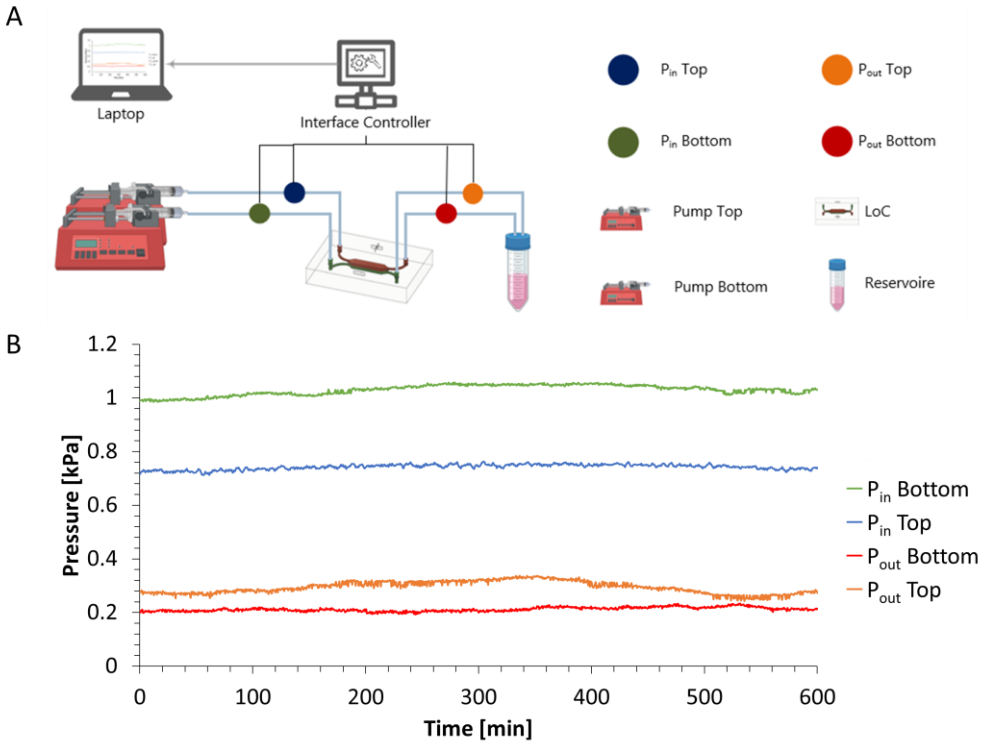

Figure 54 (a) Schematic representation of the experimental setup used to monitor inlet and outlet pressures in the upper and lower chambers of the device. PBS at 37 °C was perfused at 41.7 µL/h in both chambers using syringe pumps, while pressure sensors connected to an interface controller continuously recorded the values.
(b) Pressure profiles recorded over a 10-hour period at the four measurement points: inlet top (P_in Top, blue), inlet bottom (P_in Bottom, green), outlet top (P_out Top, orange), and outlet bottom (P_out Bottom, red). The analysis revealed a pressure drop of ~450 Pa across the upper chamber and ~800 Pa across the lower chamber, resulting in a transmembrane pressure of approximately 175 Pa directed from the bottom to the top chamber.

This supports the assumption that EV transport in our device occurs primarily by diffusion rather than convection, which closely reflects the physiological situation *in vivo*, where the endothelial barrier and basement membrane restrict bulk fluid transport.

Considering that the electrospun PLA scaffold exhibits pore sizes of ~4–5 µm and EVs have diameters of 125–150 nm [79], the slight transmembrane pressure likely enhances EVs–scaffold interactions without generating convective flux, ultimately favouring diffusion-driven delivery of EVs to the THLE-2 hepatocytes, as later confirmed by the EV uptake experiments.

4.4 Biological Assays

All biological manipulations and protocols described in this section were performed by the co-authors at the laboratories of Prof. Riccardo Alessandro and under the supervision of

Prof. Simona Fontana (Department of Biomedicine, Neurosciences and Advanced Diagnostics, University of Palermo, Italy). Their contribution is gratefully acknowledged, and all detailed information is reported in the original article Testa et al., *Lab on a Chip*, 2025, DOI: 10.1039/D5LC00353A [55].

4.4.1 Cells Culture

Before cell culturing, all Liver-on-Chip (LoC) devices, tubing, and related accessories were sterilized by immersion in a 70% (v/v) aqueous ethanol solution for 30 minutes, followed by rinsing with sterile phosphate-buffered saline (PBS) and drying under a laminar flow hood.

The THLE-2 cell line (SV40 large T antigen–immortalized human liver epithelial cells, ATCC) was cultured in RPMI 1640 medium (Euroclone, UK) supplemented with 70 ng/mL phosphoethanolamine, 5 ng/mL epidermal growth factor (EGF), 10% fetal bovine serum (FBS), and 100 U/mL penicillin–100 µg/mL streptomycin (Euroclone). Cells were maintained at 37 °C in a humidified atmosphere containing 5% CO_2.

For comparison, cells were also cultured in conventional 2D conditions using 24-well plates precoated with a collagen mixture composed of 0.03 mg/mL bovine collagen type I (Advanced Biomatrix, USA) and 0.01 mg/mL bovine serum albumin (Sigma Aldrich, USA).

On the PLA electrospun scaffolds, THLE-2 cells were seeded either under static conditions, using an insert-like device placed in 24-well plates (Static Insert-like PLA), or under dynamic conditions using the Liver-on-Chip (LoC) system.
In all configurations, the same number of cells (5×10^4 per well, corresponding to 2.5×10^4 cells/cm²) was used to ensure consistency across experiments. Although the active culture area of the LoC was 0.33 cm², the three-dimensional fibrous structure of the PLA scaffold provided an expanded surface area supporting 3D cell growth.

The SW620 colorectal cancer cell line (ATCC CCL-227) was maintained in RPMI 1640 medium supplemented with 10% FBS, 2 mM L-glutamine, 100 U/mL penicillin, and 100 µg/mL streptomycin (Euroclone). To avoid interference from bovine-derived extracellular vesicles, FBS was ultracentrifuged for 1 h 45 min at 100,000×g in a Type 70 Ti fixed-angle rotor prior to use.

Both cell lines were routinely tested for Mycoplasma contamination using Hoechst staining and the N-GARDE Mycoplasma PCR reagent set (Euroclone). Cell morphology

and proliferation rate were periodically monitored to ensure cell health and consistency throughout all experiments.

4.4.2 Lactate Dehydrogenase (LDH) Cytotoxicity Assay

The bioluminescent LDH-Glo™ Cytotoxicity Assay (Promega, USA) was performed to evaluate the biocompatibility of electrospun PLA scaffolds toward THLE-2 cells. This assay quantifies the amount of lactate dehydrogenase (LDH) released into the culture medium, which serves as a sensitive indicator of cell membrane integrity and cytotoxicity.

THLE-2 cells were cultured under three experimental conditions:

I. in conventional 2D culture,
II. on PLA scaffolds under static conditions using the insert-like system,
III. on PLA scaffolds under dynamic conditions using the Liver-on-Chip (LoC) device.

After 72 hours of culture, the conditioned medium from each experimental group was collected and diluted 1:50 in LDH Storage Buffer. Subsequently, 50 µL of each diluted sample was transferred into a 96-well plate, followed by the addition of an equal volume (50 µL) of LDH Detection Reagent. The plate was incubated for 60 minutes at room temperature, protected from light, and the resulting bioluminescent signal was recorded using a GloMax® microplate reader (Promega).

Cytotoxicity (%) was calculated following the manufacturer's instructions using the formula:

$$\text{Cytotoxicity (\%)} = 100 \times \frac{(\text{Experimental LDH Release} - \text{Medium Background})}{(\text{Maximum LDH Release Control} - \text{Medium Background})}$$

where the Maximum LDH Release Control corresponds to the amount of LDH released by cells treated with 0.2% Triton X-100 for 15 minutes.

All measurements were performed in triplicate, and data are presented as the mean ± standard deviation (SD) of at least three independent experiments.

To further assess the suitability of the PLA scaffold for hepatocyte culture, its biocompatibility with THLE-2 cells was evaluated (Figure 55). The aim of this analysis was to verify whether the scaffold provided a supportive and non-cytotoxic environment for cell growth, particularly when compared with conventional 2D cultures. LDH quantification was selected as it represents a robust and quantitative indicator of cell death, reflecting the release of this cytosolic enzyme upon plasma membrane damage or rupture. The assay was performed after 72 hours of culture under the three previously described conditions: standard 2D monolayers, PLA-based static insert-like systems (as described in Chapter 2), and the dynamic Liver-on-Chip platform.

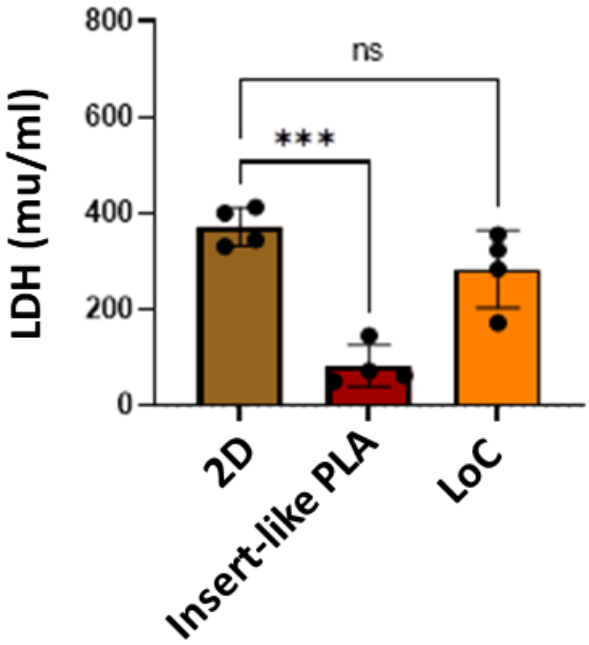

*Figure 55 Lactate dehydrogenase (LDH) release assay performed on THLE-2 hepatocytes after 72 h of culture in different conditions: conventional 2D, static culture on custom insert-like PLA scaffolds, and dynamic culture in the Liver-on-Chip (LoC) platform. Results show significantly higher cytotoxicity in the insert-like PLA condition compared to both 2D and LoC cultures, whereas no significant differences were observed between 2D and LoC. Data are presented as mean ± SD (n=3); statistical significance was evaluated by one-way ANOVA (**p < 0.001, ns = not significant).*

A significant reduction in LDH release was observed for cells grown on PLA supports compared to 2D cultures, confirming the favourable environment provided by the scaffold for hepatocyte maintenance.

4.4.3 Shear Stress Tolerance4 and Cell Adhesion

In line with the previous findings, THLE-2 hepatocytes demonstrated firm adhesion to the PLA scaffold after 24 hours of culture. To evaluate their resistance to shear stress under dynamic conditions, a perfusion test was performed by flowing phosphate-buffered saline (PBS) through the Liver-on-Chip (LoC) device at a rate of 2000 µL/min for 5 minutes.

THLE-2 cells were seeded in the upper chamber of the LoC device and allowed to adhere for 24 hours. The following day, the culture medium was removed, and PBS was perfused through the lower chamber using a syringe pump. The outgoing PBS was collected and analyzed by cell counting using a Bürker chamber, both before and after centrifugation, to assess potential cell detachment during perfusion.

Meanwhile, cells remaining in the device were fixed with 4% paraformaldehyde (PFA), rinsed three times with PBS, and stained with Actin Green and Hoechst 33342 (Molecular Probes, Life Technologies, Carlsbad, CA, USA). Samples were subsequently examined under fluorescence microscopy (Nikon Eclipse Ti).

No evidence of cell detachment was observed, as confirmed by the absence of cell pellets in the collected PBS and by manual counting. This flow rate corresponded to average fluid velocities of 1.08 mm/s in the upper chamber and 1.19 mm/s in the lower chamber, resulting in wall shear stress (WSS) values of 5.74×10^{-1} dyne/cm² and 7.09×10^{-1} dyne/cm², respectively.

Importantly, these shear stress levels did not compromise cell adhesion, as demonstrated by the actin mean fluorescence intensity (MFI), which remained comparable between static and perfused conditions (Figure 56). These results confirm that the PLA scaffold provided a mechanically stable and biologically supportive microenvironment, capable of maintaining hepatocyte attachment even under high-flow dynamic conditions.

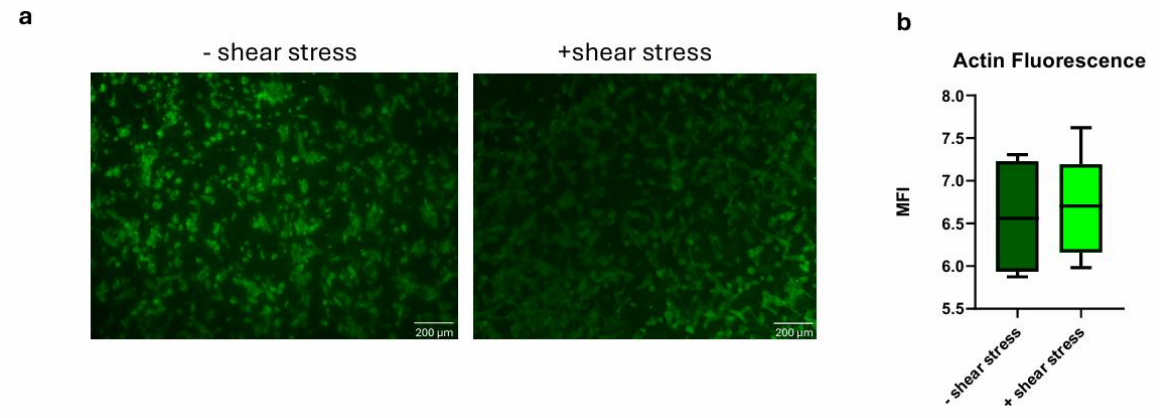

Figure 56 Evaluation of THLE-2 hepatocyte adhesion under shear stress. (a) Representative actin fluorescence micrographs of cells cultured on PLA scaffolds under static conditions (– shear stress) and after perfusion with PBS at 2000 µL/min for 5 minutes (+ shear stress). Scale bar: 200 µm. (b) Quantification of actin mean fluorescence intensity (MFI) showing no significant differences between static and perfused conditions, confirming that shear stress did not compromise cell adhesion.

4.4.4 Morphology evaluation

As described in the previous chapters, electrospun scaffolds were also analysed by scanning electron microscopy (SEM) after cell culture, in order to verify the preservation of scaffold morphology during dynamic perfusion and to assess cell distribution and morphology on the electrospun (ES) substrate. After retrieval from the devices, scaffolds underwent fixation and dehydration following literature protocol [80] described in Chapter 2, to enable SEM imaging of the cellularized membranes.

Figure 57 shows representative SEM images of THLE-2 cells cultured under static conditions for 72 h into the Inset-like device. In this case, the cells exhibited limited proliferation, with large areas of exposed electrospun membrane and only partial colonisation of the fibres.

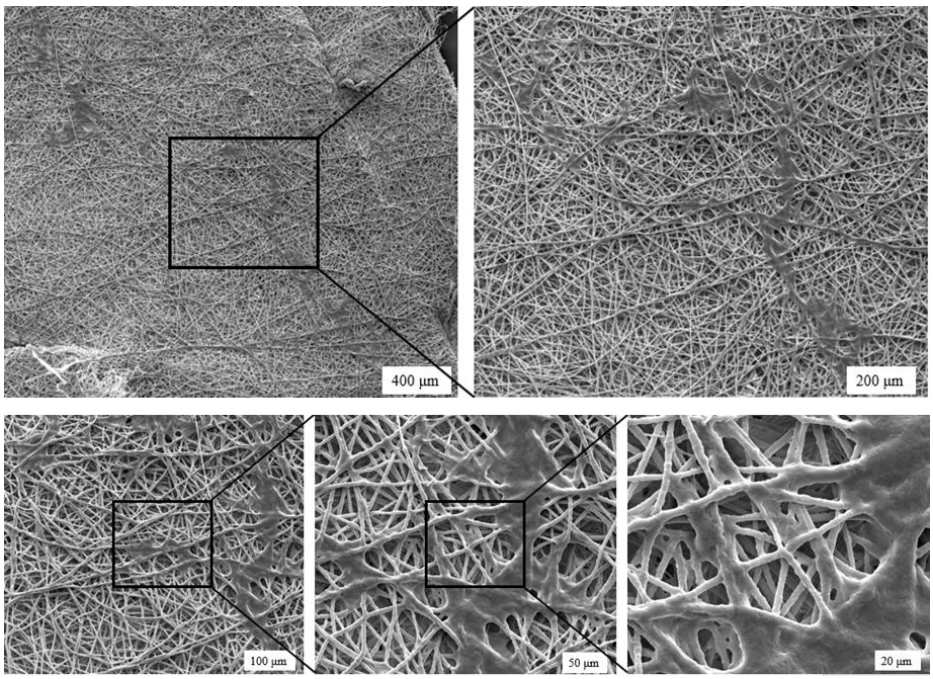

Figure 57 THLE-2 cells cultured under static conditions for 72 h into the Inset-like device at different magnifications.

In contrast, Figure 58 reports SEM images of THLE-2 cells cultured dynamically within the LoC device for a total of 48 h. Cells were first seeded and allowed to adhere to the PLA scaffold during an initial static incubation of 24 h, followed by 24 h of perfused culture. The images highlight improved cell adhesion and spreading compared to static conditions, with cells beginning to cover the underlying fibre network.

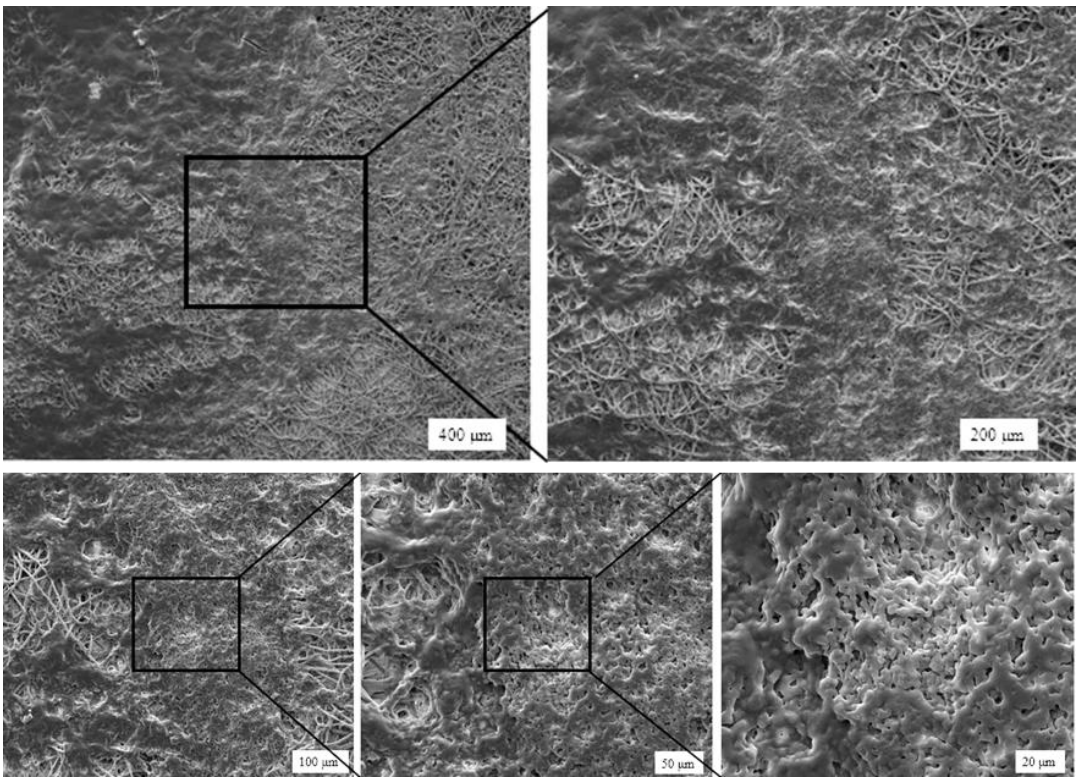

Figure 58 THLE-2 cells cultured dynamically within the LoC device for a total of 48 h at different magnifications.

Finally, Figure 59 illustrates SEM images of THLE-2 cells after 72 h of dynamic culture within the LoC. Here, cells were also allowed to adhere under static conditions for the first 24 h, followed by 48 h of perfusion. Compared to 48 h, the scaffold surface at 72 h appeared almost entirely covered by cells, which densely colonized and masked the electrospun fibres.

Taken together, these observations confirm the fluorescence microscopy results. In particular, the extended perfusion period (72 h) led to a more homogeneous and confluent coverage of the scaffold, demonstrating the suitability of the dynamic OoC culture system for supporting hepatocyte growth.

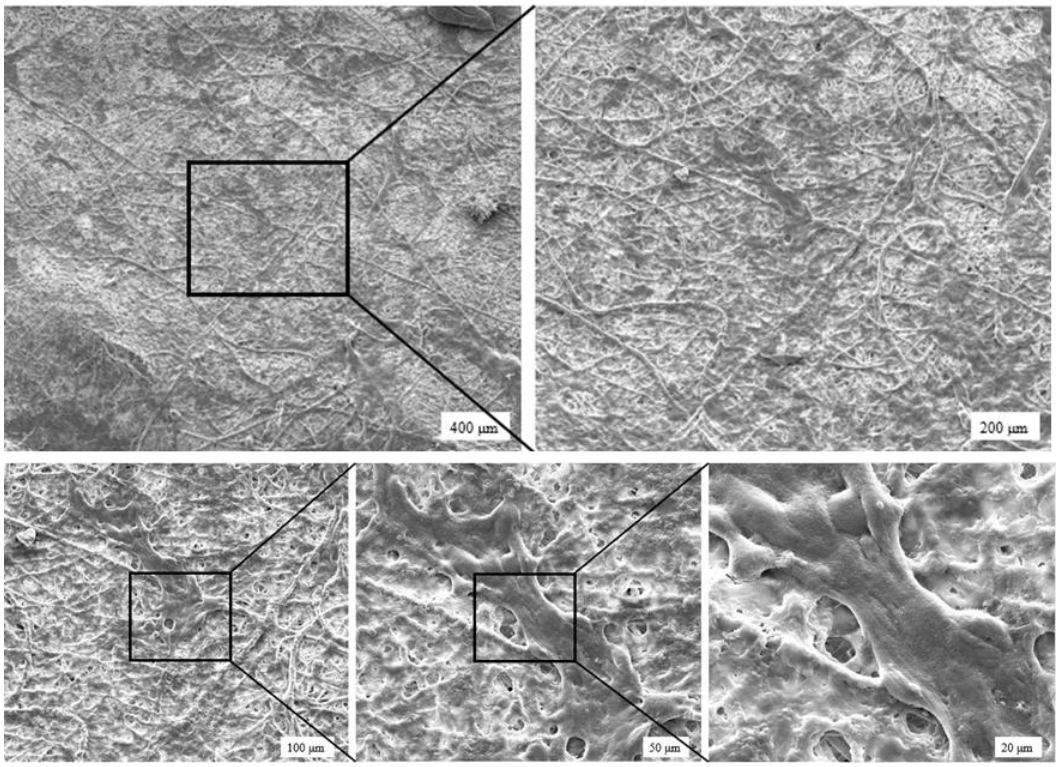

Figure 59 THLE-2 cells after 72 h of dynamic culture within the LoC at different magnifications.

4.5 Proof of concept validation

To experimentally validate the diffusion of extracellular vesicles (EVs) across the electrospun PLA membrane within the Liver-on-Chip (LoC) device, an EV uptake assay was performed. SW620-derived EVs, previously characterized by Fontana *et al.* [81], were fluorescently labelled using the PKH26 Red Fluorescent Cell Linker Kit (Merck KGaA, Darmstadt, Germany). The EVs were incubated with the dye for 20 minutes, washed three times with PBS, and then centrifuged to remove unbound dye. The resulting EV pellet was resuspended in RPMI medium for subsequent use.

Labelled SW620-EVs were introduced into the lower chamber of the LoC device, while THLE-2 hepatocytes were cultured in the upper chamber on the electrospun PLA membrane. Following 4 hours of perfusion, the medium was removed, and the cells were fixed with 4% paraformaldehyde (PFA), washed three times with PBS, and permeabilized with 0.1% Triton

X-100. Subsequently, cells were stained with Actin Green and Hoechst 33342 (Molecular Probes, Life Technologies, Carlsbad, CA, USA).

For improved visualization of the EV distribution, the LoC device was carefully disassembled and the PLA membrane was extracted and mounted between two coverslips. Samples were analyzed under fluorescence microscopy (Nikon Eclipse Ti).

After 4 hours of perfusion, PKH26-labelled EVs were clearly detectable in the upper chamber, where they colocalized with THLE-2 hepatocytes, although their spatial distribution was not yet homogeneous (Figure 60). These results confirm that SW620-derived EVs successfully diffused across the PLA scaffold and reached the hepatic cells, consistent with previous findings and supporting the biological effects described in the following sections.

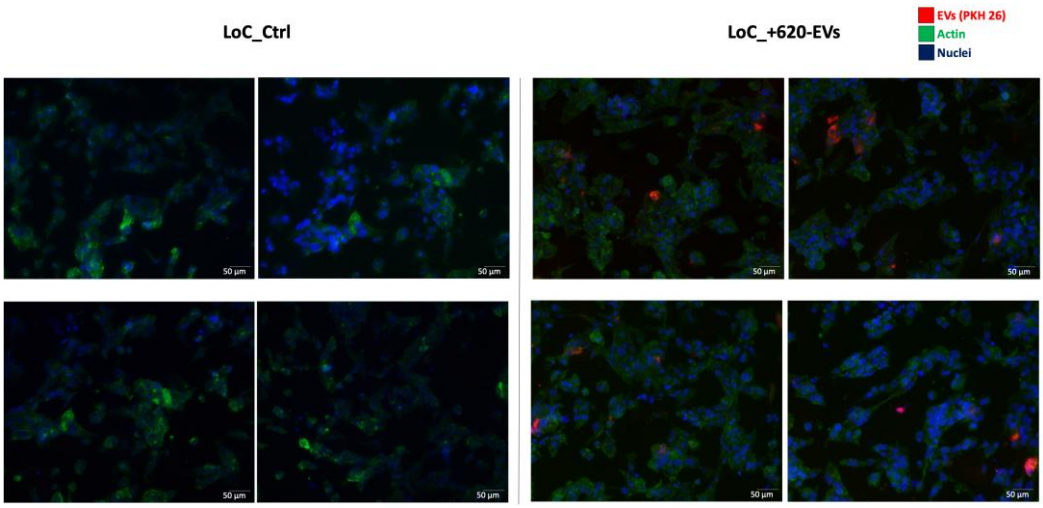

Figure 60 Diffusion assay of PKH 26/SW620-EVs by THLE-2 cells. (scale bar = 50 µM). LoC_Ctrl: untreated cells. For each condition four different fields are shown.

To further assess the potential of this system, we compared the LoC with results obtained in our previous 2D study [81], where acute exposure of THLE-2 cells to 20 µg/mL SW620-EVs for 48 h induced epithelial-to-mesenchymal transition (ETM). This was evidenced by the up-regulation of mesenchymal markers (Vimentin, α-SMA) and the concomitant down-regulation of epithelial markers (E-Cadherin, CK8/18). Remarkably, similar results were obtained in the LoC under conditions of chronic delivery, where the same cumulative EV dose (20 µg/mL) was administered over 48 h at a constant perfusion rate of 41.7 µL/h (corresponding to ~0.83 µg/h of SW620-EVs) (Figure 61a). Quantitative analysis of mean fluorescence intensity (MFI) confirmed the up-regulation of Vimentin under both acute (2D) and chronic (LoC) treatment conditions (Figure 61b).

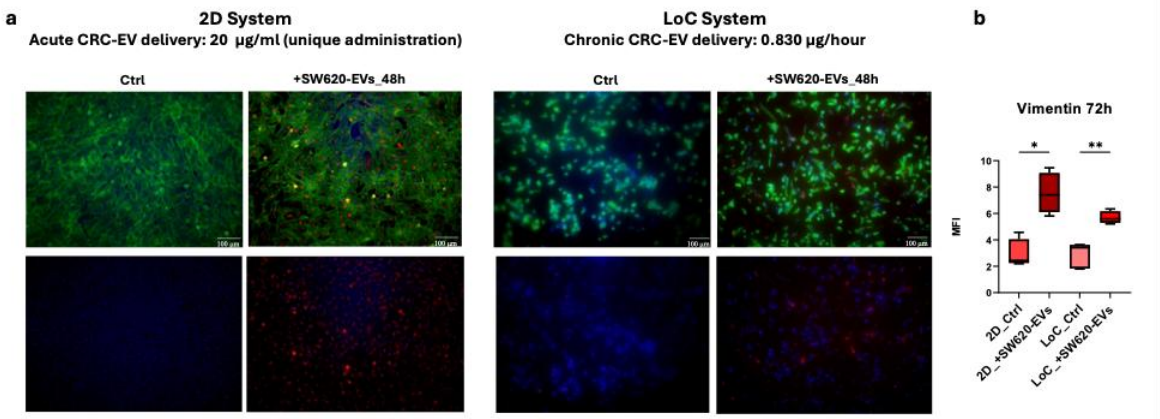

*Figure 61 Expression of vimentin in hepatic cells exposed to colorectal cancer-derived extracellular vesicles (CRC-EVs) under acute (2D) and chronic (LoC) exposure conditions.(a) Representative immunofluorescence images showing vimentin (green) and nuclei (blue, DAPI) in 2D cultures (acute delivery: 20 µg/mL, 48 h) and in the Liver-on-Chip (LoC) system (chronic delivery: 0.830 µg/h, 48 h). EV-treated cells (+SW620-EVs) exhibited enhanced vimentin expression compared to controls (Ctrl), consistent with epithelial-to-mesenchymal transition (EMT)-like activation. Scale bars: 100 µm. (b) Quantification of mean fluorescence intensity (MFI) of vimentin after 72 h confirming significant upregulation upon CRC-EV treatment in both systems (*p < 0.05; **p < 0.01).*

Taken together, these findings demonstrate that the developed LoC is an effective platform for the chronic, low-dose delivery of EVs to target cells. By more closely mimicking the continuous exposure that occurs *in vivo*, this approach overcomes the limitations of conventional 2D cultures based on acute, high-dose stimulation, providing a physiologically relevant system for studying EV-mediated cellular responses.

4.6 Discussion and Perspectives

The multicompartment Liver-on-Chip developed in this work embodies a significant advance over traditional 2D cultures and static 3D systems. By coupling thermoplastic microfabrication with an electrospun PLA scaffold and controlled perfusion, the platform recapitulates key aspects of hepatic physiology—namely, three-dimensional architecture, ECM-mediated cell adhesion, and low-shear sinusoidal flow. These features enable long-term culture of hepatocytes, promoting differentiation and metabolic functionality, as evidenced by the up-regulation of liver-specific proteins in proteomic analyses. Dynamic perfusion also facilitates continuous delivery of tumour-derived extracellular vesicles (EVs), providing a more physiologically relevant exposure scenario than bolus dosing. Under these conditions, hepatocytes internalise CRC-EVs and exhibit mesenchymal marker induction, recapitulating early events in pre-metastatic niche formation.

Compared with PDMS-based chips, the use of PMMA mitigates problems of small-molecule adsorption and permits rapid, reproducible prototyping via laser

micromachining. Integration of an electrospun scaffold confers an ECM-like microenvironment absent in membrane-based microfluidic devices and supports perfused co-culture configurations.

Furthermore, proteomic analyses, previously reported by Testa et al.[55], , demonstrated that hepatocytes cultured on R-PLA scaffolds undergo enhanced differentiation and activation of liver-specific pathways under both static and perfused conditions. Moreover, chronic administration of tumour-derived vesicles was shown to induce a mesenchymal shift, evidenced by vimentin upregulation. Although these proteomic results are described in detail elsewhere, they support the findings presented in this work by confirming that the developed platform provides a robust tool to study tumour–liver communication and pre-metastatic niche formation. Taken together, these advances highlight the capacity of the system to overcome the limitations of conventional 2D and static models, pushing Organ-on-Chip technology forward in cancer research and therapeutic development.

Nevertheless, several limitations merit consideration. First, the study relied on an immortalised hepatocyte line (THLE-2), which lacks the full metabolic capacity of primary human hepatocytes; future work should incorporate primary cells or induced pluripotent stem cell–derived hepatocytes to enhance physiological relevance. Second, non-parenchymal liver cells (e.g. Kupffer, stellate and endothelial cells) and immune components were absent from the model, yet these populations contribute to tumour cell homing and EV uptake. Incorporating multiple cell types in the multicompartment design would yield a more comprehensive representation of the hepatic microenvironment. Third, while the current design supports chronic EV administration, additional studies are needed to determine whether the EMT-like response is reversible and whether it translates to functional changes in drug metabolism or matrix remodelling.

Looking ahead, the modular nature of the LoC lends itself to several extensions. Coupling liver chips with other organ chips could enable pharmacokinetic modelling and multi-organ communication studies, aligning with efforts to develop “body-on-a-chip” systems. Incorporating continuous, real-time sensors (e.g. oxygen, glucose, lactate) would provide dynamic readouts of cell health and metabolic status. Microfluidic integration with mass spectrometry could enable on-line analysis of secreted molecules and EV cargo. Finally, adopting emerging standardization frameworks (ISO 23494 series, CEN-CENELEC Focus Group recommendations) and open-platform approaches like the Translational Organ-on-Chip Platform will facilitate reproducibility, interoperability and regulatory acceptance. By addressing these challenges, the Liver-on-Chip platform described here may

evolve into a robust tool for studying pre-metastatic niche formation, evaluating hepatotoxicity and guiding the development of personalised cancer therapies.

5 Tumor on Chip

In light of the emerging breakthroughs in cancer biology, drug discovery, and personalized medicine, Tumor-on-Chip (ToC) platforms have become pivotal tools in current biomedical research. This application introduces a novel rapid prototyping approach for the fabrication of a ToC device using laser-patterned poly(methyl methacrylate) (PMMA) layers integrated with a polylactic acid (PLA) electrospun scaffold, enabling dynamic drug delivery and the assessment of therapeutic efficacy in cancer cells [54].

To assess the biological relevance of the developed ToC platform, preliminary experiments were conducted to verify whether the R-PLA scaffolds could support the adhesion, growth, and interactions of breast cancer (BC) cells (HCC-1937) and with stromal components of the tumor microenvironment (TME). This step was essential to validate the device not only as a robust microfluidic prototype, but also as a functional model for reproducing physiologically relevant tumour–stroma interactions.

Biological validation was designed to confirm the ability of the PLA scaffold to sustain the adhesion and proliferation of BC cells alone or in co-culture with Cancer Associated Fibrobasts, CAFs, both under static conditions performed on R-PLA and within the dynamic environment of the ToC device.

Fluorescence microscopy and SEM were employed to monitor cell adhesion, distribution, and morphology on the electrospun matrices, while drug-response assays were performed to evaluate whether the system could recapitulate therapeutic effects observed *in vivo* [82]. In particular, the combined treatment with olaparib (PARP inhibitor) and dinaciclib (CDK inhibitor) was used as proof of concept, given its previously demonstrated efficacy in impairing the growth of aggressive BC cells [83].

Through these experiments, the biological validation provided key insights into the capability of the ToC platform to reproduce essential features of the TME and to serve as a preclinical tool for anticancer drug testing.

5.1 Rationale of the device

To develop a robust *in vitro* model capable of recapitulating the interactions between cancer cells and their surrounding microenvironment, weas designed a Tumor-on-Chip

(ToC) system that integrates two distinct but interacting cellular compartments. The platform is composed of a top culture chamber, dedicated to the seeding of breast cancer (BC) cells (HCC-1937), and a bottom chamber housing cancer-associated fibroblasts (CAFs), separated by a thin (~50 µm) R-PLA scaffold mimicking the tumour microenvironment (TME) (Figure 69). This configuration was adapted and further optimized from the Liver-on-Chip design described in the previous chapter with modifications aimed at utilizing commercial microfluidics connectors.

The rationale for this architecture stems from the critical role of the TME in tumor progression and therapeutic resistance. Previous studies have demonstrated that TME-associated stromal populations—particularly CAFs and adipose-derived mesenchymal stem cells (ASCs)—not only promote cancer cell proliferation and invasion but also provide protective signals that attenuate the efficacy of anticancer treatments [81]. By incorporating a scaffold-like membrane, the ToC enables physiologically relevant cell–cell and cell–matrix interactions while maintaining fluidic communication between the compartments, thus allowing paracrine and autocrine signalling to occur in a controlled manner. The modular design of the ToC further permits flexible experimental setups in a double chamber device. Panels I–IV in Figure 62, highlight the versatility of the platform showing the timing of the engineered experimental configurations.

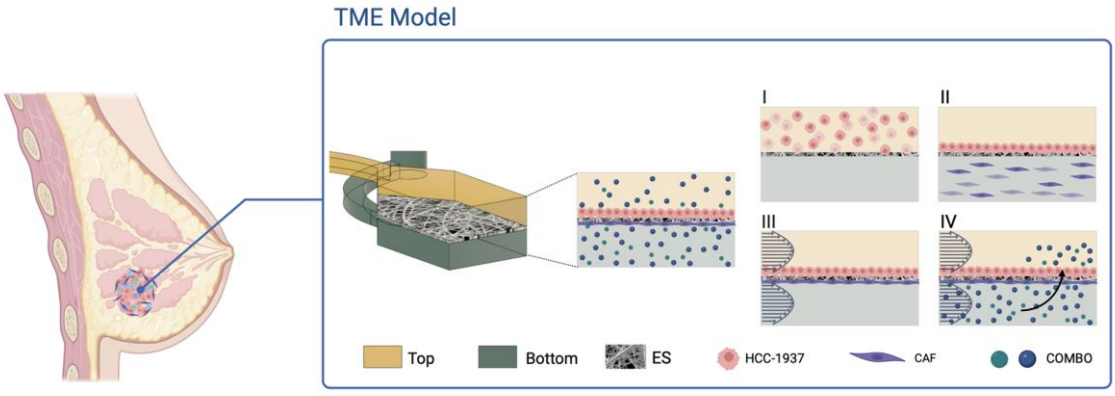

Figure 62 Schematically illustration of the modular design of the Tumor-on-Chip (ToC) platform and its potential applications. The device is composed of two culture chambers separated by an electrospun PLA scaffold (ES) that mimics the basement membrane. Breast cancer (HCC-1937) cells are seeded in the upper chamber, while cancer-associated fibroblasts (CAFs) are cultured in the lower chamber. This configuration enables controlled cell–cell and cell–matrix interactions within a perfused microenvironment that reproduces essential features of the tumour microenvironment (TME).

Panel I shows a monoculture of breast cancer cells seeded on the upper side of the scaffold, used to evaluate cell adhesion and proliferation in static conditions. Monocultures of HCC was performed in static for 12 hour inside the device in order to permit cells attachment.

Panel II illustrates the introduction of CAFs in the bottom chamber, enabling co-culture across the scaffold to study tumour–stroma crosstalk.

Panel III represents dynamic perfusion of culture medium through the system, mimicking nutrient delivery under flow.

Finally, **Panel IV** depicts dynamic combined treatments or multi-stimuli experiments, designed to replicate the complexity of the TME and to investigate drug responses in physiologically relevant conditions.

Through this design, the ToC provides a scalable, reproducible, and biologically relevant platform for studying tumour–stroma interactions, evaluating drug efficacy, and dissecting mechanisms of therapeutic resistance in breast cancer.

From an engineering perspective, the ToC device largely derives from the Liver-on-Chip platform described in the previous chapter. However, several modifications were introduced to adapt the design to the specific requirements of tumour microenvironment modelling. In particular, screw-based connectors and gaskets were eliminated in favour of standardized integrated microfluidic connectors, which ensure more reliable fluid handling, enhanced modularity, and compatibility with a wide range of existing microfluidic accessories (Figure 63). These improvements also facilitated sterilization procedures by reducing the number of individual components, while at the same time simplifying assembly. As a result, device setup can be performed more rapidly and with minimal handling, without requiring engineering expertise, thereby improving usability for biological operators and ensuring higher sterility standards.

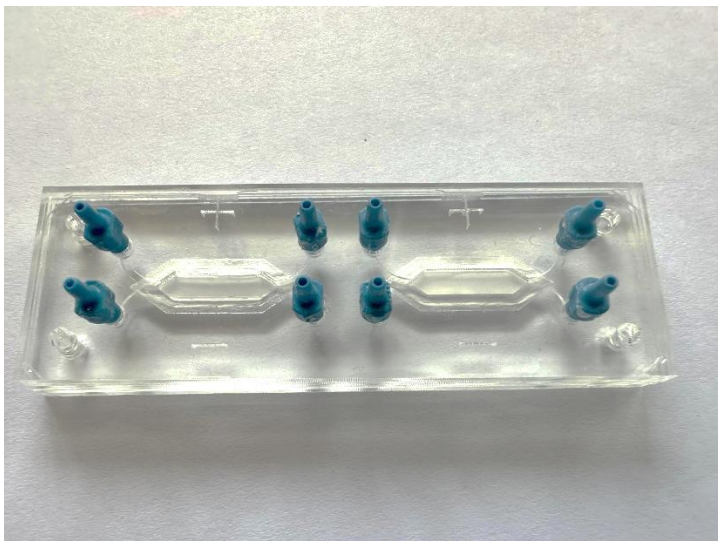

Figure 63 Assembled Toc Device whit commercial microfluidic connectors (ChipShop).

Building on these technical advancements, the following section focuses on the biological validation of the ToC, assessing its capacity to support breast cancer cell culture reproducing key features of the tumour microenvironment and the dynamic administrion of anticancer drugs.

5.2 Biological Validation

All biological manipulations and experimental protocols described in this section were performed by the co-authors at the laboratories of Prof. Giorgio Stassi and Prof. Matilde Todaro (University of Palermo, Italy). Their contribution is gratefully acknowledged. For detailed procedures, please refer to the original publication:

Testa, M.; Gaggianesi, M.; D'Accardo, C.; Porcelli, G.; Turdo, A.; Di Marco, C.; Patella, B.; Di Franco, S.; Modica, C.; Di Bella, S.; et al. *A Novel Tumor-on-Chip Mimicking the Breast Cancer Microenvironment for Dynamic Drug Screening* [60].

5.2.1 Cell culture

Human breast cancer cell lines with distinct phenotypes were employed: MCF-7 (luminal A, estrogen receptor-positive) and MDA-MB-231 (triple-negative, mesenchymal-like) (ATCC, USA). Cells were maintained in DMEM (Euroclone, Italy) supplemented with 10%

fetal bovine serum (FBS), 2 mM L-glutamine, and antibiotics (100 U/mL penicillin and 100 µg/mL streptomycin). For vascular co-culture, human umbilical vein endothelial cells (HUVECs, Lonza, Switzerland) were expanded in endothelial growth medium (EGM-2, Lonza) containing growth supplements. All cell lines were cultured at 37 °C in a humidified atmosphere of 5% CO_2, regularly monitored for morphology and proliferation, and screened for Mycoplasma contamination using Hoechst staining and PCR-based assays.

5.2.1 Seeding on PLA scaffolds and Tumor-on-Chip

Cells were seeded under three different conditions: (i) on standard tissue culture plates (2D static), (ii) on electrospun PLA membranes used in insert-like systems (Static PLA), and (iii) within the dynamic Tumor-on-Chip (ToC) platform, where PLA membranes were integrated as porous scaffolds separating upper and lower channels. A seeding density of ~25,000 cells/cm² was applied to ensure comparability across systems.

In the ToC, MCF-7 or MDA-MB-231 cells were seeded on the upper chamber, while HUVECs were cultured on the opposite side of the scaffold, allowing tumor–endothelium cross-talk under dynamic perfusion. Following seeding, cells were allowed to attach for 24 h before initiating perfusion at controlled flow rates using syringe pumps. This setup enabled long-term maintenance of co-cultures under conditions that better mimic the *in vivo* tumor microenvironment.

5.2.2 Proof of Concept Validation

Cytotoxicity was assessed through LDH release assays (Promega), while proliferation was quantified via Quant-iT™ PicoGreen dsDNA assays (Thermo Fisher Scientific). For cytoskeletal organization and adhesion, samples were fixed and stained with ActinGreen™ (Thermo Fisher) and Hoechst (Molecular Probes).

Immunofluorescence was performed with antibodies specific for tumor epithelial markers (cytokeratin, Santa Cruz Biotechnology) and endothelial markers (CD31, Cell Signaling Technology). Secondary antibodies conjugated to DyLight 488 or DyLight 594 (Thermo Fisher Scientific) were employed, and samples were imaged using a Nikon Eclipse Ti fluorescence microscope. Mean fluorescence intensity (MFI) was quantified across multiple regions of interest using ImageJ software.

Drug testing under dynamic perfusion

To evaluate therapeutic responses, the Tumor-on-Chip platform was challenged with two targeted agents:

I. **Olaparib**, a PARP inhibitor clinically used in BRCA1/2-mutated breast cancers, administered at pharmacologically relevant concentrations.

II. **Cinaciclib** (Palbociclib-like CDK4/6 inhibitor), targeting tumor cell proliferation by blocking cell cycle progression.

Drugs were perfused into the lower channel of the ToC system under two regimens: (i) a single bolus (acute treatment) or (ii) continuous delivery (chronic exposure) over 48 h. This design allowed simulation of short-term versus long-term drug exposure in a perfused tumor microenvironment.

Cellular responses were assessed by combining biochemical assays (LDH release for cytotoxicity, PicoGreen for proliferation) with morphological and immunofluorescence analyses. Particular attention was given to changes in tumor–endothelial interactions, epithelial-to-mesenchymal transition (TME) features, and drug-induced cytoskeletal remodeling.

A fundamental prerequisite for the validation of the Tumor-on-Chip (ToC) platform was to verify whether the R-PLA scaffold could provide a biocompatible substrate for cell adhesion and proliferation. The biological validation of the ToC platform was carried out to confirm whether R-PLA scaffolds, once integrated into the device, could sustain the adhesion, growth, and interaction of breast cancer (BC) cells with stromal components of the tumor microenvironment (TME).

Previous studies have demonstrated that stromal populations, particularly cancer-associated fibroblasts (CAFs) and adipose-derived mesenchymal stem cells (ASCs), play a crucial role in promoting tumorigenicity and conferring resistance to anticancer drug treatments [84] [81] [85].

Fluorescence and electron microscopy performed on the Insert-like devices revealed that both BC cells (HCC1937) and CAFs were able to adhere to the PLA scaffold and were uniformly distributed across its surface. The cells also partially infiltrated the fibrous network, although without achieving complete penetration of the scaffold (Figure 64A,B).

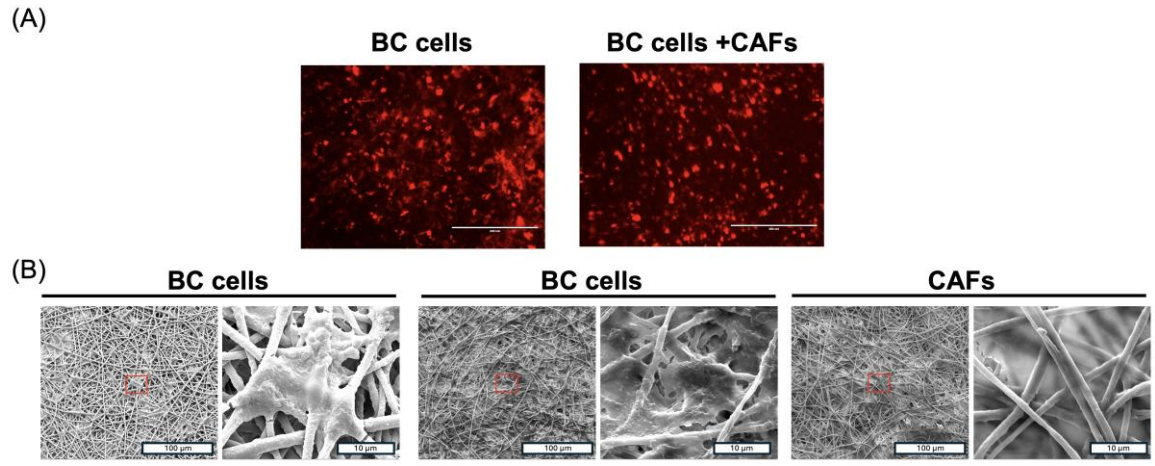

Figure 64 ***Biological validation of the Tumor-on-Chip (ToC) platform using R-PLA scaffolds:*** *(A) Fluorescence microscopy images showing breast cancer (BC, HCC1937) cells cultured alone or in co-culture with cancer-associated fibroblasts (CAFs). (B) Representative SEM micrographs of BC cells, BC cells in co-culture with CAFs, and CAFs alone seeded on R-PLA scaffolds.*

To further evaluate the translational potential of the developed system as a preclinical platform, a pharmacological treatment previously validated *in vivo* was tested both in the static insert-like system and within the dynamic ToC. Breast cancer (BC) cells, plated alone or in co-culture with CAFs, were treated for 48 h with either vehicle (untreated condition) or with the drug combination olaparib (10 μM) and dinaciclib (5 nM). Representative fluorescence images are shown in Figure 69.

In static culture (Figure 65A), both BC cells alone and BC cells co-cultured with CAFs displayed reduced viability following treatment with the drug combination compared to vehicle controls. However, in the co-culture condition, a higher number of viable BC cells persisted, suggesting that CAFs exert a protective effect on tumor cells, in line with their recognized role in modulating therapy resistance within the tumour microenvironment (TME) [84] [81] [85].

When the same experimental setup was replicated under dynamic perfusion in the ToC platform (Figure 65B), untreated controls displayed an overall higher cell viability compared to static conditions, reflecting the beneficial impact of continuous medium renewal on cell proliferation and survival. Importantly, the protective effect of CAFs against drug-induced cytotoxicity was even more evident in dynamic conditions. While BC cells cultured alone showed a marked decrease in viability upon treatment, BC cells co-cultured with CAFs maintained a higher survival fraction, confirming that stromal support attenuates drug efficacy.

In xenograft models of breast cancer, the combination of the PARP inhibitor **olaparib** with the CDK inhibitor **dinaciclib** had been shown to impair the growth of aggressive cancer cells characterized by high expression of a key mediator of resistance to PARP inhibitors in triple-negative breast cancer (TNBC) [86].

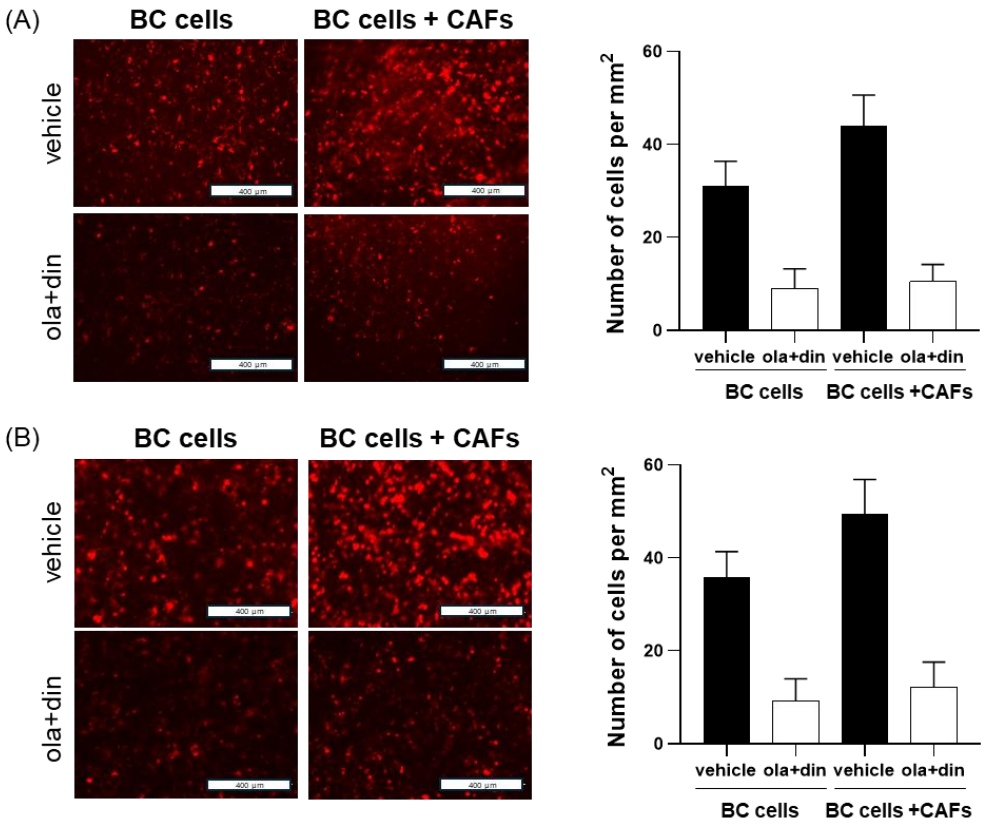

Figure 65 ***Pharmacological validation of the Tumor-on-Chip (ToC) platform with olaparib and dinaciclib treatment.*** *(A) Representative fluorescence images of breast cancer (BC, HCC1937) cells cultured alone or in co-culture with cancer-associated fibroblasts (CAFs) under static insert-like conditions..(B) Fluorescence images of the same experimental conditions reproduced under dynamic perfusion in the ToC platform.*

Scanning electron microscopy further revealed alterations in cell integrity in both cell populations exposed to the drug combination, along with the deposition of olaparib crystals on the scaffold surface (Figure 66A,B) [87].

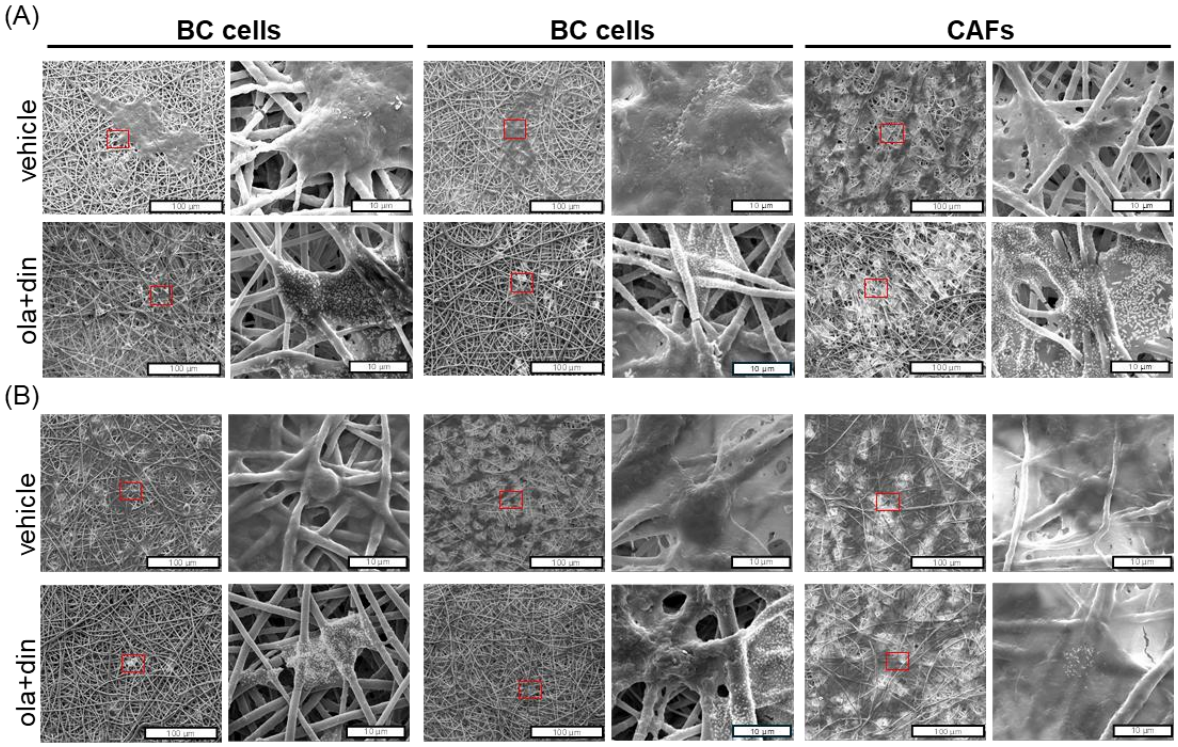

Figure 66 Scanning electron microscopy (SEM) images of breast cancer (BC) cells and cancer-associated fibroblasts (CAFs) cultured on plasma-treated PLA electrospun scaffolds after 48 h of treatment with vehicle or the drug combination olaparib (10 µM) and dinaciclib (5 nM). Scale bars: 100 µm and 10 µm.

Another relevant observation is that dynamic perfusion within the ToC allowed cells to maintain morphology and proliferative activity over the culture period. This finding highlights the contribution of the microfluidic environment in supporting more physiologically relevant conditions compared to conventional static systems.

Overall, these results demonstrate that the ToC platform developed in PMMA with electrospun PLA scaffolds successfully replicates crucial tumor–stroma interactions and preserves drug response patterns consistent with those observed *in vivo*. The system thus represents a reliable and versatile tool for preclinical cancer research, with potential applications in drug screening and personalized medicine approaches

5.3 Discussion and Perspectives

In this work, we developed an innovative Tumor-on-Chip (ToC) platform fabricated in PMMA and integrating electrospun PLA scaffolds to mimic the tumour microenvironment (TME). The fabrication strategy preserved the intrinsic morphological properties of the electrospun scaffold while enhancing its degree of crystallinity, thereby ensuring structural robustness and biological compatibility during perfusion. This technical optimization was essential to generate a reproducible and scalable platform that bridges the gap between conventional 2D monolayers and more complex 3D tumour models.

Biological validation demonstrated that the ToC supported robust proliferation of breast cancer (BC) cells, preserved their morphology, and allowed the establishment of co-cultures with stromal components such as CAFs. Importantly, the system reproduced key tumour–stroma interactions that are known to shape cancer cell behaviour and therapeutic response. For instance, drug testing with the olaparib–dinaciclib combination recapitulated the protective effect of CAFs previously reported *in vivo*, with reduced drug sensitivity observed in co-cultures compared to monocultures. This outcome underscores the ability of the ToC to capture essential aspects of the TME, providing results consistent with xenograft models while avoiding the limitations of animal experimentation.

Compared to static cultures, dynamic perfusion within the ToC resulted in improved cell viability in untreated conditions and enhanced reproducibility of drug exposure, highlighting the importance of fluid flow for maintaining a physiologically relevant microenvironment. These results position the ToC as a robust platform for studying both cancer progression and drug response under conditions that more closely approximate *in vivo* physiology.

Although 3D models such as spheroids and organoids have advanced the field by enabling the study of tumour architecture and heterogeneity, their limited standardization, technical complexity, and lack of controlled perfusion restrict their translational applicability. Similarly, while animal models capture multicellular interactions, they often fail to predict drug toxicity and efficacy in human patients, particularly when immunocompromised hosts are used. In this context, the ToC described here represents a valuable alternative, combining dynamic culture conditions, scaffold-mediated cell–matrix interactions, and modularity with high reproducibility.

Overall, the integration of electrospun scaffolds within PMMA-based microfluidic devices provides a versatile and biologically relevant approach to preclinical modelling. This

ToC platform not only reduces reliance on animal testing but also offers a physiologically meaningful environment for the evaluation of novel anticancer compounds. Future work will focus on extending this model to include immune components of the TME, further enhancing its predictive capacity for immunotherapy and combination treatment strategies.

6 Brain on Chip

One of the major challenges in pharmacology remains the limited selectivity of therapeutic compounds toward specific tissues and cell types. In most cases, drugs distribute systemically before reaching the intended site of action, potentially reducing their efficacy and inducing adverse off-target effects. This limitation is particularly critical in the central nervous system (CNS), which is characterized by a highly complex architecture and a wide diversity of specialized cell populations that work in close interaction to maintain brain function and homeostasis. Many neurological disorders selectively affect specific neuronal or glial subpopulations or discrete brain regions, further underlining the need for experimental models capable of reflecting this cellular heterogeneity.

Conventional two-dimensional cultures, although widely employed, are inadequate for mimicking the three-dimensional organization and dynamic microenvironment of neural tissue. To address this limitation, a novel Brain-on-Chip (BoC) microfluidic platform was developed, integrating an electrospun scaffold engineered to reproduce extracellular matrix-like properties. The device is designed to support the co-culture of two distinct CNS cell types within spatially separated yet fluidically connected compartments, thus allowing paracrine interactions and exposure to shared perfused media. This configuration provides a more physiologically relevant setting for evaluating selective drug–cell interactions under dynamic flow conditions.

As a proof-of-concept application, the BoC was tested using myelin-derived nanovesicles (MyVes), previously developed and characterized by Picone *et al.* at the Institute for Biomedical Research and Innovation (IRIB), CNR, Palermo, Italy, who also collaborated in the experimental phase of this study. MyVes have been shown to exhibit selective tropism for microglial cells, making them an ideal model system for assessing the platform's ability to discriminate drug–cell interactions.

Overall, the BoC platform represents an integrated and modular tool for advancing *in vitro* modelling of the CNS. By enabling controlled and reproducible studies of compound selectivity across different neural cell types, it holds promise for improving the predictive power of preclinical screening strategies and contributing to the development of more effective and safer therapies targeting neurological diseases

6.1 The rationale

The Brain-on-Chip (BoC) platform was specifically designed to investigate the selectivity of pharmacological compounds across distinct neural cell populations cultured within a shared perfused environment. This configuration enables a direct comparison of drug responses between two different cell types, which are initially seeded in separate compartments and subsequently exposed to the same culture medium under controlled flow conditions that reproduce physiologically relevant fluid velocities. The design of the BoC, in the same way of both the LoC and ToC devices, include two separate culture chambers integrated within the same platform, allowing each platform to serve as a duplicate for every experimental condition.

As illustrated in Figure 67A (top view) and Figure 67B (perspective view), the device consists of a single chamber with an overall height of 4 mm. A central septum, 2 mm in height, divides the chamber into two symmetrical compartments. Since the septum does not extend across the full chamber height, perfusion induces medium overflow, thereby establishing controlled fluidic communication between the two initially segregated compartments. This design ensures that, once flow is applied, both cell populations are exposed to the same biochemical environment, allowing selective drug–cell interactions to be assessed under dynamic conditions.

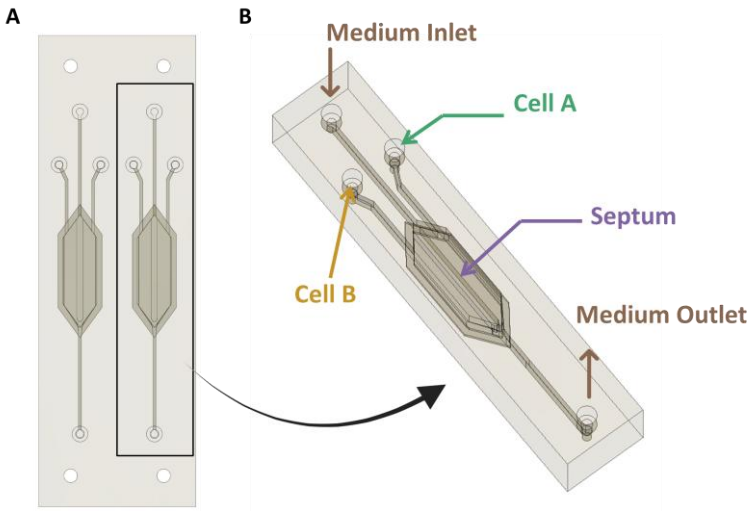

Figure 67 A) Top-View design of the whole BoC system composed of two culture chambers: B) Perspective-View of a single culture chamber design highlighting the inlets for cells and medium and the medium outlet.

A thin electrospun PLA scaffold was positioned at the base of the chamber to provide a biomimetic substrate for cell attachment and growth. Two scaffold configurations—randomly oriented fibres and aligned fibres—were employed in order to investigate the influence of substrate topography on cellular behaviour, including adhesion, morphology, and survival.

The device incorporates three inlets and one outlet. The lateral inlets are dedicated to the independent seeding of two distinct cell populations, enabling their initial physical separation. The central inlet allows the infusion of either plain culture medium or drug-containing solutions, ensuring uniform perfusion throughout the chamber. The outlet, positioned at the chamber base, facilitates continuous medium exchange while preventing drug accumulation and guaranteeing reproducible exposure profiles.

The exploded view shown in Figure 68 highlights the four functional PMMA layers (L1–L4) that compose the BoC. Each layer was obtained from pre-formed sheets using CO_2 laser cutting and engraving, with a specific role assigned to each component:

- **Layer 1 (L1, 3 mm):** accommodates inlet and outlet ports, with circular openings designed to fit connectors or sealing plugs.
- **Layer 2 (L2, 2 mm):** distributes the medium evenly within the central chamber through dedicated microchannels.
- **Layer 3 (L3, 2 mm):** includes the microchannels for independent seeding, the central septum dividing the chamber, and the outlet channel for recirculation.
- **Layer 4 (L4, 1 mm):** acts as the chamber base, supporting the integration of the electrospun scaffold and ensuring fluidic sealing of the assembly.

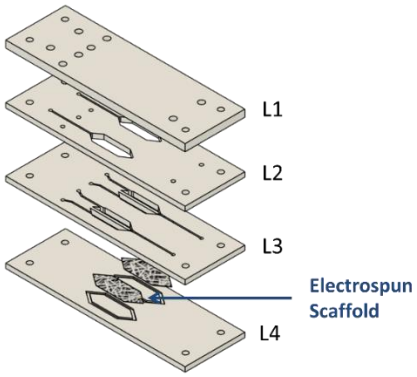

Figure 68 CAD design of the exploded view of the BoC into its four functional layers and the scaffold.

Figure 69 reports the technical drawings of the individual chip layers, including the main dimensions, hole diameters and positioning of the channels. Each layer (L1-L4) highlight the precise measurements of the inlets/outlets, alignment holes, and chamber geometries. These schematics provides a clear overview of the laser-cutting design used during fabrication.

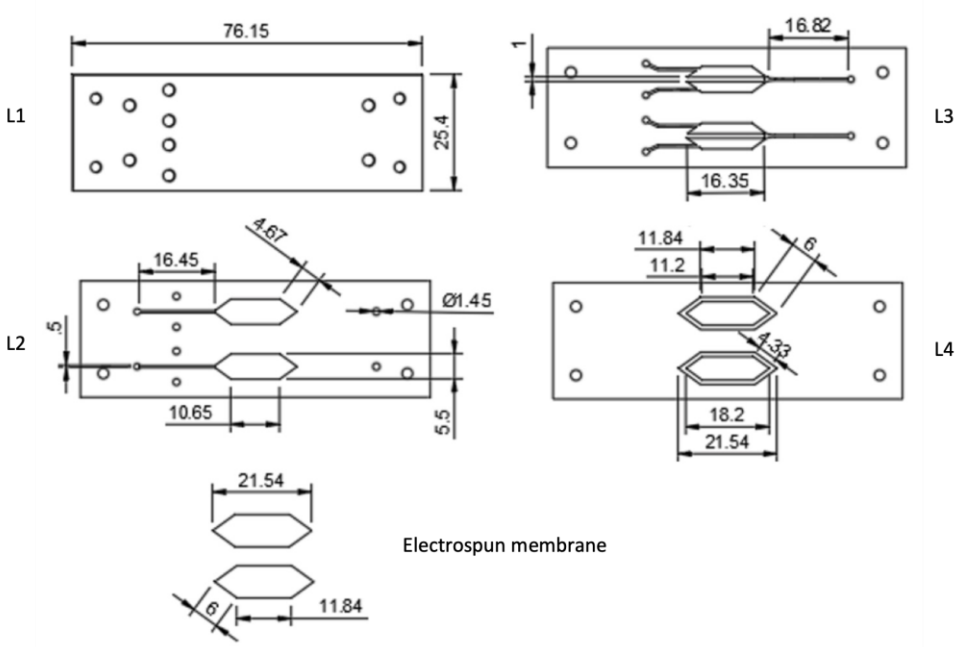

Figure 69 Technical drawings of the Brain-on-Chip (BoC) device separated into its functional layers. Dimensions of inlets, outlets, channels, and electrospun membrane housing are expressed in millimeters (mm). The scheme highlights the precise alignment of microchannels and the membrane interface, ensuring proper fluidic separation and controlled communication between compartments.

As shown in Figure 70A, the four functional layers (L1–L4) were fabricated through laser cutting and engraving. In layer L3, the central septum separating the two culture chambers was preserved without deformation during micromachining, demonstrating the high precision of the process. Optimization studies identified 2 mm as the minimum thickness required to guarantee structural stability without warping. Layer L4 was instead engraved with recesses specifically designed to accommodate and secure the electrospun scaffold.

As shown in Figure 70B, the untreated engraved regions exhibited a whitish, opaque appearance due to the recondensation of vaporized polymer. Ethanol cleaning reduced surface particle deposition (Figure 70C), although residual pores remained visible under SEM. After TCM vapor treatment, transparency was markedly enhanced (Figure 70D), and SEM analysis confirmed both the removal of particulate residues and the significant

reduction of laser-induced porosity. The resulting surfaces appeared smooth and homogeneous, with only occasional microcracks, thereby ensuring reliable functionality of the assembled device.

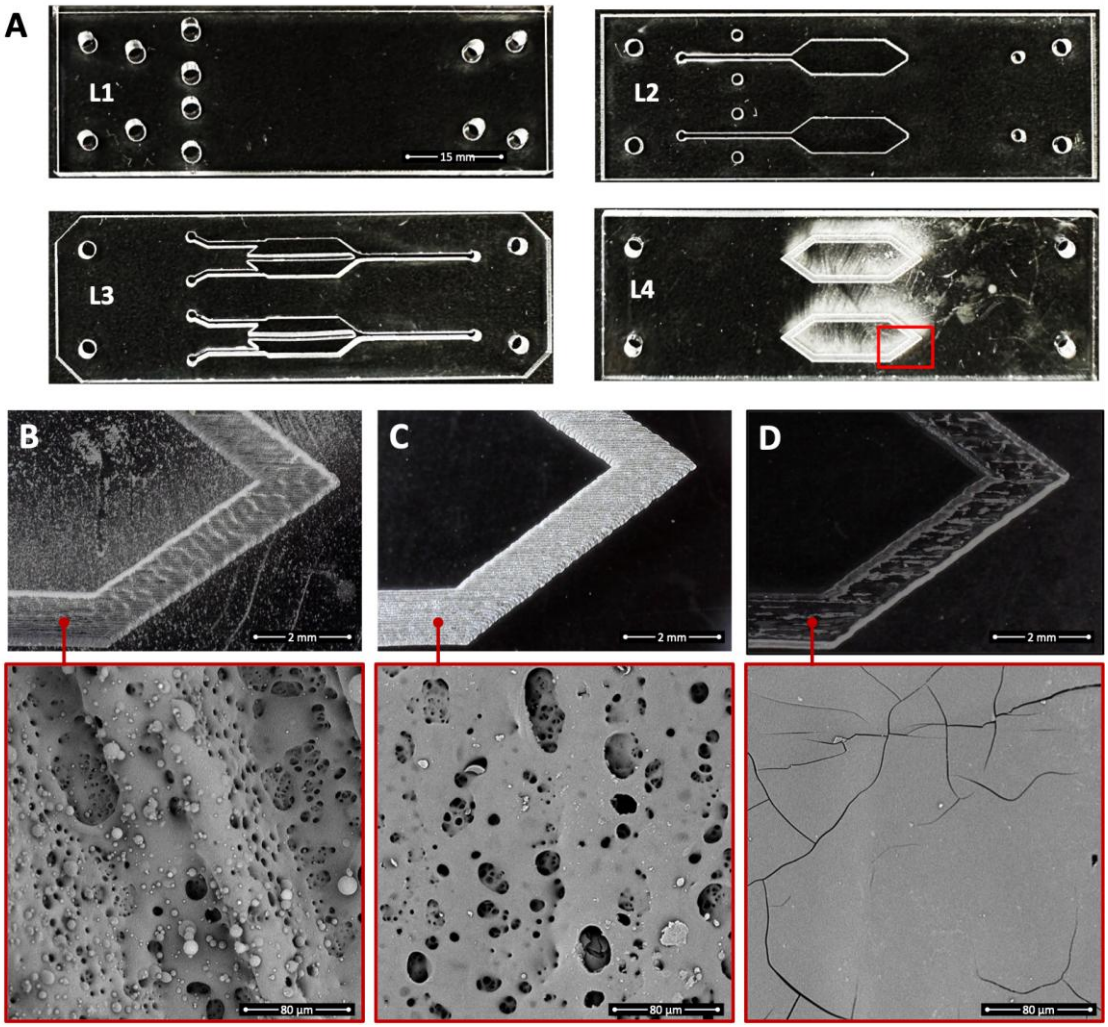

Figure 70 Fabrication and post-processing of the PMMA-based BoC layers. (A) Laser-cut and engraved PMMA layers (L1–L4), showing high-fidelity reproduction of the microfluidic layout, including the structurally intact 2 mm-wide septum in layer L3 and the engraved regions in L4 designed for scaffold anchoring. (B) Optical image of the engraved area in L4 prior to cleaning, exhibiting a whitish and opaque appearance due to laser-induced debris and surface porosity. (C) Surface morphology after ultrasonic cleaning in ethanol is macroscopically unchanged, whereas SEM analysis reveals a reduction in particulates, but persistent microporosity. (D) Post-treatment with TMC vapor results in restored optical clarity and a smooth, homogeneous surface, as confirmed by SEM, with minimal residual artifacts and occasional microcracks.

After assembly, the device exhibited a robust overall architecture with precisely aligned layers, a result ensured by the use of corner alignment holes and mold-integrated alignment pins (Figure 71A). The effectiveness of the compartmentalized culture chamber was then verified through a seeding simulation: two aqueous solutions, each containing a different food dye, were introduced separately into the two compartments (80 µL each), mimicking

the loading of distinct cell suspensions (Figure 71B). A magnified view of the terminal region (Figure 75C) confirmed that the injected solutions fully covered the culture surfaces without cross-contamination between chambers. Notably, fluid compartmentalization was preserved for at least 48 h—twice the time required for stable cell adhesion to the scaffold—and no appreciable differences were detected between devices containing R-PLA or A-PLA scaffolds.

Achieving this reliable separation required fine optimization of the chamber geometry, particularly the thickness of layers L2 and L3. A critical challenge was to prevent the seeded droplet from contacting the upper chamber wall due to surface tension, which could compromise compartment isolation. By carefully adjusting the vertical spacing, stable fluid confinement and strict independence of the two seeding regions were ensured.

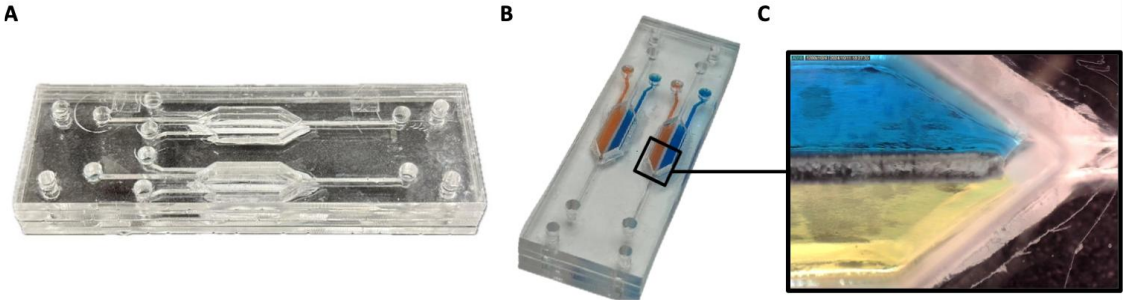

Figure 71 ***Validation of the assembly and compartmentalization performance of the Brain-on-Chip device****. (A) Assembled chip showing precise alignment of the PMMA layers, ensured by integrated alignment pins and corner holes. (B) Simulation of the dual-cell seeding process using food dyes: 80 µL of two differently colored aqueous solutions were injected into the separate compartments of the culture chamber. (C) Magnified view of the terminal region of the culture chamber, demonstrating complete surface coverage and effective fluid compartmentalization without cross-contamination. Dye separation was maintained for 48 hours. No differences in compartmentalization performance were observed between devices with randomly oriented (R-PLA) or aligned (A-PLA) scaffolds.*

As schematically illustrated in Figure 72, the morphology of electrospun scaffolds integrated within the devices was examined in two distinct regions: directly beneath the septum separating the two compartments and, at higher magnification, in an area located ~500 µm away from the dividing wall. As anticipated, the scaffold immediately below the septum exhibited marked structural disruption, with a clear loss of porosity. This confirms the mechanical role of the septum in ensuring compartmental isolation, as the compacted region prevents fluid crossover that would otherwise occur through capillary-driven flow.

Conversely, the scaffold regions adjacent to the septum retained a well-preserved fibrous architecture, demonstrating that the fabrication process enables scaffold integration without substantially compromising microstructural integrity. Minor alterations were nonetheless observed: fibers appeared locally fused, likely due to localized thermal or mechanical

stresses during the bonding step. Importantly, this effect did not significantly impact the average fiber diameter. In aligned scaffolds, fibers also displayed a slightly more undulated morphology compared to their pre-assembly state. It remains unclear whether this waviness originated from the fabrication process itself or from the disassembly procedure required for SEM preparation.

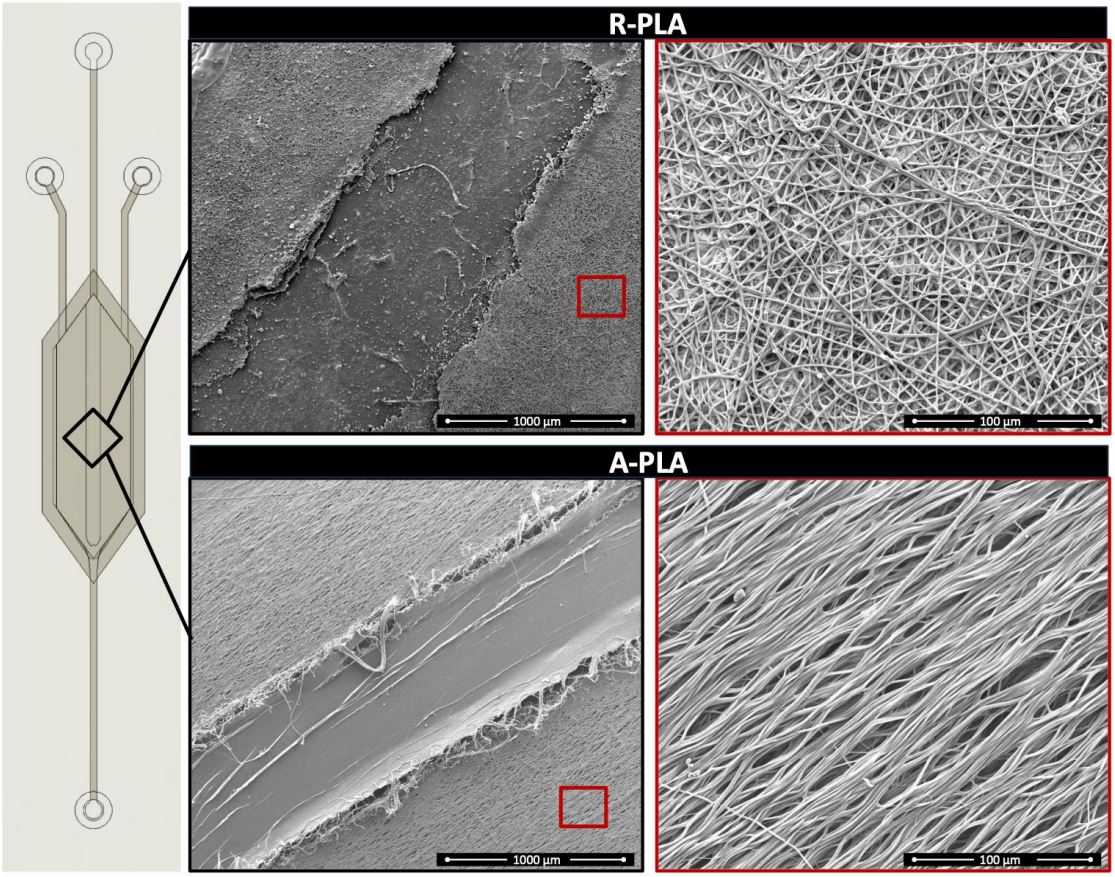

Figure 72 SEM analysis of scaffold morphology near the septum within the assembled BoC device. The left image schematically illustrates the regions of interest: beneath the septum and approximately 500 µm away from it.

At this stage of the work, the experimental workflow designed to validate the Brain-on-Chip (BoC) was established (Figure 73). The concept behind the device is to host two distinct cell populations within the same platform, enabling parallel assessment of their responses to selective stimuli. To this end, BV2 and SH-SY5Y cells were seeded in two separate compartments of the culture chamber. After seeding, the lateral inlets used for loading were sealed with plugs, while microfluidic connectors were inserted into the central inlet and outlet to allow controlled medium perfusion.

The BoC was then maintained under static conditions for 24 hours to promote cell adhesion onto the electrospun PLA scaffold, which was fabricated using either randomly oriented (R-PLA) or aligned (A-PLA) fibers. Subsequently, medium containing the test compound was perfused for 2 hours, establishing dynamic and differential stimulation of the two cell populations. The effect of the treatment was finally assessed using a fluorescent marker, applied either as a direct label or as an uptake reporter. Thanks to the optical transparency and low autofluorescence of PMMA, fluorescence signals could be reliably detected by microscopy or scanning platforms. In this setting, a selective drug is expected to elicit a fluorescent signal only in the responsive population, leaving the non-targeted region unstained.

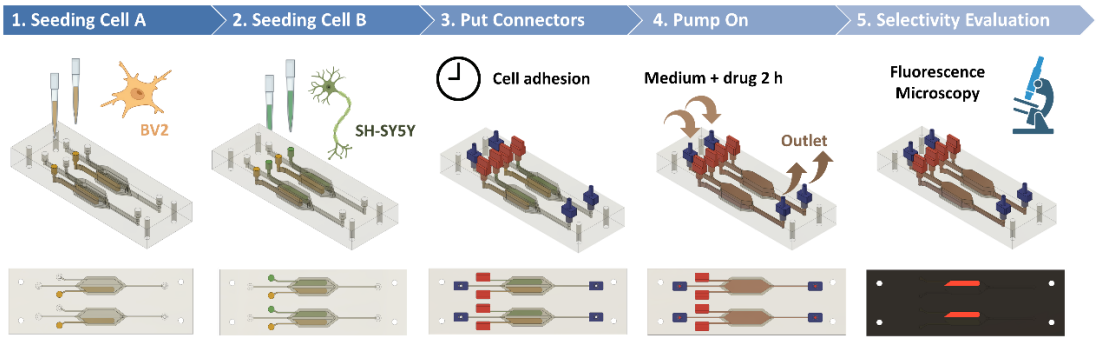

Figure 73 Schematic representation of the BoC working principle used as a proof of concept in this study. (1–2) BV2 and SH-SY5Y are selectively seeded in two distinct regions of the culture chamber. (3) After seeding, lateral inlets (red) are sealed, and the device undergoes 24 hours of static incubation to allow cell adhesion onto the electrospun PLA scaffold, composed of either randomly oriented (R-PLA) or aligned (A-PLA) fibers. (4) The device is first perfused for 2 hours with drug-containing medium to assess cell-specific responses. (5) Fluorescence microscopy is used to evaluate drug selectivity through a fluorescent marker, which reveals uptake only in the compartment containing sensitive cells. The high optical transparency and low autofluorescence of the PMMA-based device enable efficient imaging.

To determine the most suitable perfusion parameters for the BoC system, a computational fluid dynamics (CFD) analysis was conducted on the fluid domain. The primary objective was to identify flow rates that would generate velocities at the cell culture surface comparable to those reported in brain tissue, typically ranging between 0.1 and 1.0 µm/s in healthy conditions [88]. Several trial CFD simulations were performed, and the optimal flow rate was identified as 1.39 mL/h.

Although this value is higher than the estimated physiological volumetric flow in the brain of healthy, awake adults (0.4–1 µL/min [89]), it proved sufficient to maintain adequate oxygen supply for both cell types cultured within the device. Under standard culture conditions (100% humidity, 5% CO_2, 37 °C), the dissolved oxygen concentration in culture

medium is approximately 0.194 mM, which corresponds to an oxygen delivery of ~4.6 nmol/min at the selected flow rate [74]. Considering oxygen consumption rates of 3.33 nM/10^6 cells/min for BV2 microglial cells [90] and 2.5 nM/10^6 cells/min for SH-SY5Y neuroblastoma cells [91], and taking into account the seeding densities used in this study (6×10^{-4} BV2 and 12×10^{-4} SH-SY5Y cells per compartment), the total estimated oxygen demand amounted to ~0.55 nmol/min. This represents only ~12% of the oxygen delivered through perfusion, confirming the adequacy of the selected conditions. It is also relevant to note that during the static adhesion phase (Step 3), the chamber was only partially filled, with culture medium occupying the bottom half and air filling the upper half. This configuration allowed passive gas exchange through open inlet and outlet ports, further supporting oxygen availability. Conversely, under dynamic perfusion (Step 4), the chamber was completely filled with medium. Given the low oxygen permeability of PMMA [92], this closed configuration highlights the importance of optimized perfusion to ensure adequate oxygenation.

CFD simulations additionally provided insight into the mechanical environment of the cell culture. As shown in Figure 74A, the pressure drop across the device at 1.39 mL/h was approximately 0.8 Pa, well below thresholds known to compromise cell viability. The shear stress distribution (Figure 74B) was mapped across the culture chamber.

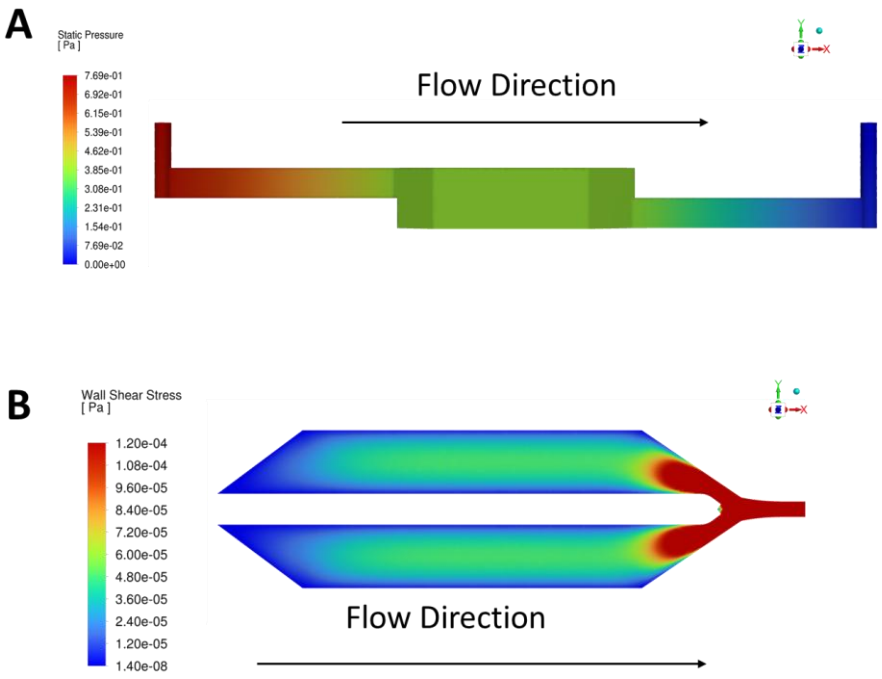

Figure 74 Computational fluid dynamics (CFD) simulation results for the BoC device. (A) Simulated pressure drops across the device under a flow rate of 1.39 mL/h. (B) Wall shear stress distribution at the culture surface.

Values ranged between 1.46×10^{-4} and 5.12×10^{-4} dyne/cm², approximately two orders of magnitude lower than typical physiological levels (~0.01 dyne/cm² [88]). Such low shear stresses are unlikely to critically affect mechanotransduction pathways, while remaining sufficient to maintain stable perfusion without inducing cell detachment.

Flow streamlines (Figure 75) revealed a diagonal trajectory from inlet to outlet, with higher velocities in the channels and reduced velocities within the culture chamber due to its larger cross-sectional area. This configuration minimized the risk of drug accumulation or stagnant regions. A detailed analysis of the velocity field at 30 µm above the chamber base—corresponding to the cell culture surface—confirmed a uniform distribution of velocities, ranging from 0.29 to 1.45 µm/s, consistent with physiological values [88].

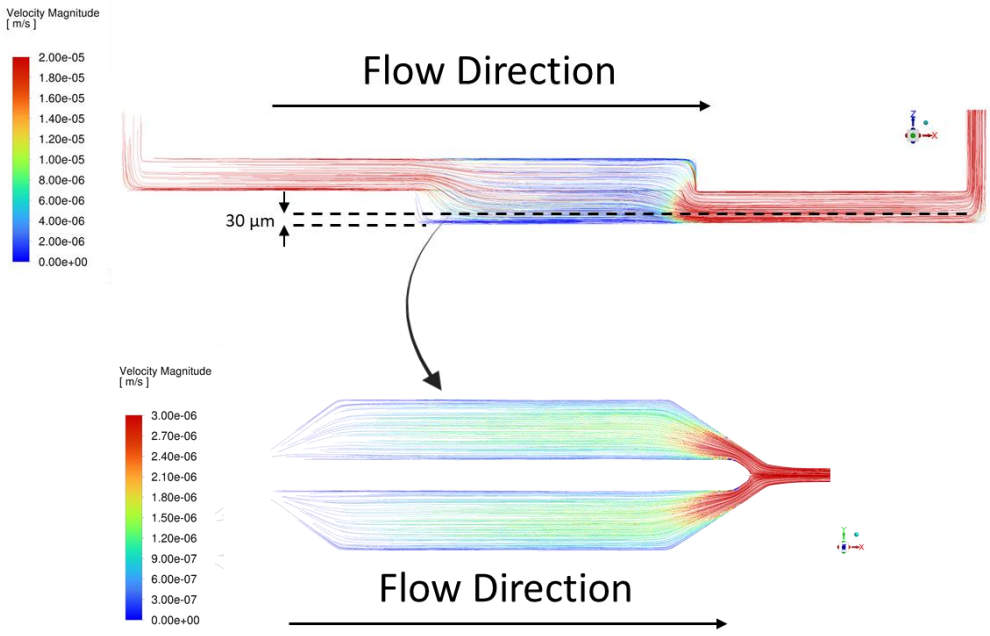

Figure 75 Flow streamlines visualized in both lateral and top views.

Although the chamber geometry imposed some constraints on reproducing physiological flow rates and shear stresses, our design strategy prioritized achieving velocity values consistent with those observed in brain tissue, as velocity was considered the most relevant parameter for this application. Since drug molecules are expected to follow the streamlines of the perfused medium in the BoC—analogous to their transport within the interstitial fluid of the brain—velocity was adopted as the primary metric to evaluate drug selectivity within the model.

Under these conditions, oxygen supply to the cultured cells was maintained at adequate levels, while the relatively low shear stresses generated within the chamber are unlikely to significantly impact mechanotransduction processes or induce cell detachment during perfusion. This concern is further mitigated by the fact that the system was exposed to medium and drug perfusion for a limited experimental timeframe.

6.2 Biological Validation

All biological experiments and protocols described in this section were conducted at the laboratories of Prof. Pasquale Picone (Consiglio Nazionale delle Ricerche – Istituto per la Ricerca e l'Innovazione Biomedica, Via U. La Malfa 153, Palermo, Italy) and collaborators, whose valuable contribution is gratefully acknowledged.

The integration of electrospun PLA scaffolds into the Brain-on-Chip (BoC) platform required a systematic biological validation to confirm their suitability for supporting neuronal and microglial cultures. To this end, a series of in vitro assays was performed to assess (i) scaffold cytocompatibility, (ii) the influence of fiber orientation on cell morphology and organization, and (iii) the preservation of cell-specific structural markers.

Furthermore, the functionality of the microfluidic device was verified through a proof-of-concept experiment, designed to assess its ability to discriminate selective interactions between bioactive compounds and distinct neural cell populations under dynamic perfusion. Together, these analyses provided a comprehensive validation of both the biomaterial substrates and the microfluidic design, demonstrating their potential for application in advanced in vitro models of the central nervous system (CNS).

To recreate a simplified brain microenvironment, two complementary CNS-relevant cell lines were selected:

- BV2 murine microglial cells, commonly employed as surrogates for primary microglia. These cells retain phagocytic activity and cytokine secretion capabilities, making them suitable for studying inflammatory responses, debris clearance, and neuroimmune interactions.
- SH-SY5Y human neuroblastoma cells, widely used as a neuronal model due to their ability to develop neuronal-like morphology and synaptic features under

differentiation protocols. They provide a robust and reproducible system to investigate neuronal viability, neurotoxicity, and neuroprotective mechanisms.

Both cell lines were cultured in Dulbecco's Modified Eagle Medium (DMEM) (Euroclone, Italy) supplemented with 10% fetal bovine serum (FBS), 2 mM L-glutamine, and 1% penicillin/streptomycin. Cells were maintained at 37 °C in a humidified incubator with 5% CO_2, with medium renewed every 48–72 hours.

To preserve optimal growth conditions, BV2 cells were subcultured at approximately 70% confluency, while SH-SY5Y cells were maintained below 80% confluency to sustain neuronal-like morphology. Both cell lines were routinely screened for Mycoplasma contamination using Hoechst staining and the N-GARDE Mycoplasma PCR detection kit (Euroclone). Morphology and proliferation rates were regularly monitored under phase-contrast microscopy to ensure cell health and consistency across all experiments.

6.2.1 Cells Cytocompatibility and Morphology

To test the biocompatibility of the fibers under static conditions, inserts with a comparable diameter to that of the 96-well plates were used. These inserts featured either aligned or random membranes. Prior to seeding, the inserts were sterilized by placing them in a 70% ethanol solution for two hours, followed by sterilization under UV light for 20 minutes on both sides. Once dry, the inserts were placed in a 48-well plate ready for cell seeding.

Cell viability was measured using the MTS assay (Promega). MTS [3-(4,5-dimethylthiazol-2-yl)-5- (3-carboxymethoxyphenyl)-2-(4-sulfophenyl)-2H-tetrazolium] was used according to the datasheet protocol. Bv2 cells and SH-SY5Y cells were seeded in triplicate into inserts with random or aligned fibers. The different seeding densities used for BV2 and SH-SY5Y cells of 6 x10-4 and 12 x10-4 cells/chamber, respectively, is due to the different replication rates of the cells. 24 hours and 7 days after seeding, 20 µl of the MTS solution was added to each well containing the cells and incubated for 4 hours at 37°C, 5% CO2. Absorbance was read at 490 nm using a Glomax microplate reader (Promega). Values are expressed as percentage of cell growth relative to day 1. At the same time, to confirm the presence of cells on the fibers and their ability to support cell adhesion and growth, cells were plated at the same concentration and for the same period of time and incubated with Hoechst 33342 trihydrochloride trihydrate for nuclear staining. Cells were then observed with an IX83 fluorescence microscope (Evident/Olympus) at 20X magnification.

The cytocompatibility of A-PLA and R-PLA fibers was evaluated with BV2 and SH-SY5Y cell lines using the MTS assay, in accordance with ISO 10993-5 guidelines. As shown in Figures 76A and 76B, formazan production was quantified by measuring optical density (O.D.) at 490 nm.

To assess the stability of cytocompatibility over time, the assay was also repeated seven days after seeding, with O.D. values normalized to those obtained at 24 hours.

The results demonstrated that both cell types adhered to the fibers and remained metabolically active, as indicated by their ability to reduce MTS to formazan, a marker of cell viability. Notably, no decrease in viability was observed compared to day 1; on the contrary, both BV2 and SH-SY5Y cells exhibited increased viability over time, confirming the sustained cytocompatibility of the fibers under prolonged culture conditions. Cell adhesion and growth on the scaffolds were further corroborated by Hoechst nuclear staining (Figures 76C and 76D).

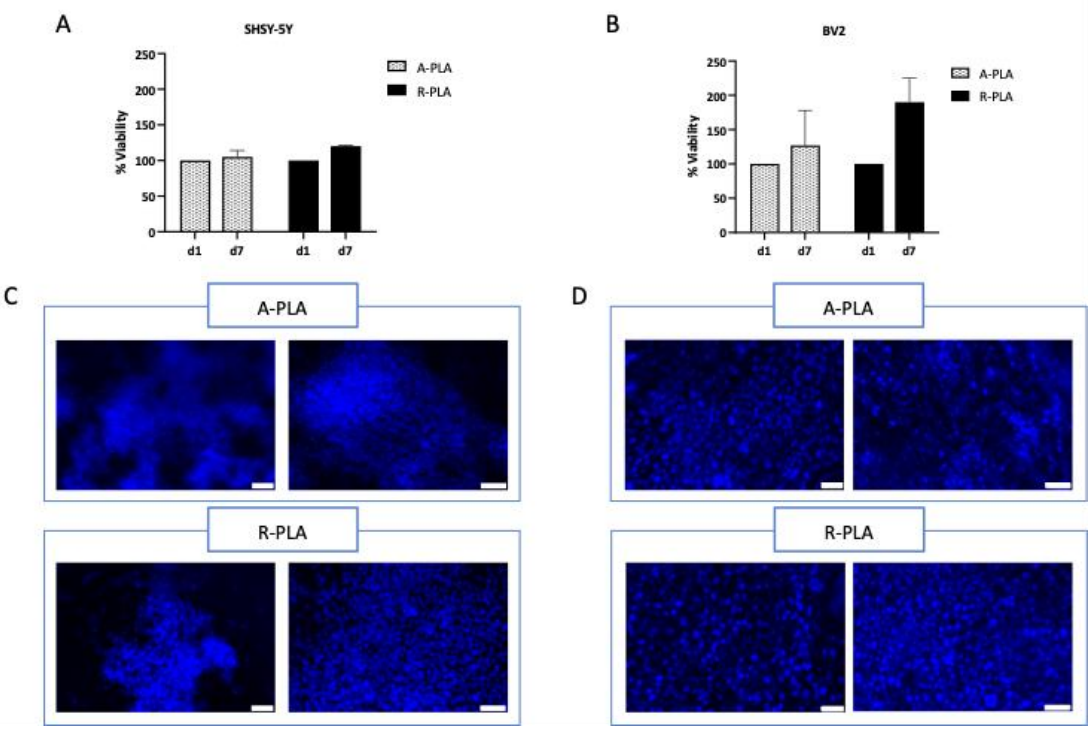

Figure 76 Cytocompatibility assessment of A-PLA and R-PLA fibers on BV2 and SH-SY5Y cells. (A, B) Cell viability was evaluated by MTS assay on BV2 (A) and SH-SY5Y (B) cell lines seeded on A-PLA and R-PLA fibers. Formazan production was measured by optical density (O.D.) at 490 nm after 24 hours and 7 days. O.D. values at day 7 were normalized to the 24-hour time point to assess the cytocompatibility over time. (C, D) Representative fluorescence microscopy images of BV2 (C) and SH-SY5Y (D) cells stained with Hoechst to visualize nuclei after 7 days of culture on the fibers. Data are presented as mean ± SEM of three independent experiments. Scale bar: 50 µm.

The morphological characterization of the fibrous scaffolds and the evaluation of cell attachment were carried out using a scanning electron microscope (SEM, Quanta 200 F, FEI, USA). Circular sections of the samples (Ø 3 mm) were mounted on aluminum stubs using conductive carbon adhesive. Prior to imaging, specimens were sputter-coated with a thin layer of gold (Sputtering Scancoat Six, Edwards Laboratories, Milpitas, CA, USA) for 120 seconds under an argon atmosphere to enhance conductivity and image resolution. SEM analysis was performed also on scaffolds retrieved from the microfluidic platform system after dynamic cell culture experiments. Scaffolds previously used for cell culture were processed for fixation and dehydration prior to SEM analysis. Samples were fixed in a 4% (v/v) paraformaldehyde (PFA) in PBS at room temperature for 30 minutes. The fixation step was followed by a dehydration process using a graded series of ethanolwater mixtures, increasing in ethanol concentration, as described in prior protocols

To further assess the influence of fiber orientation on cell–scaffold interactions, SEM imaging of BV2 and SH-SY5Y cells cultured on A-PLA and R-PLA scaffolds was performed at different time points (Figure 77). The analysis revealed that fiber alignment strongly affects cell morphology and spatial organization over time. For SH-SY5Y cells, elongation of the cell bodies (visible as darker regions) along the fiber direction was evident as early as day 1 on A-PLA scaffolds, and this directional alignment was maintained at days 3 and 7.

In contrast, on R-PLA scaffolds, SH-SY5Y cells exhibited an isotropic morphology, with randomly oriented extensions and cell bodies, independent of culture time.

A comparable behavior was observed for BV2 cells. On A-PLA scaffolds, uncovered regions at day 1 already appeared as elongated gaps aligned with the fiber axis, whereas on R-PLA scaffolds the uncovered areas formed irregular islands without preferential orientation. By days 3 and 7, BV2 cells cultured on A-PLA scaffolds progressively aligned

along the fiber direction, while on R-PLA they tended to aggregate into irregular, anisotropic clusters lacking directional organization.

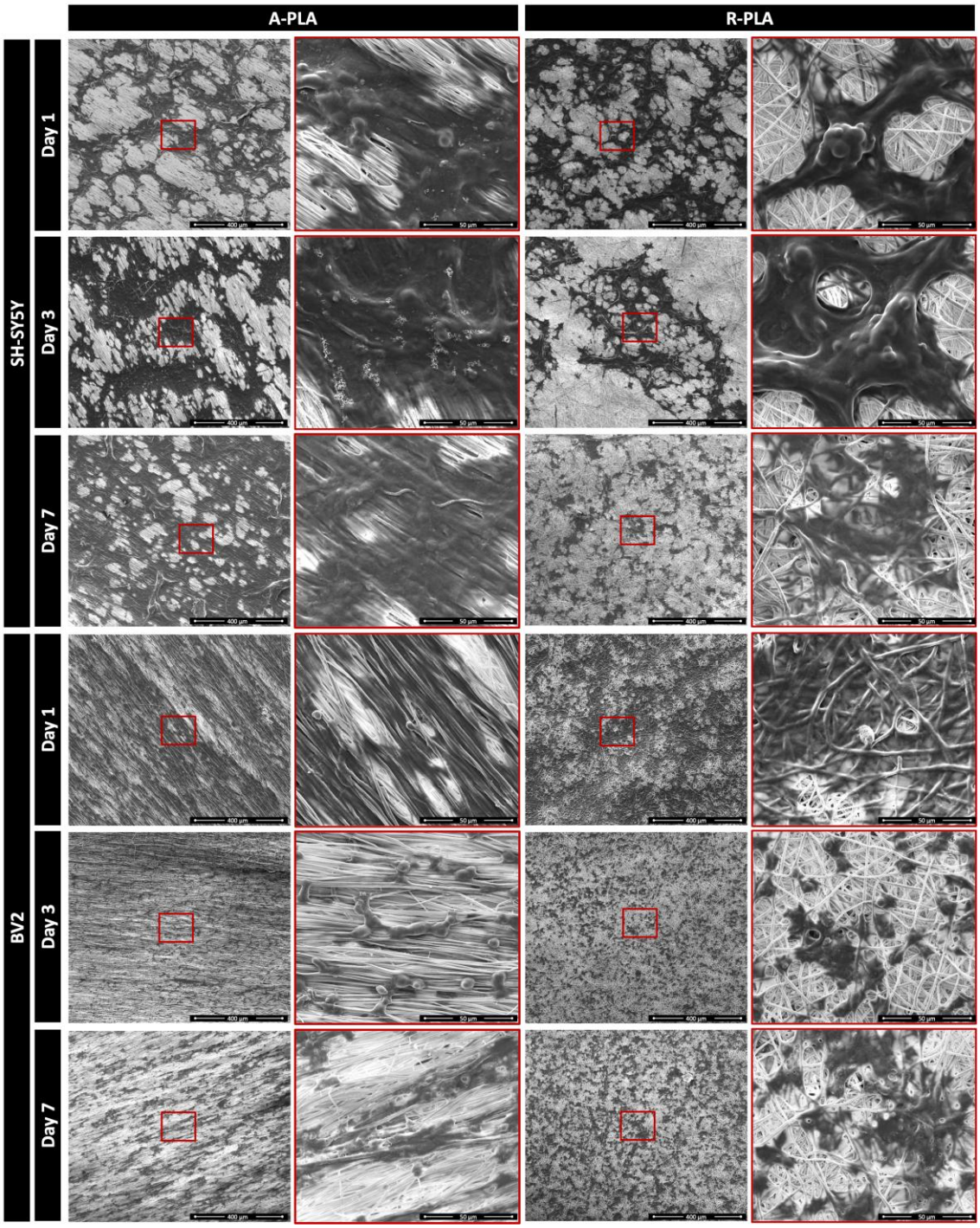

Figure 77 SEM images of SH-SY5Y and BV2 cells cultured on aligned (A-PLA) and random (R-PLA) electrospun scaffolds at days 1, 3, and 7.

These findings demonstrate that scaffold architecture plays a pivotal role in directing cell morphology and spatial arrangement from the earliest stages of culture, with aligned fibers consistently promoting oriented growth and organization in both neuronal and microglial

populations. This phenomenon can be attributed to the alignment of microfibers, which act as physical guides for cellular extensions, influencing both their growth direction and overall morphology. Indeed, substrates with oriented patterns have been shown to promote neurite alignment and elongation, thereby facilitating the establishment of coherent connections between neuronal cells [93]. This property makes aligned fibers particularly relevant for studies on electrical conduction in neuronal cultures, where the orientation of extensions is critical for effective synaptic transmission, as well as for applications in neural tissue engineering.

Conversely, randomly arranged fibers do not promote preferential alignment, resulting in a more isotropic cell morphology. Such organization may be particularly advantageous for cells with amoeboid morphology, such as microglia, whose highly dynamic shape supports phagocytic activity and independent migration without constraints from substrate orientation [94]. Therefore, *in vitro* studies of cell populations involved in immune response and brain inflammation may benefit from the use of randomly organized fibers.

Nevertheless, further studies are required to elucidate the cellular mechanisms underlying the directional effects of substrate architecture on cell behavior.

6.2.2 Evaluation of cellular structural markers

β-tubulins are structural components of the microtubule network and are involved in essential cellular processes such as proliferation and motility. Among them, β-tubulin III is commonly used as a marker of neuronal identity due to its specific expression in neurons and its role in axonal maintenance [95], [96]. Microtubule-associated proteins (MAPs) also regulate microtubule organization and function; in particular, MAP2 is selectively expressed in neurons, where it contributes to cytoskeletal stability and supports multiple neuronal functions [97] [98].

In this work, β-tubulin III and MAP2 were employed as reference markers to assess the effect of scaffold architecture on the structural and functional status of SH-SY5Y neuronal cells. Twenty-four hours after seeding, BV2 and SH-SY5Y cells were fixed with 4% paraformaldehyde for 15 minutes and permeabilized with 0.1% Triton X-100 in PBS for 10 minutes at room temperature. Subsequently, they were blocked with 2% BSA at room temperature for 1 hour and incubated with primary antibodies to MAP2 (SC74421), β-tubulin III (c.s 5568s), IBA1 (c.s 17198s) overnight at 4o C in a humidified chamber. Subsequently, incubation with secondary antibodies conjugated with Alexa Fluor 488

(1:1000) (MAP2) and Alexa Fluor 546 (1:1000) (IBA1 and β-tubulin III) was performed for 1 hour in the dark at room temperature. Finally, the cells were washed with PBS and stained with DAPI (1 µg/mL) for 7 minutes in the dark at room temperature. Fluorescence imaging was performed with the IX83 fluorescence microscope (Evident/Olympus) at a magnification of 20X. Immunofluorescence analysis revealed strong and consistent expression of both markers in cells cultured on random (R-PLA) and aligned (A-PLA) electrospun membranes (Figure 78).

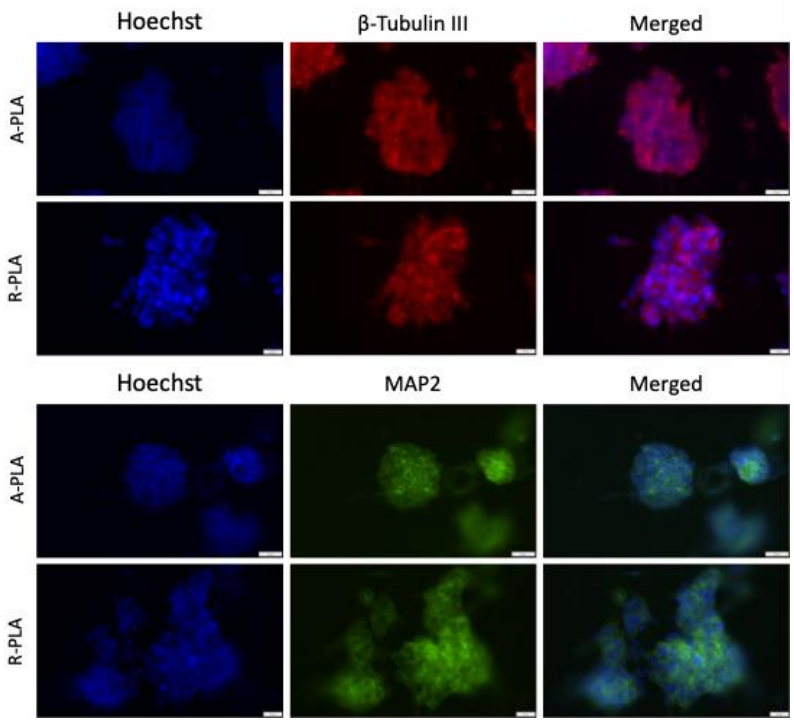

Figure 78 Immunofluorescent distribution of β-tubulin III and MAP2 in SH-SY5Y cells cultured on random and aligned fiber membranes. Representative images of Immunostaining for β-tubulin III (green), MAP2 (red), Hoechst (blue) Bar: 20 µm.

From an engineering perspective, these findings confirm that the proposed scaffold fabrication strategies do not negatively impact neuronal structural organization, thus supporting their suitability for integration into the Brain-on-Chip platform.

IBA1 (Ionized Calcium-Binding Adapter Molecule 1) is a cytoplasmic protein encoded by the *AIF1* (Allograft Inflammatory Factor 1) gene and commonly used as a marker for microglial and macrophage populations, due to its selective expression in these cell types [99] [100]. Functionally, IBA1 is involved in cytoskeletal regulation through interactions with actin, supporting processes such as morphology adaptation, migration, and phagocytosis.

In the context of this study, IBA1 expression was evaluated in BV2 cells cultured on both aligned (A-PLA) and random (R-PLA) electrospun scaffolds, with the objective of assessing whether the substrate architecture could influence cytoskeletal organization. Immunofluorescence analysis revealed consistently strong IBA1 staining in all experimental conditions (Figure 79).

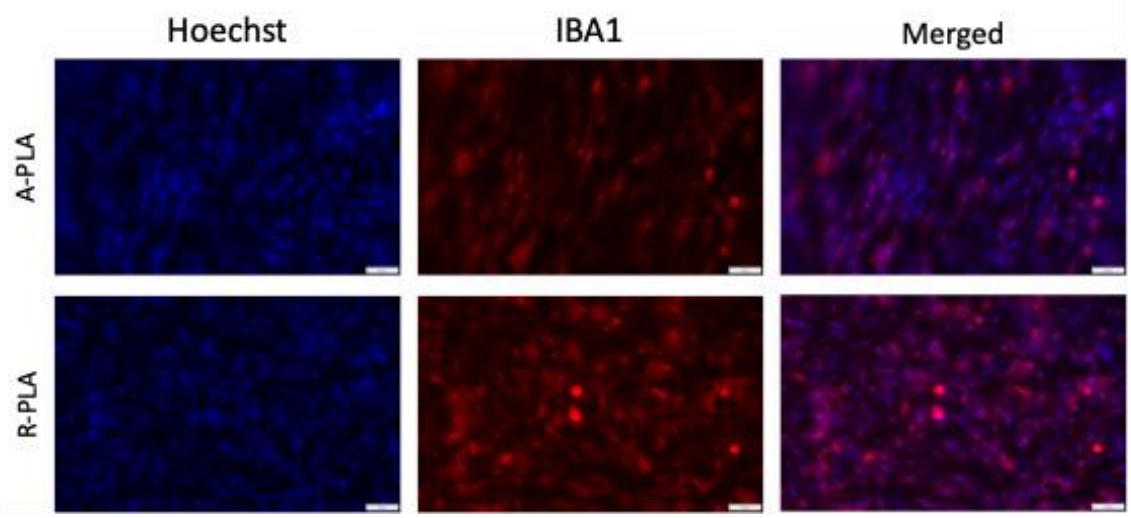

Figure 79 Immunofluorescent distribution of IBA1 in BV2 cells cultured on random and aligned fiber membranes. Representative images of Immunostaining for IBA1 (red), Hoechst (blue). Scale bar 50 µm.

From an engineering perspective, these results validate that the scaffold fabrication approach—independent of fiber orientation—preserves the functional integrity of microglial cells, thereby confirming the biocompatibility and suitability of the proposed substrates for integration into the Brain-on-Chip platform.

6.2.3 Chip for Assessing Cell-Specific Drug Selectivity

To evaluate the ability of the Brain-on-Chip platform to discriminate drug selectivity across different cell populations, a proof-of-concept experiment was performed using myelin-derived nanovesicles (MyVes), which are known to preferentially interact with microglial cells [101,102]. To perform studies under dynamic conditions, Microfluidic platform chips featuring either aligned or random membranes were used. Before seeding, the chips were sterilized by placing them in a 70% ethanol solution for 2 hours and then sterilized under UV light for 20 minutes. After allowing the chips to dry, 6 x10-4 cells/chamber of BV2 and 12 x 10-4 cells/chamber of SH-SY5Y were plated. For this study,

MyVes were fluorescently labeled (MyVes-Atto633) and perfused through the device under continuous flow conditions, followed by a 2-hour incubation.

Myelin nanovesicles (MyVes) were prepared using a nanoprecipitation method as previously described [20,21]. Briefly, myelin extract was dissolved in DMSO at a concentration of 2 mg/mL and sonicated for 30 minutes at 35 kHz. Subsequently, this solution was added dropwise ultrapure water (volume ratio DMSO/water 1:20) under vigorous agitation using an Ultraturrax homogenizer (8000 rpm, 15 minutes). The resulting suspension was purified by repeated ultracentrifugation (30 minutes at 50,000 rpm), redispersed in ultrapure water, and then freeze-dried. Fluorescently labeled MyVes were obtained from the freeze-dried nanovesicles. The lyophilized MyVes were redispersed in DPBS (pH 7.4) at a concentration of 2 mg/mL. To this dispersion, 50 µL of Atto 633 NHS ester in DMSO (2 mg/mL) was added. The mixture was incubated for 2 hours in the dark to allow for conjugation, followed by ultracentrifugation (30 minutes at 50,000 rpm). The vesicles (MyVes-Atto633) were then washed three times with ultrapure water, each followed by ultracentrifugation under the same conditions. Finally, the fluorescent MyVes were redispersed in 2 mL of ultrapure water and freeze-dried. Twenty-four hours after seeding, the cells in the chip were treated with a 30 µg/ml MyVes-Atto633 solution in the culture medium. The pump flow was started at a rate of 1.39 ml/h for 2 hours. The cells were then washed in PBS and stained with Hoechst to detect nuclei. Fluorescence was first detected using a Typhoon FLA 9500 and then using with the IX83 fluorescence microscope (Evident/Olympus) at a magnification of 4X.

The distribution of vesicles within the BoC was assessed by two complementary imaging techniques: a fluorescence scanner, which enabled full-device visualization and simultaneous observation of both chambers, and high-resolution fluorescence microscopy, which provided detailed confirmation of vesicle internalization. Both approaches consistently revealed fluorescence signals exclusively in the microglial compartment, regardless of scaffold fiber orientation (random or aligned, Figure 80).

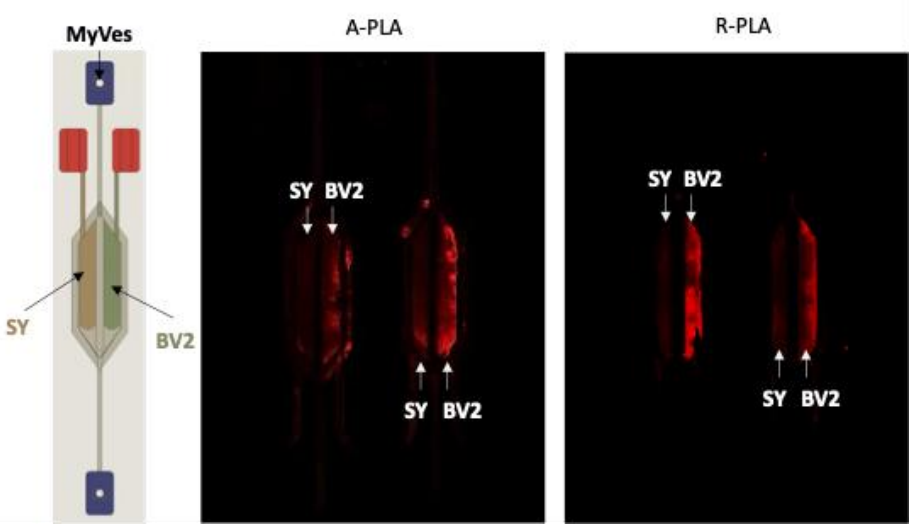

Figure 80 Fluorescence analysis of MyVes-Atto633 interaction with microglial and neuronal cells cultured in microfluidic chips. Fluorescently labelled MyVes were introduced into the microfluidic chip and incubated under continuous flow for 2 hours. The fluorescence images of the chips were detected using fluorescence scanner.

From an engineering standpoint, these results validate the functionality of the microfluidic design in enabling selective delivery and real-time discrimination of drug–cell interactions within a controlled co-culture environment. Moreover, the use of dynamic perfusion strengthens the physiological relevance of the system, confirming its suitability as an advanced *in vitro* platform for drug selectivity and screening studies.

To gain a more detailed understanding of vesicle distribution within the chip, fluorescence microscopy analysis was performed (Figure 81). By employing a 4× objective, it was possible to visualize both chambers simultaneously, clearly separated by the central septum. The acquired images revealed that fluorescence signals were confined exclusively to the compartment containing microglial cells, fully consistent with the results previously obtained using the fluorescence scanner.

This outcome not only confirms the selective tropism of MyVes for microglia but also provides further validation of the chip as a reliable platform for investigating drug or delivery system selectivity. In particular, the ability to reproduce controlled and dynamic

microenvironmental conditions highlights the potential of the device for applications in advanced *in vitro* drug testing.

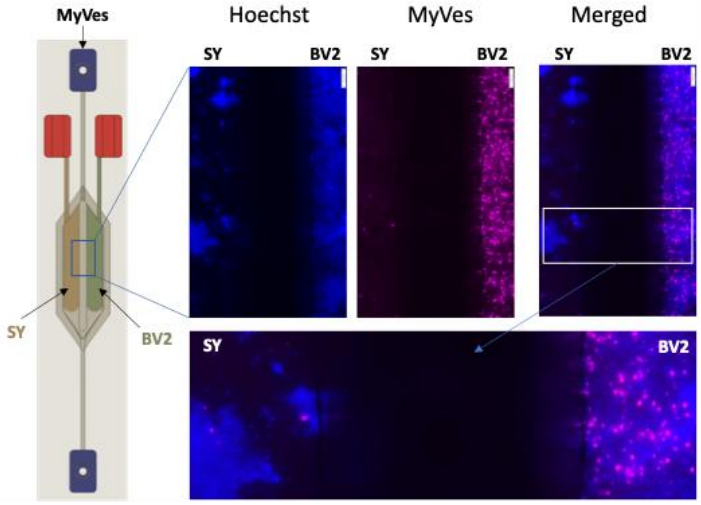

Figure 81 Fluorescence microscopy analysis of MyVes-Atto633 distribution in the microfluidic chip. Representative image of MyVes labelled with Atto 633 (purple) and Nuclei with Hoechst (blue) were acquired at 4X magnification.

6.3 Discussion and Perspectives

In this application, was reported the design, fabrication, and validation of an innovative Brain-on-Chip (BoC) platform specifically developed to investigate drug selectivity in heterogeneous neural cell populations. The device integrates an electrospun PLA-based scaffold within a microfluidic architecture that enables the co-culture of distinct cell types in spatially separated compartments, interconnected by a shared perfusion environment. By modulating flow parameters to reproduce physiological or pathological conditions, the system provides *in vivo*–like drug delivery and allows the assessment of compound selectivity.

A key feature of the platform is the fluidic isolation achieved during cell seeding, followed by controlled interconnection during perfusion, without compromising scaffold integrity or cell adhesion. The successful incorporation of both aligned and random electrospun fiber architectures further highlights the versatility of the system in recapitulating tissue-specific cues. Results demonstrated that brain cells adhered efficiently to both scaffold types, maintaining high viability over time, thus confirming the excellent cytocompatibility of the substrates. Moreover, analysis of structural proteins revealed

preserved cellular organization on both architectures, supporting their suitability for advanced brain tissue models.

The proof-of-concept co-culture experiment, combining neurons and microglia in distinct compartments exposed to a shared flow of myelin-derived nanovesicles (MyVes), confirmed the selective uptake of MyVes by microglial cells under physiologically relevant flow conditions. Overall, these findings validate the BoC platform as a robust and versatile system for advanced studies on drug selectivity and screening within complex neural microenvironments.

7 ISO-Compliant OoC

The final project focused on the development of an innovative microfluidic device conceived as a pivotal platform for biomedical research, particularly within the field of Organ-on-Chip (OoC) technology. OoCs are widely recognized for their potential to revolutionize drug development and disease modelling; however, conventional devices still face significant limitations, including poor scalability, limited reproducibility, and challenges in meeting regulatory standards. Moreover, the absence of standardized fabrication protocols has hindered the large-scale adoption of these systems in industrial and clinical contexts.

To address these issues, was designed and realized a thermoplastic microfluidic device fully compliant with ISO standards and tailored for industrial-scale production through rapid prototyping strategies, such as laser micromachining and thermal bonding.

This section focuses on the design and fabrication of a novel iso-compliant multiscaffold microfluidic device, which was developed during my research stay abroad under the supervision of Prof. Virginia Pensabene at the *School of Electronic and Electrical Engineering* (Faculty of Engineering) and the *School of Medicine, Leeds Institute of Medical Research (LIMR)* at St. James's University Hospital.

The platform integrates a dual-scaffold system: an aligned electrospun polylactic acid (A-PLA) membrane, mimicking endothelial tissue architecture, and an ionically crosslinked alginate hydrogel (Alg-H), providing a three-dimensional cellular microenvironment. This configuration combines the structural anisotropy of electrospun fibers with the versatility of hydrogels, thereby recreating a biomimetic milieu with enhanced physiological relevance.

By overcoming key obstacles in scalability and reproducibility, this ISO-compliant device establishes a reliable and cost-effective framework for preclinical research, drug testing, and tissue engineering. Furthermore, its design ensures compatibility with regulatory pathways and high-throughput screening, bridging the gap between academic research and industrial translation. Overall, this platform represents a promising step toward the broader implementation of OoC technologies, offering robust, standardized, and ethically sustainable alternatives to traditional animal models in pharmaceutical development.

7.1 Rationale device

The microfluidic device was designed to reproduce a physiologically relevant co-culture environment by integrating two distinct scaffolding strategies within a single thermoplastic ISO-compliant platform (Figure 82). The architecture consists of an upper and lower culture chamber separated by an electrospun membrane and a hydrogel compartment. The electrospun polylactic acid (A-PLA) membrane, composed of aligned fibers, provides a biomimetic ECM-like substrate that supports the adhesion and growth of epithelial or endothelial cells, while permitting the exchange of nutrients and signaling molecules through its porous structure. Beneath the membrane, an ionically crosslinked alginate hydrogel (Alg-H) serves as a three-dimensional cell-laden matrix, enabling the embedding of stromal or parenchymal cells and recreating complex tissue–tissue interfaces.

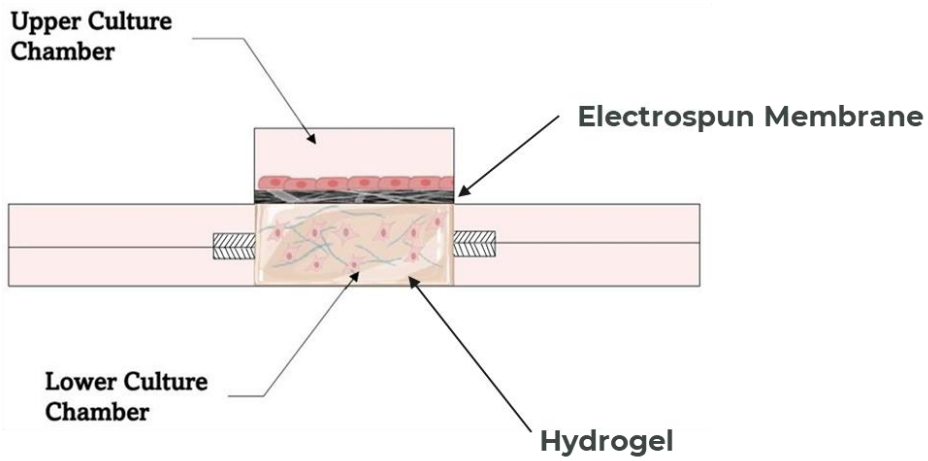

Figure 82 Schematic representation of the dual-scaffold microfluidic device. The architecture consists of an upper and a lower culture chamber separated by an electrospun membrane and an alginate hydrogel compartment. In addition, the device includes lateral microchannels for culture medium administration, which will be described in detail in a later section.

This dual-scaffold configuration overcomes the limitations of conventional 2D monocultures and single-scaffold approaches by combining the barrier function of nanofibrous membranes with the 3D cell–matrix interactions provided by hydrogels. As a proof of concept, Human Umbilical Vein Endothelial Cells (HUVECs) were seeded on the A-PLA scaffold to mimic the vascular compartment, while human mammary carcinoma epithelial cells (MDA-MB-231) were cultured within the Alg-H hydrogel matrix, generating a hybrid 2D/3D tissue construct inside the microfluidic platform.

By leveraging rapid prototyping techniques such as CO_2 laser micromachining and thermal

bonding, this device was realized in thermoplastic material conforming to ISO 22916:2022, ensuring reproducibility, standardization, and scalability. This innovative approach not only facilitates the construction of physiologically relevant tissue models for drug testing and tissue engineering but also bridges the gap between academic research and industrial translation, paving the way for the regulatory adoption and large-scale implementation of Organ-on-Chip technology.

7.2 Design of the ISO-Compliant Microfluidic Device

The microfluidic device was designed using *Autodesk Fusion 360*™ in compliance with ISO 22916:2022, which establishes interoperability requirements for microfluidic systems. The design adhered to standardized dimensional tolerances, including port pitches, chip thickness, and top connection port dimensions, to ensure reproducibility and seamless integration with existing microfluidic platforms. Specifically, four 6 mm × 6 mm square inlet/outlet regions were defined, each with a centrally positioned port, maintaining a 6 mm pitch to facilitate standardized interfacing and minimize leakage, (Fig. 83). The device has a total thickness of 2.6 mm and overall dimensions of 30 mm × 60 mm, maintaining structural integrity and facilitating integration with standard microfluidic connections.

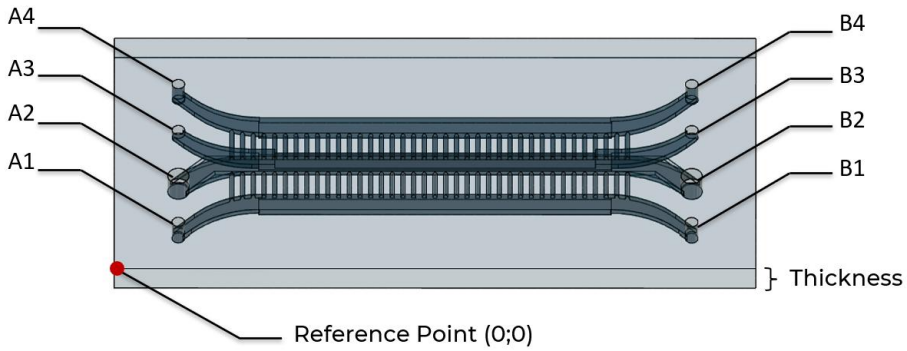

Figure 83 CAD design of the ISO-compliant microfluidic device created in Autodesk Fusion 360™. The layout includes four inlet/outlet regions (A1–A4, B1–B4) with 6 × 6 mm square ports arranged at a 6 mm pitch to ensure standardized interfacing and minimize leakage. The reference point (0;0) is indicated according to the ISO-norm. The device has an overall thickness of 2.6 mm and dimensions of 30 × 60 mm, in accordance with ISO 22916:2022 guidelines for microfluidic interoperability.

To accommodate the fabrication constraints, the device was engineered as a multi-layered structure composed of polymeric sheets of varying thicknesses, whit a total thickness of 2,6 mm. This configuration enables the integration of two distinct scaffold materials: (i)

an electrospun A-PLA scaffold, which is physically embedded within the device, and (ii) an in situ crosslinkable Alg-H, (Figure 84).

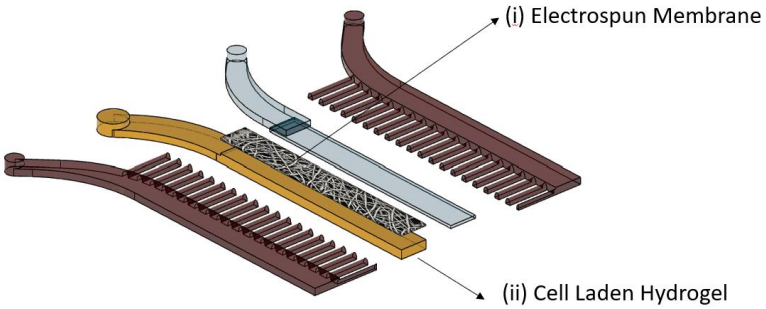

Figure 84 Exploded CAD view of the dual-scaffold microfluidic device. The architecture integrates (i) an electrospun membrane, designed to mimic the extracellular matrix and support cell adhesion, and (ii) a cell-laden hydrogel, providing a three-dimensional environment for parenchymal or stromal cell culture. This configuration enables the reconstruction of complex tissue–tissue interfaces within a standardized microfluidic platform.

The lower compartment is permeated by a microchannel array, allowing controlled diffusion of nutrients and gases while maintaining a physiologically relevant microenvironment for 3D cell culture applications.

The device was constructed as a multilayer thermoplastic microfluidic system designed to integrate both electrospun and hydrogel scaffolds within an ISO-compliant architecture. The exploded view in Figure 85 illustrates the six layers composing the device and their respective thicknesses and functions.

The upper compartment includes two layers (3 mm total thickness) containing four inlet/outlet ports (Ø 1.48 mm) specifically dimensioned through preliminary pressure resistance tests to ensure leak-free microfluidic connections. These layers primarily serve as sealing and connection supports.

Layer I (0.5 mm) acts as a closing lid for the upper portion of the device.

Layer II (0.2 mm) incorporates the access channels leading to the upper culture chamber.

Layers III and IV (0.2 mm each) provide mechanical support for the housing of the electrospun membrane, ensuring proper alignment and confinement between the upper and lower chambers.

Layer V (1 mm total, composed of two 0.5 mm sublayers) forms the central chamber of the device, which accommodates the hydrogel, lateral microchannels, and nutrient diffusion channels.These microchannels allow controlled exchange of nutrients and gases while

facilitating the delivery of the $CaCl_2$ crosslinking solution to the hydrogel compartment, ensuring uniform gelation.

Layer VI (0.5 mm) constitutes the bottom base, sealing the structure and completing the assembly.

The total thickness of the device is 2.6 mm, consistent with ISO 22916:2022 specifications for microfluidic interoperability.

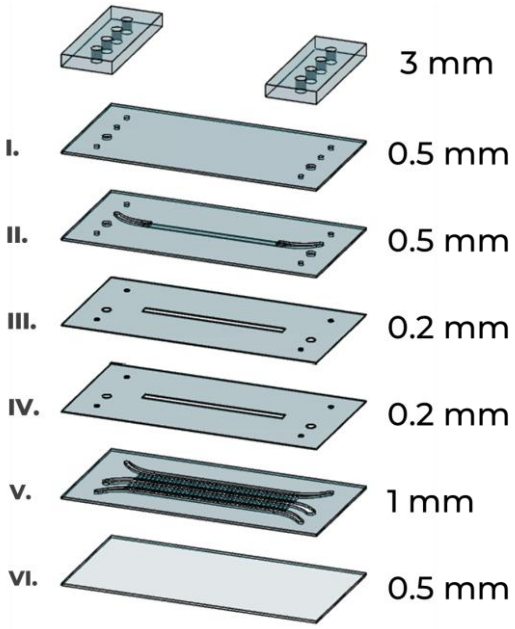

Figure 85 Exploded view of the multilayer ISO-compliant thermoplastic microfluidic device.

The dimensional layout of the microfluidic device was defined to ensure precision and reproducibility during fabrication via CO_2 laser micromachining. Figure 86 reports the technical drawing of the individual layers, illustrating all key geometric parameters and interconnections. Each component was designed to comply with the ISO 22916:2022 standard for microfluidic interoperability, including standardized inlet/outlet port diameters (Ø 1.2 mm and Ø 2 mm), chip footprint (30 × 60 mm), and port spacing.

The design incorporates gently curved microchannels (radius ~7 mm) to facilitate smooth fluid flow and minimize shear stress during cell culture experiments. The channel width of 2 mm and inter-channel spacing of 3 mm were selected to maintain laminar flow regimes and efficient nutrient diffusion. The precision of these dimensions ensures alignment between layers during assembly, supporting consistent fluidic performance and reliable biological testing within the integrated multi-scaffold system.

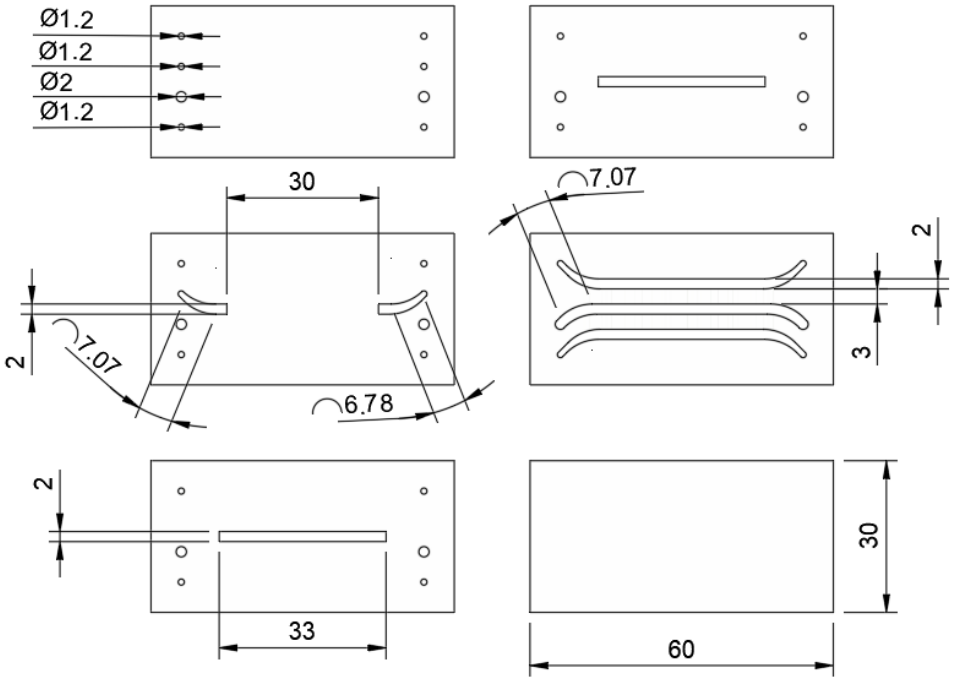

Figure 86 Technical drawing of the ISO-compliant microfluidic device showing the detailed geometrical layout and cutting dimensions of each layer. Measurements are expressed in mm.

Before finalizing the fabrication process, a set of optimization tests was performed to determine the most suitable parameters for laser micromachining of the thermoplastic layers. These tests aimed to ensure high-fidelity reproduction of the microchannel geometry and to prevent deformation or surface damage during fabrication.

7.2.1 Channels Shape Characterization

The CAD model of the microfluidic device was generated to define the geometry and dimensions of each individual layer. Preliminary optimization of the laser cutting process was carried out in a defocused configuration (Figure 87), testing different focal distances ranging from 30 to 35mm, in order to identify the condition that provided the most uniform and reproducible microchannel engraving.

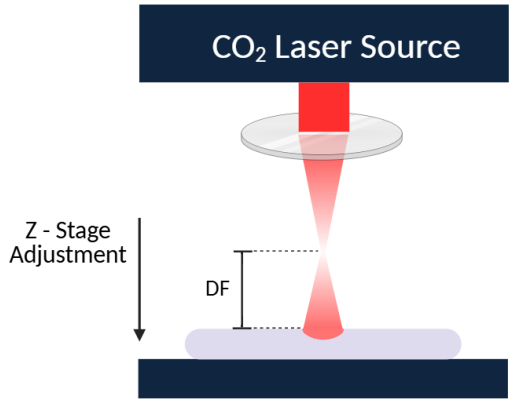

Figure 87 Schematic representation of the CO_2 laser micromachining setup in defocused configuration. The focal distance (DF) was varied by adjusting the Z-stage, allowing control over the beam spot size and energy distribution on the PMMA substrate for microchannel engraving

In the initial trials, a center-to-center spacing of 1 mm between adjacent channels was employed. However, this configuration resulted in excessive thermal damage, leading to localized deformation of the PMMA substrate. To mitigate overheating, the spacing was increased to 1.5 mm, which markedly improved the definition and structural integrity of the microchannels (Figure 88). Both channel height and width were mapped to assess reproducibility and dimensional accuracy.

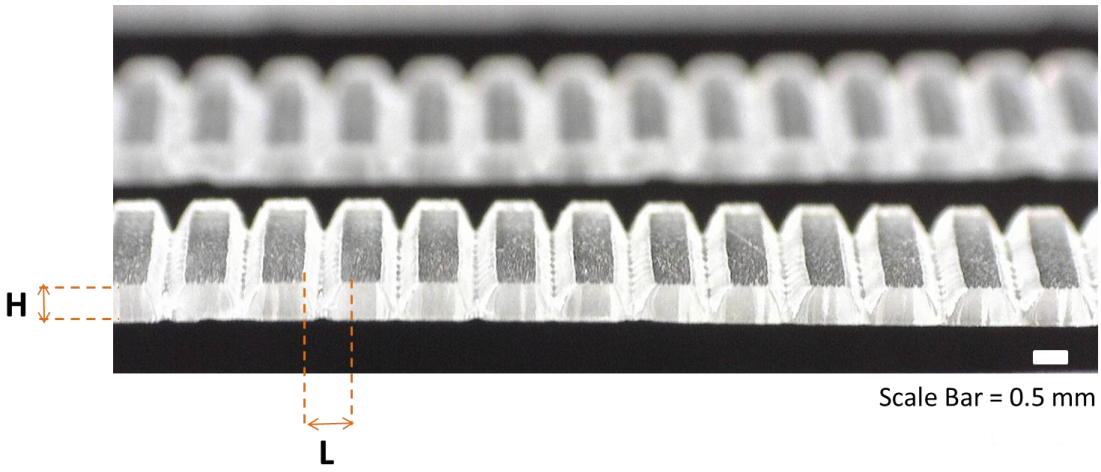

Figure 88 Cross-sectional view of laser-engraved PMMA microchannels obtained with a center-to-center spacing of 1.5 mm. Increasing the spacing from the initial 1 mm configuration prevented excessive thermal damage and localized deformation, resulting in well-defined channel geometry with improved structural integrity.

Subsequently, microstructured layers were fabricated and subjected to morphological analysis by scanning electron microscopy (SEM). Each row of microchannels was characterized immediately after laser cutting, after ultrasonic cleaning, and finally following combined ultrasound treatment and chloroform vapor exposure, in order to assess the impact of post-processing steps on surface quality and microchannel fidelity.

To this end, several characterization experiments were conducted using a CO_2 laser cutter set at 15% power and 100 mm/s speed. Different defocused configurations were tested by varying the focal distance (DF) to 30 mm, 32.5 mm, and 35 mm.

SEM micrographs revealed that the morphology of the laser-engraved microchannels after cleaning and post-processing varied as a function of the DF parameter. As shown in Figure 89, the channels fabricated at DF = 30 mm exhibited sharper edges and higher surface roughness, while increasing the focal distance to 35 mm produced smoother and more uniform surfaces with a well-defined ellipsoidal cross-section.

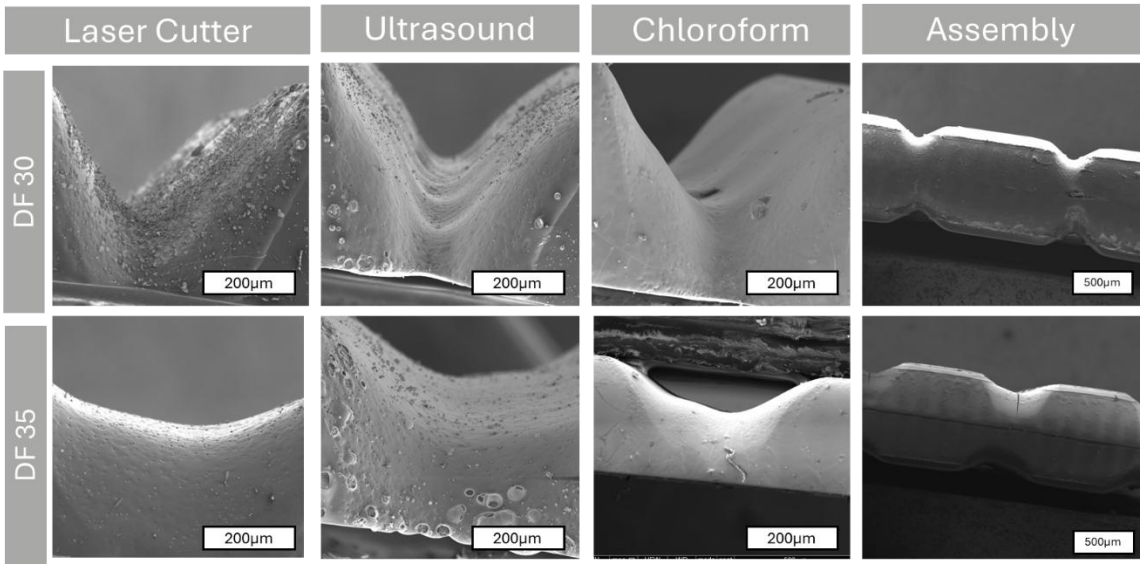

Figure 89 SEM micrographs illustrating the effect of different fabrication and bonding treatments on PMMA microchannel morphology for devices produced with two laser defocus distances (DF 30 and DF 35). Columns show representative cross-sections after laser cutting, ultrasonic cleaning, chloroform vapor exposure, and final device assembly. Samples treated with chloroform exhibited smoother channel surfaces and improved interlayer adhesion, while excessive solvent exposure led to partial deformation at the bonding interface. Scale bars: 200 µm (Laser Cutter–Chloroform) and 500 µm (Assembly).

Although the resolution of laser micromachining is relatively lower compared to other prototyping techniques, this method enabled precise control over channel geometry and depth, allowing accurate definition of the final dimensions. Moreover, the subsequent bonding step—performed under controlled heat and pressure—did not induce structural deformation. On the contrary, the microchannels preserved their shape and demonstrated excellent interlayer adhesion, confirming the suitability of this fabrication approach for reliable microfluidic device assembly.

Table 4 summarizes the laser cutting parameters used for the fabrication of the individual layers, which were adjusted to meet the specific structural requirements of the device design.

Table 4 Laser Cutter Parameters

Layer thickness	***Power***	***Speed***	***Modality***
2 mm	30%	15 mm/s	Cut
1 mm	30%	15 mm/s	Cut
0,5 mm	15%	15 mm/s	Cut
0,5 mm	15%	15 mm/s	Engraving
0,2 mm	10%	15 mm/s	Cut

Figure 90a shows the 2D model of the device generated in the *AutoLaser* software, illustrating the arrangement and geometry of the various structural components. Figure 90b presents the corresponding PMMA layers immediately after the laser cutting process, arranged and ready for assembly.

All layers were cut using a standard focal distance of 20.998 mm. However, for the fabrication of the perpendicular microchannels—spaced 1.5 mm apart—a defocused configuration with a focal distance of 32.5 mm was employed to achieve optimal engraving quality and uniform channel morphology.

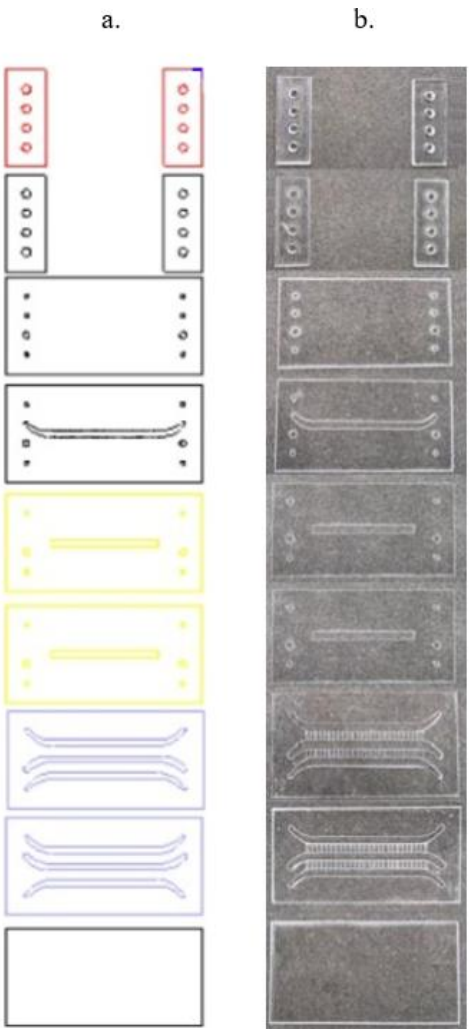

Figure 90 Schematic and physical representation of the laser-cut PMMA layers composing the ISO-compliant microfluidic device. (a) 2D model generated in AutoLaser software showing the geometrical layout and sequence of the individual layers used for device assembly. (b) Corresponding PMMA layers immediately after laser cutting, arranged in the order of assembly from top to bottom, displaying precise contour definition and alignment of the inlet/outlet ports and microchannels.

After laser cutting and alignment of all PMMA layers, the device was assembled using a thermal bonding process to ensure complete sealing and optical transparency across the layers. This step was critical to preserve microchannel geometry and avoid deformation or delamination during operation. The final device, shown in Figure 91, displays excellent alignment of the inlet/outlet ports and microchannels, with a clear visualization of the central chamber and lateral perfusion pathways. The result confirms the mechanical stability and dimensional accuracy of the thermally bonded multilayer structure, suitable for subsequent biological and fluidic testing.

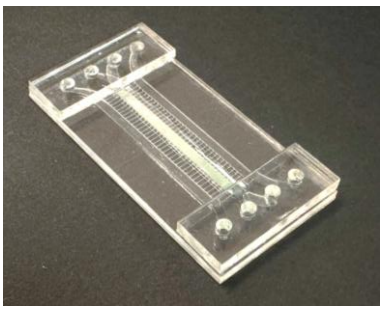

Figure 91 Final ISO-compliant microfluidic device after thermal bonding. The assembled PMMA-based chip exhibits precise layer alignment, clear microchannel definition, and optical transparency, enabling real-time microscopic observation during cell culture experiments.

7.3 Hydrogel Integration and Morphological Evaluation

Before initiating cell culture experiments, preliminary tests were conducted to evaluate the loading and crosslinking behavior of alginate-based hydrogels within the microfluidic device.

A 1% (w/v) $CaCl_2$ crosslinking solution, supplemented with a food-grade dye for visualization, was introduced into the channels using a 5 mL Luer Lock syringe connected to the device via silicone tubing and microfluidic connectors. After removing air bubbles, the crosslinking solution was perfused until complete channel filling and subsequently sealed with occluders.

The alginate hydrogel precursor solution was then loaded into the hydrogel channel using a pipette, and crosslinking was allowed to proceed for 15–20 min. Following gelation, the device was delaminated to assess hydrogel integrity and crosslinking efficiency.

The architectural design of the device was subsequently validated through morphological evaluation of the ionically crosslinked hydrogel integrated within the microfluidic platform at different time points (24 h, 48 h, and 72 h) (Figure 92). Following the injection of the alginate-based polymeric solution and its in situ crosslinking, the hydrogel exhibited a homogeneous distribution and strong adhesion to the inner walls of the microchannel, without obstructing the lateral perfusion channels responsible for nutrient and medium exchange.

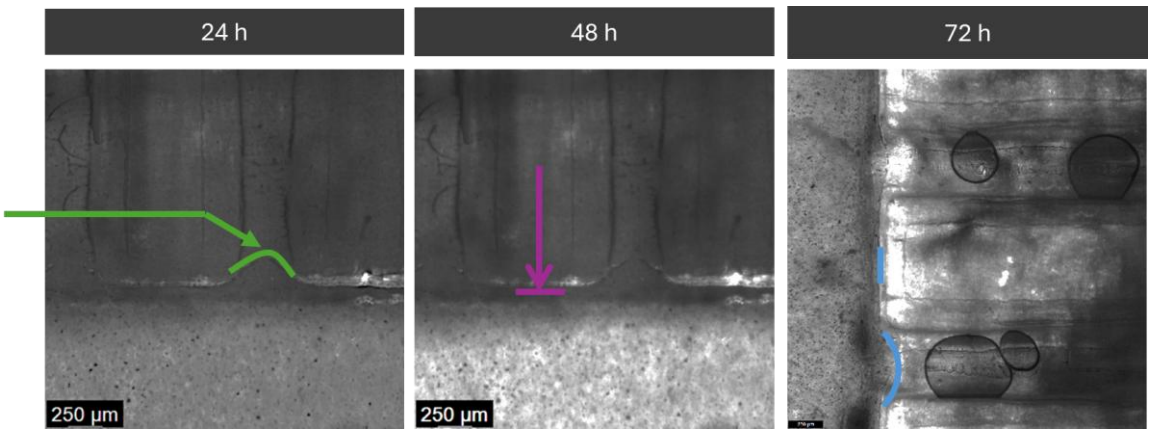

Figure 92 Morphological evaluation of the ionically crosslinked alginate hydrogel integrated within the microfluidic device at different time points (24 h, 48 h, and 72 h).

At 24 hours, a distinct and continuous interface between the hydrogel and the surrounding thermoplastic structure was observed, confirming its effective confinement within the designated compartment. After 48 hours, the hydrogel maintained uniform morphology and structural integrity, with no signs of detachment or leakage. Even after 72 hours of incubation in HPBS, the hydrogel preserved its three-dimensional structure and adhesion to the device walls, demonstrating dimensional stability and chemical compatibility with the thermoplastic material.

Overall, these findings validate the optimized microchannel geometry and material selection, which prevent clogging while ensuring reliable hydrogel anchorage. This stability under static conditions supports the feasibility of using the device for dynamic cell culture experiments, where continuous perfusion and long-term mechanical integrity are essential.

7.4 Atomic Force Microscopy (AFM)

Atomic Force Microscopy (AFM) analysis confirmed the surface morphology and alignment of the electrospun PLA scaffold. As shown in the 3D surface topography map (Figure 93), the fibers exhibited a well-defined periodic pattern with uniform orientation, demonstrating the effectiveness of the electrospinning parameters in achieving controlled alignment.

The color scale, ranging from −1.3 µm to +1.5 µm, reflects the topographical variations along the fiber surface, where lighter regions correspond to elevated areas and darker regions to depressions. The homogeneous distribution and absence of surface defects indicate that

the process ensured consistent fiber morphology and reproducibility across the scaffold. This organized fibrous architecture provides a biomimetic topography that can promote cell alignment and guide cellular organization, key features for tissue engineering and organ-on-chip applications.

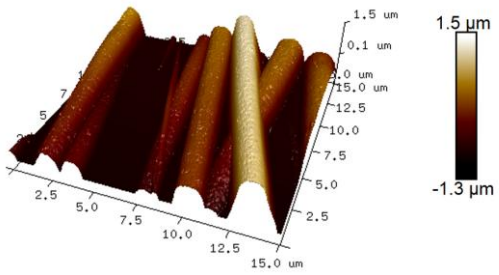

Figure 93 3D AFM topography of the PMMA surface after laser micromachining, showing the characteristic periodic ridges generated by the cutting process. The measured height profile indicates surface variations between –1.3 µm and +1.5 µm, confirming the presence of micrometric roughness along the machining direction.

A 3D surface topography map of the electrospun PLA scaffold with aligned fibers was obtained through AFM. The color scale represents height variations, with lighter regions indicating elevated areas and darker regions corresponding to depressions. The aligned fiber structure is clearly visible, with a periodic pattern and uniform orientation, confirming the effectiveness of the electrospinning process in achieving controlled fiber alignment. Moreover, the fibers appear homogeneous, with no evident defects, further demonstrating the consistency of the electrospinning process.

7.5 Biological Validation: HUVECs and MDA-MB-231 Cultures

Electrospun scaffolds were customized and assembled into an insert-like device with a culture area equivalent to a standard 96-well plate and then sterilized by immersion in a 70% ethanol solution for 1 hour, followed by UV exposure for 30 minutes.

HUVECs (Human Umbilical Vein Endothelial Cells, Lonza, Switzerland) were cultured in endothelial cell medium supplemented with 10% of fetal bovine serum (FBS), and 1% Pen-Strep mixture. Insert-like devices were put into a 24 well plate and then a suspension of 25,000 cells was then seeded onto the electrospun scaffolds.

7.5.1 Seeding of MSCs in Hydrogels

MDA-MB-231 cells were cultured into Dulbecco's Modified Eagle Medium (DMEM) and suspended at a concentration of 50,000 cells per 50 µL and mixed with the alginate polymer solution in a 1:1 ratio. Fifty microliters of the polymer solution with the cell suspension were then added to the wells of a 96-well plate.

Crosslinking was achieved by adding an aqueous solution of calcium chloride ($CaCl_2$, 1% w/v) as the ionic crosslinking agent. After 10 minutes the calcium chloride solution was removed, and each well was washed whit phosphate-buffered saline (PBS) and replenished with 100 µL of DMEM to maintain cell viability.

7.5.2 Morphology evaluation

For cytoskeletal analysis, cells were fixed in 4% (w/v) paraformaldehyde for 30 min at room temperature, rinsed with DPBS, and subsequently stained with ActinGreen™ 488 ReadyProbes™ Reagent (Thermo Fisher; 2 drops/mL of medium) for 30 min. Nuclear counterstaining was performed using the nuclear dye provided in the kit. Following staining, samples were washed in PBS and maintained hydrated until imaging. For HUVECs cultured on electrospun membranes, inserts were inverted during acquisition to orient the cell layer toward the microscope light path.

Imaging was performed using a Leica Thunder confocal microscope equipped with temperature (37 °C) and CO_2 (5%) control. Acquired images were processed and analyzed using ImageJ software.

Fluorescence microscopy was used to assess the adhesion, morphology, and cytoskeletal organization of HUVECs and MDA-MB-231 cells cultured within the dual-scaffold microfluidic system. As shown in Figure 94, DAPI staining confirmed a homogeneous cell distribution across both scaffolds, with the nuclei (blue) appearing intact and uniformly dispersed. The HUVECs seeded on the aligned electrospun PLA membrane exhibited an elongated morphology with actin filaments (green) oriented along the fiber direction, indicating cytoskeletal alignment and substrate-guided organization. In contrast, MDA-MB-231 cells cultured within the alginate hydrogel under static conditions for seven days displayed a rounded morphology typical of 3D growth, with a dense actin network and preserved cell viability. These observations confirm the biocompatibility of both scaffolds and their ability to support distinct cellular architectures representative of endothelial and epithelial tumor phenotypes.

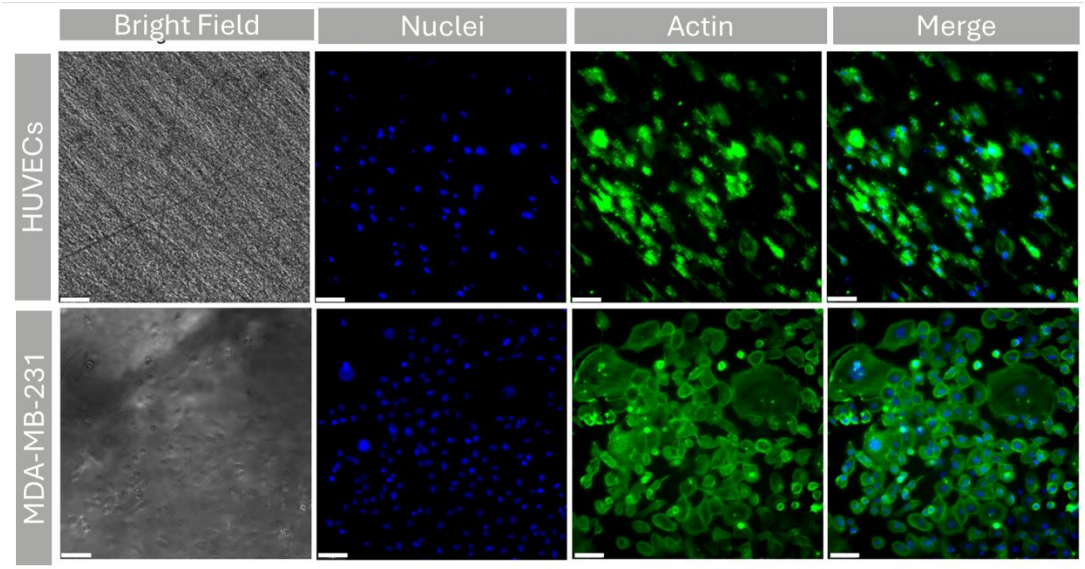

Figure 94 Fluorescence microscopy images showing HUVECs cultured on the aligned PLA electrospun membrane (top) and MDA-MB-231 cells embedded within the alginate hydrogel (bottom). Columns show bright field, DAPI-stained nuclei (blue), actin filaments (green), and merged channels. HUVECs display alignment along the fiber orientation, while MDA-MB-231 cells exhibit rounded morphology consistent with 3D culture. Scale bar: 50 µm.

7.6 Discussion and Perspectives

Overall, the results presented in this work represent a proof of concept demonstrating the feasibility of integrating multiple scaffold types within an ISO-compliant thermoplastic microfluidic platform. The system successfully supported the adhesion and viability of both endothelial and tumor cells, confirming its biocompatibility and structural stability under static culture conditions. These findings validate the design of a novel Organ-on-Chip device that combines a two-dimensional electrospun PLA (A-PLA) scaffold with a three-dimensional alginate-based hydrogel (Alg-H), thus integrating the structural advantages of both substrates into a single, versatile platform for *in vitro* modeling.

The device, fabricated from PMMA through laser micromachining and thermal bonding, ensures high precision, reproducibility, and compatibility with industrial-scale production. Its ISO-compliant architecture facilitates standardization and scalability, addressing key limitations associated with conventional PDMS-based systems. Moreover, the dual-scaffold configuration enables efficient hydrogel crosslinking and robust compartmentalization, creating physiologically relevant microenvironments suitable for co-culture applications.

While static culture experiments confirmed the stability and biocompatibility of the system, further investigations are required under dynamic perfusion conditions to better reproduce physiological stimuli such as shear stress and interstitial flow. Future work will

focus on dynamic co-cultures on-chip, combining the A-PLA and Alg-H scaffolds to develop vascularized and multi-tissue constructs. These advancements will be essential to fully exploit the potential of this platform for tissue modeling, drug testing, and translational biomedical research.

8 Conclusions and Future Perspective

This thesis presented the design, fabrication, and validation of innovative microfluidic platforms based on thermoplastic polymers (PMMA) combined with electrospun PLA scaffolds. The aim was to reproduce physiologically and pathologically relevant microenvironments *in vitro*, overcoming the intrinsic limitations of static 2D cultures and PDMS-based devices by introducing scalable, reproducible, and industry-compatible solutions. The results collectively demonstrate that both the fabrication workflow and the selected material strategies are suitable for the development of robust and reproducible microfluidic platforms.

Laser micromachining proved to be a reliable approach for channel fabrication, provided that power and scan speed were finely tuned. The accurate parameters setting could ensure reproducible cuts and engraving with minimal thermal damage, highlighting the importance of balancing to achieve well-defined microstructures.

Mechanical robustness was validated through burst pressure testing, which confirmed that bonded PMMA devices can withstand pressures significantly higher than those typically encountered in microfluidic applications. Notably, commercial connectors (ChipShop mini plugs) provided a practical alternative to screw-and-ferrule systems, offering comparable sealing performance while reducing the complexity of sterilization and assembly. This aspect is crucial in view of the future standardization and scalability of OoC technologies.

Optical analyses confirmed that the thermal bonding process preserves the transparency of PMMA, with only negligible alterations in the UV–Vis spectra, thus ensuring compatibility with real-time optical readouts in biological experiments.

The integration of electrospun PLA scaffolds into the microfluidic devices was successfully achieved without compromising their microstructural or functional properties. Although minor morphological changes (slight fibre fusing and waviness) were observed after bonding, scaffold functionality was preserved, as demonstrated by consistent fibre diameters and porosity. Mechanical tests further highlighted the role of fibre orientation, with aligned fibres providing markedly stiffer and stronger scaffolds, while random fibres exhibited more ductile behaviour. These differences emphasize the potential to tailor scaffold mechanics to specific biological applications.

Surface characterization further supported the suitability of the fabrication strategy: plasma treatment effectively increased scaffold hydrophilicity, although partial loss of wettability was observed after bonding due to polymer chain rearrangement. FTIR/ATR and DSC analyses converged in demonstrating that the integration process promoted an increase in PLA crystallinity, without significantly altering the molecular architecture of the polymer. Such changes are consistent with the combined effects of thermal exposure and ethanol treatment during bonding.

Taken together, these results validate the use of PMMA as a versatile thermoplastic substrate for OoC applications, while confirming that electrospun PLA scaffolds can be seamlessly integrated without losing their structural or functional attributes. The optimization of fabrication parameters, sealing strategies, and scaffold properties lays a solid foundation for the subsequent biological validation of the devices.

In the **Liver-on-Chip**, dynamic perfusion of tumor-derived extracellular vesicles induced a mesenchymal-like phenotype in hepatocytes, recapitulating key events in the formation of pre-metastatic niches. This confirmed the relevance of the device as a platform to investigate tumor–organ cross-talk. Within this thesis, the Liver-on-Chip (LoC) served as a proof-of-concept that thermoplastic microfabrication (PMMA) combined with electrospun PLA scaffolds can deliver a robust, biomimetic and operationally simple platform for studying tumour–liver crosstalk under physiologically relevant, chronic exposure. The dual-chamber architecture enabled diffusion-dominated delivery of colorectal-cancer–derived extracellular vesicles across a scaffold that acted both as ECM-like substrate and semi-permeable barrier, while laser-cut PMMA provided optical clarity, low drug/EV absorption, and reproducible fabrication. Functionally, hepatocytes maintained adhesion and viability under flow, and—consistent with prior proteomic evidence—displayed differentiation features; chronic EV perfusion elicited mesenchymal marker induction, recapitulating early events of pre-metastatic niche conditioning. From an engineering standpoint, the platform met key reliability metrics (pressure tolerance, leakage-free sealing with commercial connectors, preserved transparency after bonding) and was built through a workflow compatible with standardization and scale-up.

Limitations (use of an immortalized line and absence of non-parenchymal liver cells) delineate clear next steps: inclusion of primary/iPSC-derived hepatocytes and stromal/immune compartments, integration of in-line sensors, and coupling with other organ

chips for PK/PD studies. Overall, the LoC advances the case for scaffold-integrated, thermoplastic OoCs as practical, reproducible tools that bridge static 2D assays and animal models, and it establishes a transferable blueprint for modelling chronic intercellular signalling in cancer progression.

The **Breast Cancer Tumor-on-Chip** successfully reproduced the interaction between breast cancer cells and stromal fibroblasts, highlighting the protective role of the tumor microenvironment in drug resistance. The differential response to treatments with olaparib and dinaciclib mirrored *in vivo* findings, supporting the potential of the system as a preclinical tool for drug screening and therapy evaluation. Within this thesis, the Tumor-on-Chip (ToC) demonstrated that a thermoplastic, scaffold-integrated microfluidic platform can recapitulate essential tumour–stroma dynamics while remaining practical, reproducible, and compatible with rapid prototyping. Laser-patterned PMMA provided optical clarity, low small-molecule absorption, and robust sealing with commercial connectors; the integrated electrospun PLA scaffold supplied an ECM-like interface that preserved structure after bonding and supported adhesion, proliferation, and crosstalk of breast-cancer cells (HCC-1937) with CAFs under static and perfused conditions. Functionally, the device reproduced *in vivo*–consistent pharmacological behavior: combined olaparib–dinaciclib treatment reduced tumour cell viability, while CAF co-culture conferred protection, mirroring stromal-mediated resistance observed in xenograft studies. Dynamic perfusion improved baseline viability and exposure control relative to static inserts, underscoring the importance of flow for physiologically relevant drug testing.

From an engineering standpoint, the shift to standardized, commercial connectors simplified aseptic handling and assembly without sacrificing pressure tolerance or transparency, strengthening the platform's translational readiness. Limitations—use of a single BC line and stromal subset, absence of immune components, and lack of longitudinal functional readouts—define clear next steps: expansion to patient-derived cells, inclusion of immune and endothelial compartments, quantitative secretome/omics endpoints, and coupling to multi-organ circuits for PK/PD interrogation. Overall, the ToC advances scaffold-integrated thermoplastic OoCs as credible preclinical models that bridge the gap between 2D assays, animal studies, and clinically relevant drug-response prediction, supporting more ethical, efficient, and personalized oncology research.

The **Brain-on-Chip** demonstrated the feasibility of co-culturing neuronal and glial cells within a controlled microenvironment, enabling both the assessment of structural markers and the selective uptake of neuroactive compounds. This approach opens promising perspectives for modeling neurodegenerative disorders and for testing neuropharmacological agents. The Brain-on-Chip (BoC) developed in this thesis shows that a thermoplastic, scaffold-integrated microfluidic platform can interrogate cell-type selectivity in the CNS with high experimental control and practical usability. Laser-patterned PMMA provided low small-molecule absorption, optical clarity, and robust, leak-free assembly; the integrated electrospun PLA scaffold—tested in both aligned and random architectures—offered an ECM-like interface that sustained long-term cytocompatibility for neuronal (SH-SY5Y) and microglial (BV2) cultures while guiding morphology in a topology-dependent manner. CFD-informed operation achieved brain-relevant surface velocities under ultra-low shear, preserving adhesion during perfusion and enabling a controlled transition from fluidic isolation (for independent seeding) to shared perfusion (for comparative stimulation).

Functionally, the platform reproduced cell-type selective uptake using myelin-derived nanovesicles (MyVes) from the Picone/IRIB-CNR group: under identical flow and exposure, fluorescence localized exclusively to the microglial compartment, validating the device's ability to resolve selective interactions in a co-culture exposed to a common milieu. Marker analysis (β-tubulin III, MAP2, IBA1) confirmed preserved cytoskeletal organization across scaffold types, supporting the engineering claim that the bonding and assembly workflow does not impair neuronal or microglial structural integrity.

Current limitations define clear avenues for expansion: the use of immortalized lines (BV2, SH-SY5Y), a two-cell architecture lacking astrocytes and a vascular/Blood Brain Barrier (BBB) interface, short exposure windows, and qualitative readouts of uptake rather than quantitative kinetic/transport measurements. Future work should incorporate iPSC-derived human neurons and microglia, add an endothelial–astrocyte BBB module, extend to multiplexed readouts (live imaging, TEER, secretomics), and generalize beyond MyVes to targeted biologics and nanoparticles. Coupling the BoC with upstream BBB-on-chip or downstream liver-on-chip units would also enable PK/PD-aware selectivity studies. Altogether, this BoC demonstrates that scaffold-integrated, thermoplastic OoCs can deliver rigorous, reproducible assessments of cell-type selectivity in neural co-cultures, advancing more predictive, reductionist alternatives to animal testing and supporting safer, more effective CNS drug development.

In the final part of this work, a new microfluidic platform compliant with the ISO 22916:2022 standard was developed, representing an important step toward the standardization and scalability of Organ-on-Chip technologies. The device was conceived to integrate within a single thermoplastic architecture two complementary culture environments: an aligned electrospun PLA membrane, designed to reproduce the anisotropic features of barrier tissues and support endothelial organization, and an ionically *in-situ* crosslinked alginate hydrogel, which mimics the three-dimensional structure and mechanical properties of stromal or parenchymal tissues.

Morphological and functional analyses demonstrated that the hydrogel remained stably confined within its compartment, maintaining adhesion and structural integrity for up to 72 hours without obstructing the lateral microchannels responsible for nutrient exchange. This confirmed the effectiveness of the design in preventing leakage and ensuring proper fluidic connectivity between compartments. The topography of the aligned PLA scaffold, characterized by AFM, promoted directional alignment of HUVECs, while the alginate matrix supported the viability and morphology of MDA-MB-231 cells cultured under static conditions, thus validating the biocompatibility and functionality of both scaffolds within the device.

Although the present study represents a preliminary proof of concept, the results highlight the feasibility of integrating multiple scaffold types within a standardized thermoplastic microfluidic system. The ISO-conformant layout and geometrical precision of the device ensure reproducibility and interoperability with existing microfluidic platforms, bridging the gap between academic prototyping and scalable production. Future work will focus on dynamic perfusion experiments to reproduce physiological flow conditions such as shear stress and interstitial fluid transport, as well as on the development of more complex co-culture models that include vascular–tumour or vascular–stromal interfaces.

Taken together, these results validate the use of PMMA as a versatile thermoplastic substrate for OoC applications, while confirming that electrospun PLA scaffolds can be seamlessly integrated without losing their structural or functional attributes. The optimization of fabrication parameters, sealing strategies, and scaffold properties lays a solid foundation for the subsequent biological validation of the devices.

The future directions of this doctoral research are deeply rooted in the translational ambition that guided its development from the outset — the creation of reliable,

standardized, and physiologically relevant Organ-on-Chip (OoC) systems that can bridge the gap between academic innovation and real-world biomedical applications.

During the second year of this PhD program, the promising preliminary results obtained from the thermoplastic scaffold-integrated platforms laid the foundation for the creation of *BioRESystems s.r.l.s.,* an academic spin-off of the University of Palermo. This company represents the natural evolution of the research work presented in this thesis, translating laboratory prototypes into scalable, regulatory-compliant, and commercially viable products. BioRESystems operates at the interface of bioengineering, life sciences, and clinical translation, aiming to deliver modular OoC technologies tailored for both academic research and hospital-based personalized medicine. The mission of BioRESystems reflects the broader objective of this doctoral project: transforming microfluidic systems from experimental tools into reproducible biomedical devices ready for preclinical and clinical use.

Looking forward, one of the main technological advancements will concern the integration of electrochemical sensing modules directly within the OoC architecture. The incorporation of in-line, real-time biosensors capable of monitoring key physicochemical parameters—such as oxygen concentration, pH, redox balance, and oxidative stress—will open unprecedented possibilities for continuous assessment of cellular health, metabolism, and microenvironmental dynamics. Electrochemical sensors, due to their miniaturization potential, sensitivity, and compatibility with thermoplastic substrates, represent an ideal analytical interface for microphysiological systems. Their integration will enable closed-loop feedback between cell responses and environmental stimuli, laying the groundwork for autonomous and adaptive tissue models. This technological evolution will transform static observation platforms into dynamic bio-intelligent systems, capable of providing quantitative, high-resolution data for drug testing, toxicology, and systems biology.

Building upon these foundations, future work will extend toward the development of multi-organ systems, where interconnected microfluidic modules reproduce physiological communication between different tissues within a shared circulatory circuit. These interconnected “body-on-chip” or “human-on-chip” platforms represent the ultimate evolution of microphysiological systems, capable of capturing systemic responses to drugs, nanoparticles, and environmental factors. By linking organ-specific compartments via controlled microfluidic flow and sensor feedback, such systems will provide a powerful tool for predictive pharmacokinetic and pharmacodynamic (PK/PD) studies, disease modeling, and precision medicine.

The long-term vision is therefore to create standardized, interoperable, and sensor-integrated multiorgan platforms that not only replace animal models but also offer superior physiological relevance, scalability, and ethical sustainability. These devices will enable quantitative, data-rich experimentation, bringing together engineering, biology, and digital analytics in a truly interdisciplinary framework.

In summary, the outcomes of this PhD work have paved the way for a paradigm shift in Organ-on-Chip research—from academic prototypes to translational technologies ready for industrial and clinical deployment. Through the continued efforts of BioRESystems and the integration of real-time sensing, modular architecture, and advanced scaffold engineering, the vision of standardized human-on-chip systems is becoming increasingly tangible. These innovations hold the potential to standardize preclinical testing, accelerate drug discovery, and redefine the experimental landscape of modern biomedicine.

Research Activities

The following section summarizes the scientific and academic activities carried out during my PhD within the Doctoral Program in *Biomedicine, Neurosciences and Advanced Diagnostics (BiND)* at the University of Palermo.

My work was mainly focused on the development of microfluidic *Organ-on-Chip* (OoC) platforms as advanced *in vitro* models to investigate physiological and pathological mechanisms in a controlled microenvironment.

This section provides an overview of the research outcomes achieved during the doctoral period, including peer-reviewed publications, national and international conference presentations, participation in funded research projects, and collaboration within multidisciplinary teams.

Additionally, it outlines my contributions to teaching activities, supervision of master thesis, patent applications, and international training experiences, reflecting the highly integrative nature of my research at the interface between engineering, biology, and diagnostic innovation.

Published Articles

E. Capuana et al., *Impact of Fiber Orientation in Electrospun PLA Scaffolds on Fluid Dynamics in a Custom Microfluidic Device*, Advanced Healthcare Materials Open source preview, 2025, 14(25), 2500378

M. Testa et al., *Rapid prototyping of a multicompartment liver-on-chip for dynamic administration of tumour derived vesicles within an electrospun scaffold*, Lab on A Chip Open source preview, 2025, 25(18), pp. 4717–4734

Di Stefano, A.B. et al*., Effect of nanocomposite chitosan/hydroxyapatite pH-induced hydrogels on the osteogenic differentiation of spheroids from adipose stem cells*, International Journal of Biological Macromolecules Open source preview, 2025, 299, 140213

M. Testa et al., *A Novel Tumor on Chip Mimicking the Breast Cancer Microenvironment for Dynamic Drug Screening*, International Journal of Molecular Sciences Open source preview, 2025, 26(3), 1028

M. Testa et al., Experimental Validation of an Organ-on-Chip for Mechanical Stimulation of Cell Cultures, bioRxiv, 2023, https://doi.org/10.1101/2023.12.15.571835

M. Testa et al., Rapid prototyping of a microfluidic platform for nasal mucosa models, Convegno Nazionale di Bioingegneria, 2023

P. Picone et al., *Mitochondria embedded in degalactosylated xyloglucan hydrogels to improve mitochondrial transplantation*, Carbohydrate Polymer Technologies and Applications, 2024, 8, 100543, https://doi.org/10.1016/j.carpta.2024.100543

Conferences

M. Testa et al, *ISO-Compliant multiscaffold microfluidic platform for scalable Organ-on-Chip applications,* GNB 2025 IX National Congress of Bioengineering, Palermo, Italy, 16 - 18 June 2025

F. Lopresti, M. Testa et al., Mechanical *Stimulation of Cell Cultures in a Rigid Organ-on-Chip Platform.* Tissue Engineering and Regenerative Medicine (TERMIS) in Freiburg Germany, 19-23 May 2025

M. Testa et al, *ISO-Compliant microfluidic device for multilayer Alg-H/A-PLA Co-Culture with in-situ cell-laden gelation*, Tissue Engineering and Regenerative Medicine International Society, TERMIS-EU Congress 2025, Freiburg, (Germany) 19-23 May 2025

M. Testa et al, *Rapid Prototyping of ISO-Compliant Scaffold-Integrated Microfluidic Devices: Towards Animal-Free and Scalable Preclinical Models,* Poster Presentation**,** Bragg Exchange 2025, Esther Simpson Building, University of Leeds (UK).

M. Testa et al*, Polylactic acid electrospun membrane as a proof of concept for intestinal barrier reconstruction.* 11th Conference of the Modification, Degradation, Stabilization of Polymers Society (MoDeSt 2024) - Palermo, Italy, September 1-4, 2024

M. Testa et al, *Thermoplastic Liver-on-Chip integrating an electrospun membrane for dynamic administration of cancer-derived vesicles*. Poster Presentation European Organ-on-Chip Society, held in Milan, Italy, from July 3–5, 2024

M. Testa et al., *Rapid prototyping of a microfluidic platform for nasal mucosa models*, GNB VIII National Congress od Bioengineering Padova, Italy,21 - 23 June 2023.

Conference Contributions (Co-author / Collaborator)

S. Tornabene, G. Musotto, M. Testa, S. Di Leonardo, G. Burriesci, F. Lopresti, V. La Carrubba *An innovative dual stimulation organ-on-a-chip, validated through experimental tests and Fluid Solid Interaction Analysis.* Ri.MED Symposium 2025 "Engineering Biology for Next-Gen Medicine" 17-17 October 2025, Palermo Italy

Tornabene, S., **Carmagnola, I.**, **Spedicati, M.**, **Di Marco, C.**, **Testa, M.**, **Lopresti, F.**, **La Carrubba, V.**
Sustainable Organ-on-Chip: A PLA-Based Microfluidic Platform for Preclinical Testing. ESB 34th Annual Conference of the European Society for Biomaterials,September 7-11, 2025 in Turin, Italy.

Tornabene, S., **Testa, M.**, **Di Leonardo, S.**, **La Carrubba, V.**, **Burriesci, G.**, **Lopresti, F.**
Fabrication and Validation of a Dual-Stimulation Organ-on-Chip.
IX Congress of the National Group of Bioengineering (GNB), Palermo, Italy, June 16–18, 2025.

C. Di Marco, N. Torras Andrés, M. Testa, D. Bartolomé Català, F. Lopresti, V. La Carrubba and E. Martínez Fraiz
Customized PMMA microfluidic device for in situ hydrogel crosslinking. *IX Congress of the National Group of Bioengineering (GNB)*, Palermo, Italy, June 16–18, 2025.

N. Calabriso, F. Lopresti, S. Tornabene, C. Di Marco, M. Testa, I. Carmagnola, M. Spedicati, M. Massaro, S. Quarta, L. Siculella, L. Draghi, S. Farè, V. La Carrubba and M.A. Carlucci
Polylactic acid scaffolds improve osteogenesis of mesenchymal stem cell cultured with human vascular endothelial cells. IX Congress of the National Group of Bioengineering (GNB), Palermo, Italy, June 16–18, 2025.

La Carrubba, V., **Di Marco, C.**, **Testa, M.**, **Tornabene, S.**, **Di Leonardo, S.**, **Burriesci, G.**, **Lopresti, F.**
Development and Characterization of a Blood-Mimicking Fluid for Hemodynamic Research.
IX Congress of the National Group of Bioengineering (GNB), Palermo, Italy, June 16–18, 2025. *(Co-author contribution)*

La Rosa, M., **Girgenti, A.**, **Di Marco, C.**, **Testa, M.**, **Palumbo, L.**, **Picone, P.**, **Nuzzo, D.**, **Lopresti, F.**, **La Carrubba, V.**
Effect of Poly(Lactic Acid) Fiber Orientation on Neural Cell Migration and Spheroid-like Polarization.
IX Congress of the National Group of Bioengineering (GNB), Palermo, Italy, June 16–18, 2025.

Tornabene, S., **Musotto, G.**, **Testa, M.**, **Di Leonardo, S.**, **Burriesci, G.**, **Lopresti, F.**, **La Carrubba, V.**
An Innovative Dual-Stimulation Organ-on-Chip Validated Through Experimental Tests and Fluid–Solid Interaction Analysis.
IX Congress of the National Group of Bioengineering (GNB), Palermo, Italy, June 16–18, 2025.

C. Curiale, M. Testa, C.Di Marco, G.Serio, C. Gentile, V. La Carrubba and F.Lopresti *Design and assessment of an ISO-compliant Gut-on-Chip device with electrospun scaffolds through rapid prototyping method IX Congress of the National Group of Bioengineering (GNB)*, Palermo, Italy, June 16–18, 2025

C. Curiale, M. Testa, C. Di Marco, G. Serio, C. Gentile, V. La Carrubba, F. Lopresti
Development and Evaluation of an ISO-Compliant Gut-on-Chip Device with Electrospun Membranes Using Rapid Prototyping Techniques. Tissue Engineering and Regenerative Medicine (TERMIS) in Freiburg Germany, 19-23 May 2025

E. Capuana, **C. Di Marco, C. Curiale, M. Testa, F. Lopresti, V. La Carrubba**
Development of a vascularized Tumor-on-Chip platform for dynamic simulation of the tumor microenvironment. Tissue Engineering and Regenerative Medicine (TERMIS) in Freiburg Germany, 19-23 May 2025 (Oral Presentation)

C. Di Marco, F. Lopresti, A. Carrista, M. Testa, S. Burgio, P. Bongiorno, F. Bucchieri, V. La Carrubba
Fabrication and characterization of electrospun PLA membranes for targeted release of THC and CBD in treating inflammatory respiratory mucosa. Tissue Engineering and Regenerative Medicine (TERMIS) in Freiburg Germany, 19-23 May 2025

M. La Rosa, A. Girgenti, C. Di Marco, M. Testa, P. Picone, D. Nuzzo, Palumbo, F. Lopresti, V. La Carrubba

Alignment of electrospun poly lactic acid nanofibers increase neural cell migration and polarization into 3D cell clusters. Regenerative Medicine (TERMIS) in Freiburg Germany, 19-23 May 2025

Integrating Microfluidics and Electrospun Scaffold in Breast Cancer Tumor-on-a-Chip (ToC) Models: Design, Optimization, and Computational Insights.
7th TERMIS World Congress, Seattle, Washington (USA), June 25-28, 2024

F. Lopresti, M. Testa, M. Gaggianesi, C. D'Accardo, G. Porcelli, A. Turdo, M. Todaro, G. Stassi, V. La Carrubba

Rapid prototyping of a compartmentalized tumor-on-chip device for anticancer treatments. EuroOoCs 2024 Milan Italy 3-5 July 2024

C. Di Marco, M. Trapani, M. Testa, B. Di Stefano, V. La Carrubba, F. Lopresti

Enhanced Mechanical and Rheological Properties of Chitosan-Based Hydrogels with Hydroxyapatite for Bone Tissue Engineering.
11th MoDeSt Conference, Palermo, Italy – September 1–4, 2024.

Active Projects

Member of the research unit at the University of Palermo (Project Leader), in the **PRIN 2022 Research Program.** Project Title: Green MIcrofluiDic PLAtform for advanced tissue on a Chip culturEs (**Green MID-PLACE**)

Didactic

Teaching (10 hours) of course "BIOMED – Tecnico Superiore per la produzione, manutenzione e assistenza di apparecchi e dispositivi diagnostici, terapeutici e riabilitativi" of Fondazione ITS Nuove Tecnologie della Vita Alessandro Volta.

Correlator of Master Thesis

“Sviluppo di un Organ-on-Chip multicompartimentato per lo screening farmacologico avanzato”

Student: Zappacosta Aurelio Savio University of Palermo, Academic Year 2023/2024.
Supervisor: V. La Carrubba, P. Picone, M. La Rosa, M. Testa

“Sviluppo di una piattaforma microfluidica per lo studio dei meccanismi di metastasi”

Student: Sidoti Lina Ilaria University of Palermo, Academic Year 2023/2024.

Supervisors: F. Lopresti, V. La Carrubba, C. Curiale, M. Testa, A. Filippone

“Sviluppo e caratterizzazione di un dispositivo microfluidico del tipo Gut-on-Chip”

Student: Placa Elia University of Palermo, Academic Year 2023/2024.

Supervisor: V. La Carrubba, F. Lopresti C. Gentile, C. Curiale, M. Testa

“Sviluppo di uno scaffold multistrato per la bio-fabbricazione di un modello cutaneo su organ-on-chip”

Student: Andrea Ciacciofera University of Palermo, Academic Year 2023/2024.

Supervisors: Prof. Francesco Lo Presti, Prof. Vincenzo La Carrubba, Prof. Virginia Pensabene, Dott.ssa Maria Testa

“Sviluppo di uno scaffold elettrofilato per la bio-fabbricazione di un modello tumorale endotelializzato su organ-on-chip”

Student: Federica Bellanca University of Palermo, Academic Year 2023/2024.

Supervisors: Prof. Francesco Lopresti, Prof. Vincenzo La Carrubba, Prof. Virginia Pensabene,Dott.ssa Maria Testa

“Validazione sperimentale e Analisi delle Interazioni Fluido Struttura di un dispositivo microfluidico per la stimolazione meccanica di colture cellulari”

Student: Federica Castiglia University of Palermo, Academic Year 2023/2024.

Supervisors: Prof. Francesco Lopresti, Prof. Vincenzo La Carrubba, Prof. Gaetano Burriesci, Ing. Maria Testa, Ing. Salvatore Tornabene

“Progettazione, fabbricazione e validazione di un dispositivo microfluidico ecosostenibile per la realizzazione di un modello di Organ-on-Chip”

Student: Davide Macaluso University of Palermo, Academic Year 2023/2024.

Spuervisors: Prof. Vincenzo La Carrubba, Prof. Francesco Lopresti, Dott.ssa Maria Testa, Ing. Salvatore Tornabene

“Progettazione, fabbricazione e validazione di un dispositivo Organ-on-Chip ad interfaccia aria liquido”

Student Gaja Giglione ,University of Palermo, Academic Year 2023/2024.
Supervisors: Prof. Francesco Lopresti, Ing. Maria Testa, Prof. Fabio Bucchieri

“Liver-on-Chip termoplastico equipaggiato con una membrana elettrofilata per la somministrazione dinamica di vescicole derivate da cellule tumorali.”

Student: Federico De Simone, University of Palermo, Academic Year 2022/2023.
Supervisors: Prof. Francesco Lopresti, Prof. Vincenzo La Carrubba, Prof.ssa Simona Fontana, Dott.ssa Maria Testa

“Development of a dual chamber culture microfluidic chip to evaluate the effect of cancer cells on healthy tissues.”

Student: Giulia Santaromita, University of Palermo, Academic Year, 2022/2023.
Supervisors: Prof. Vincenzo La Carrubba, Prof. Francesco Lopresti, Dott.ssa E.Capuana, Dott.ssa Maria Testa.

“Optimization of an Air-Liquid Interface Microfluidic Platform for the Development of Nasal Mucosa.”

Student: Irene Ignazzitto, University of Palermo, Academic Year 2022/2023.
Supervisors: Prof. Francesco Lopresti, Prof. Vincenzo La Carrubba, Dott.ssa Maria Testa.

“Validazione sperimentale e computazionale di un Organ-on-Chip per la stimolazione meccanica di colture cellulari.”

Student: Salvatore Tornabene, University of Palermo, Academic Year 2022/2023.
Supervisors: Prof. Francesco Lopresti, Prof. Vincenzo La Carrubba, Prof. Gaetano Burriesci, Dott.ssa Maria Testa.

“Modello microfluidico in vitro di tessuto intestinale.”

Student: Nicolò Paglino, University of Palermo, Academic Year 2022/2023,
Supervisors: Prof. Francesco Lopresti, Prof. Vincenzo La Carrubba, Dott.ssa Maria Testa, Prof.ssa Carla Gentile.

Patent Pending

"Metodo, dispositivo e sistema combinato per la co-coltura cellulare in ambienti bidimensionali e tridimensionali" – M. Testa, F. Lopresti, V. La Carrubba, F. Bucchieri, C. Di Marco.

"Metodo, dispositivo e sistema per l'emulazione di stress microfluidici indotti sulle vie aeree durante la respirazione". M. Testa, F. Lopresti, V. La Carrubba, S. Burgio, O. M. Manna.

Academic Spin-Off

*Chief Executive Officer (CEO) -**BioRESystems s.r.l.s.***

Award

Premio America Innovazione 2025, promoted by the *Italy–USA Foundation* and presented at the *Italian Parliament*, awarded in recognition of outstanding entrepreneurial talent among founders of Italian startups and innovative SMEs.

Second Prize – Premio Cambiamenti 2024, *VIII Edition*, organized by *Confederazione Nazionale dell'Artigianato e della Piccola e Media Impresa (CNA)* –National Competition, Rome.
Project: *BioRESystems – Innovative Entrepreneurial Project*

Special Mention – UniCredit StartLab, *Premio Cambiamenti 2024*, *VIII Edition*, organized by *CNA* – National Competition, Rome.
Project: *BioRESystems – Innovative Entrepreneurial Project*

Special Mention – SEARCHON "We Make Future", *National Award for Innovation (PNI)*, 2023 Edition
Category: Life Sciences – MedTech
Project: *Environmental Biosensor System: Real-Time Analysis of Pollutants on Respiratory Mucosa (BioRESystem)*

Courses and Seminars Attended

“An Introduction to the Horizon Europe Framework Program with Good Practices for the Preparation of Research Proposals”*Prof. G. Micale*

“Epigenetics and Cancer: State of the Art and Potential of HDAC Inhibitors in Targeted Therapy” *Prof. Sonia Emanuele*

“Extracellular Vesicles from Plants: From Basic Research to Clinical Applications”*Dr. Stefania Raimondo, Ph.D.*

“Advances in Techniques to Monitor Neuronal Activity During Animal Behavior”
Short Course

“Mango Peel and Seed Extracts Reduce Adipogenesis and Counteract Palmitic Acid-Induced Lipotoxicity in 3T3-L1 Adipocytes”
Seminar Presentation

“ENABLING NEW ALTERNATIVES TO ANIMAL MODELS”
Workshop Presentation

Exchange period

Multiorgan Development of Breast-Bone Organ on Chip device, Skin on Chip for investigating Thermal chock in Raynaud’s syndrome – Leeds, West Yorkshire, England– from 01/10/2024 to 28/03/2025.

Bibliography

[1] R. Kalot, R. Mhanna, R. Talhouk, Organ-on-a-chip platforms as novel advancements for studying heterogeneity, metastasis, and drug efficacy in breast cancer, Pharmacol. Ther. 237 (2022). https://doi.org/10.1016/j.pharmthera.2022.108156.

[2] L.A. Low, C. Mummery, B.R. Berridge, C.P. Austin, D.A. Tagle, Organs-on-chips: into the next decade, Nat. Rev. Drug Discov. 20 (2021) 345–361. https://doi.org/10.1038/s41573-020-0079-3.

[3] M. Hay, D.W. Thomas, J.L. Craighead, C. Economides, J. Rosenthal, Clinical development success rates for investigational drugs, Nat. Biotechnol. 32 (2014) 40–51. https://doi.org/10.1038/nbt.2786.

[4] J.A. DiMasi, H.G. Grabowski, R.W. Hansen, Innovation in the pharmaceutical industry: New estimates of R&D costs, J. Health Econ. 47 (2016) 20–33. https://doi.org/10.1016/j.jhealeco.2016.01.012.

[5] K. Smietana, M. Siatkowski, M. Møller, Trends in clinical success rates, Nat. Rev. Drug Discov. 15 (2016) 379–380. https://doi.org/10.1038/nrd.2016.85.

[6] K. Duval, H. Grover, L.H. Han, Y. Mou, A.F. Pegoraro, J. Fredberg, Z. Chen, Modeling physiological events in 2D vs. 3D cell culture, Physiology 32 (2017) 266–277. https://doi.org/10.1152/physiol.00036.2016.

[7] J.A. DiMasi, M.I. Florez, S. Stergiopoulos, Y. Peña, Z. Smith, M. Wilkinson, K.A. Getz, Development Times and Approval Success Rates for Drugs to Treat Infectious Diseases, Clin. Pharmacol. Ther. 107 (2020) 324–332. https://doi.org/10.1002/cpt.1627.

[8] M. Abdelsayed, E.J. Kort, S. Jovinge, M. Mercola, Repurposing drugs to treat cardiovascular disease in the era of precision medicine, Nat. Rev. Cardiol. 19 (2022) 751–764. https://doi.org/10.1038/s41569-022-00717-6.

[9] P. Mukherjee, S. Roy, D. Ghosh, S.K. Nandi, Role of animal models in biomedical research: a review, Lab. Anim. Res. 38 (2022) 18. https://doi.org/10.1186/s42826-022-00128-1.

[10] A. Kamatar, G. Gunay, H. Acar, Natural and Synthetic Biomaterials for Engineering Multicellular Tumor Spheroids, Polymers 12 (2020) 2506. https://doi.org/10.3390/polym12112506.

[11] R. Edmondson, J.J. Broglie, A.F. Adcock, L. Yang, Three-Dimensional Cell Culture Systems and Their Applications in Drug Discovery and Cell-Based Biosensors, ASSAY Drug Dev. Technol. 12 (2014) 207–218. https://doi.org/10.1089/adt.2014.573.

[12] S.-Y. Lee, I.-S. Koo, H.J. Hwang, D.W. Lee, In Vitro three-dimensional (3D) cell culture tools for spheroid and organoid models, SLAS Discov. 28 (2023) 119–137. https://doi.org/10.1016/j.slasd.2023.03.006.

[13] S.A. Langhans, Three-Dimensional in Vitro Cell Culture Models in Drug Discovery and Drug Repositioning, Front. Pharmacol. 9 (2018) 6. https://doi.org/10.3389/fphar.2018.00006.

[14] R. Edmondson, J.J. Broglie, A.F. Adcock, L. Yang, Three-Dimensional Cell Culture Systems and Their Applications in Drug Discovery and Cell-Based Biosensors, ASSAY Drug Dev. Technol. 12 (2014) 207–218. https://doi.org/10.1089/adt.2014.573.

[15] N. Matsuda, T. Shimizu, M. Yamato, T. Okano, Tissue Engineering Based on Cell Sheet Technology, Adv. Mater. 19 (2007) 3089–3099. https://doi.org/10.1002/adma.200701978.
[16] A. Ghanemi, Cell cultures in drug development: Applications, challenges and limitations, Saudi Pharm. J. 23 (2015) 453–454. https://doi.org/10.1016/j.jsps.2014.04.002.
[17] L.A. Low, C. Mummery, B.R. Berridge, C.P. Austin, D.A. Tagle, Organs-on-chips: into the next decade, Nat. Rev. Drug Discov. 20 (2021) 345–361.
[18] D. Huh, G.A. Hamilton, D.E. Ingber, From 3D cell culture to organs-on-chips, Trends Cell Biol. 21 (2011) 745–754. https://doi.org/10.1016/j.tcb.2011.09.005.
[19] S.N. Bhatia, D.E. Ingber, Microfluidic organs-on-chips, Nat. Biotechnol. 32 (2014) 760–772. https://doi.org/10.1038/nbt.2989.
[20] G.M. Whitesides, The origins and the future of microfluidics., Nature 442 (2006) 368–373. https://doi.org/10.1038/nature05058.
[21] S. Ishida, Organs-on-a-chip: Current applications and consideration points for in vitro ADME-Tox studies., Drug Metab. Pharmacokinet. 33 (2018) 49–54. https://doi.org/10.1016/j.dmpk.2018.01.003.
[22] J. Rogal, K. Schlünder, P. Loskill, Developer's Guide to an Organ-on-Chip Model, ACS Biomater. Sci. Eng. 8 (2022) 4643–4647. https://doi.org/10.1021/acsbiomaterials.1c01536.
[23] D. Huh, B.D. Matthews, A. Mammoto, M. Montoya-Zavala, H.Y. Hsin, D.E. Ingber, Reconstituting Organ-Level Lung Functions on a Chip, Science 328 (2010) 1662–1668. https://doi.org/10.1126/science.1188302.
[24] J.A. Terrell, C.G. Jones, G.K.M. Kabandana, C. Chen, From cells-on-a-chip to organs-on-a-chip: Scaffolding materials for 3D cell culture in microfluidics, J. Mater. Chem. B 8 (2020) 6667–6685. https://doi.org/10.1039/d0tb00718h.
[25] R.C. Dutta, A.K. Dutta, Cell-interactive 3D-scaffold; advances and applications., Biotechnol. Adv. 27 (2009) 334–339. https://doi.org/10.1016/j.biotechadv.2009.02.002.
[26] N. Gupta, J.R. Liu, B. Patel, D.E. Solomon, B. Vaidya, V. Gupta, Microfluidics-based 3D cell culture models: Utility in novel drug discovery and delivery research., Bioeng. Transl. Med. 1 (2016) 63–81. https://doi.org/10.1002/btm2.10013.
[27] Y. You, C. Zhang, Z. Guo, F. Xu, D. Sun, J. Xia, S. Chen, Lung-on-a-chip composed of styrene-butadiene-styrene nano-fiber/porous PDMS composite membranes with cyclic triaxial stimulation, Microfluid. Nanofluidics 28 (2024). https://doi.org/10.1007/s10404-024-02739-7.
[28] L. Zheng, H. Dong, W. Zhao, X. Zhang, X. Duan, H. Zhang, S. Liu, G. Sui, An Air-Liquid Interface Organ-Level Lung Microfluidics Platform for Analysis on Molecular Mechanisms of Cytotoxicity Induced by Cancer-Causing Fine Particles, ACS Sens. 4 (2019) 907-917-907–917. https://doi.org/10.1021/acssensors.8b01672.
[29] A. Sengupta, N. Roldan, M. Kiener, L. Froment, G. Raggi, T. Imler, L. de Maddalena, A. Rapet, T. May, P. Carius, N. Schneider-Daum, C.-M. Lehr, M. Kruithof-de Julio, T. Geiser, T.M. Marti, J.D. Stucki, N. Hobi, O.T. Guenat, A New Immortalized Human Alveolar Epithelial Cell Model to Study Lung Injury and Toxicity on a Breathing Lung-On-Chip System, Front. Toxicol. 4 (2022). https://doi.org/10.3389/ftox.2022.840606.
[30] R. Plebani, R. Potla, M. Soong, H. Bai, Z. Izadifar, A. Jiang, R.N. Travis, C. Belgur, A. Dinis, M.J. Cartwright, R. Prantil-Baun, P. Jolly, S.E. Gilpin, M. Romano, D.E. Ingber, Modeling pulmonary cystic fibrosis in a human lung airway-on-a-chip, J. Cyst. Fibros. 21 (2022) 606-615-606–615. https://doi.org/10.1016/j.jcf.2021.10.004.
[31] T. Messelmani, A. Le Goff, Z. Souguir, V. Maes, M. Roudaut, E. Vandenhaute, N. Maubon, C. Legallais, E. Leclerc, R. Jellali, Development of Liver-on-Chip Integrating

a Hydroscaffold Mimicking the Liver's Extracellular Matrix, Bioengineering 9 (2022). https://doi.org/10.3390/bioengineering9090443.
[32] P. Kanabekova, A. Kadyrova, G. Kulsharova, Microfluidic Organ-on-a-Chip Devices for Liver Disease Modeling In Vitro, Micromachines 13 (2022). https://doi.org/10.3390/mi13030428.
[33] V. Paloschi, M. Sabater-Lleal, H. Middelkamp, A. Vivas, S. Johansson, A. Van Der Meer, M. Tenje, L. Maegdefessel, Organ-on-a-chip technology: A novel approach to investigate cardiovascular diseases, Cardiovasc. Res. 117 (2021) 2742–2754. https://doi.org/10.1093/cvr/cvab088.
[34] X. Mou, J. Shah, Y. Roye, C. Du, S. Musah, An ultrathin membrane mediates tissue-specific morphogenesis and barrier function in a human kidney chip, Sci. Adv. 10 (2024) eadn2689–eadn2689.
[35] C.A.M. Fois, A. Schindeler, P. Valtchev, F. Dehghani, Dynamic flow and shear stress as key parameters for intestinal cells morphology and polarization in an organ-on-a-chip model, Biomed. Microdevices 23 (2021) 55. https://doi.org/10.1007/s10544-021-00591-y.
[36] D. Marrero, F. Pujol-Vila, D. Vera, G. Gabriel, X. Illa, A. Elizalde-Torrent, M. Alvarez, R. Villa, Gut-on-a-chip: Mimicking and monitoring the human intestine, Biosens. Bioelectron. 181 (2021) 113156–113156. https://doi.org/10.1016/j.bios.2021.113156.
[37] C.M. Leung, P. De Haan, K. Ronaldson-Bouchard, G.-A. Kim, J. Ko, H.S. Rho, Z. Chen, P. Habibovic, N.L. Jeon, S. Takayama, M.L. Shuler, G. Vunjak-Novakovic, O. Frey, E. Verpoorte, Y.-C. Toh, A guide to the organ-on-a-chip, Nat. Rev. Methods Primer 2 (2022) 33. https://doi.org/10.1038/s43586-022-00118-6.
[38] D.E. Ingber, Human organs-on-chips for disease modelling, drug development and personalized medicine, Nat. Rev. Genet. 23 (2022) 467–491. https://doi.org/10.1038/s41576-022-00466-9.
[39] L.A. Low, C. Mummery, B.R. Berridge, C.P. Austin, D.A. Tagle, Organs-on-chips: into the next decade, Nat. Rev. Drug Discov. 20 (2021) 345–361. https://doi.org/10.1038/s41573-020-0079-3.
[40] A.E. Ongaro, D. Di Giuseppe, A. Kermanizadeh, A. Miguelez Crespo, A. Mencattini, L. Ghibelli, V. Mancini, K.L. Wlodarczyk, D.P. Hand, E. Martinelli, V. Stone, N. Howarth, V. La Carrubba, V. Pensabene, M. Kersaudy-Kerhoas, Polylactic is a Sustainable, Low Absorption, Low Autofluorescence Alternative to Other Plastics for Microfluidic and Organ-on-Chip Applications, Anal. Chem. 92 (2020) 6693–6701. https://doi.org/10.1021/acs.analchem.0c00651.
[41] C.M. Leung, P. De Haan, K. Ronaldson-Bouchard, G.-A. Kim, J. Ko, H.S. Rho, Z. Chen, P. Habibovic, N.L. Jeon, S. Takayama, M.L. Shuler, G. Vunjak-Novakovic, O. Frey, E. Verpoorte, Y.-C. Toh, A guide to the organ-on-a-chip, Nat. Rev. Methods Primer 2 (2022) 33. https://doi.org/10.1038/s43586-022-00118-6.
[42] M.Z.A. Zulkifli, D. Nordin, N. Shaari, S.K. Kamarudin, Overview of Electrospinning for Tissue Engineering Applications, Polymers 15 (2023). https://doi.org/10.3390/polym15112418.
[43] M. Radisic, P. Loskill, Beyond PDMS and membranes: New materials for organ-on-a-chip devices, ACS Biomater. Sci. Eng. 7 (2021) 2861–2863. https://doi.org/10.1021/acsbiomaterials.1c00831.
[44] Q. Ramadan, M. Zourob, Organ-on-a-chip engineering: Toward bridging the gap between lab and industry., Biomicrofluidics 14 (2020) 041501. https://doi.org/10.1063/5.0011583.
[45] C. Matellan, A.E. Del Río Hernández, Cost-effective rapid prototyping and assembly of poly(methyl methacrylate) microfluidic devices, Sci. Rep. 8 (2018). https://doi.org/10.1038/s41598-018-25202-4.

[46] A. Liga, J.A.S. Morton, M. Kersaudy-Kerhoas, Safe and cost-effective rapid-prototyping of multilayer PMMA microfluidic devices, Microfluid. Nanofluidics 20 (2016). https://doi.org/10.1007/s10404-016-1823-1.
[47] J. Chuchuy, J. Rogal, T. Ngo, K. Stadelmann, L. Antkowiak, K. Achberger, S. Liebau, K. Schenke-Layland, P. Loskill, Integration of electrospun membranes into low-absorption thermoplastic organ-on-chip, ACS Biomater. Sci. Eng. 7 (2021) 3006–3017. https://doi.org/10.1021/acsbiomaterials.0c01062.
[48] H.-G. Yi, H. Lee, D.-W. Cho, 3D Printing of Organs-On-Chips, Bioengineering 4 (2017) 10. https://doi.org/10.3390/bioengineering4010010.
[49] V. Carvalho, I. Gonçalves, T. Lage, R.O. Rodrigues, G. Minas, S.F.C.F. Teixeira, A.S. Moita, T. Hori, H. Kaji, R.A. Lima, 3D Printing Techniques and Their Applications to Organ-on-a-Chip Platforms: A Systematic Review, Sensors 21 (2021). https://doi.org/10.3390/s21093304.
[50] J. Meneses, F. Conceição, A.D. Van Der Meer, S. De Wit, L. Moreira Teixeira, Guiding organs-on-chips towards applications: a balancing act between integration of advanced technologies and standardization, Front. Lab Chip Technol. 3 (2024) 1376964. https://doi.org/10.3389/frlct.2024.1376964.
[51] D.R. Reyes, M.B. Esch, L. Ewart, R. Nasiri, A. Herland, K. Sung, M. Piergiovanni, C. Lucchesi, J.T. Shoemaker, J. Vukasinovic, H. Nakae, J. Hickman, K. Pant, A. Taylor, N. Heinz, N. Ashammakhi, From animal testing to in vitro systems: advancing standardization in microphysiological systems, Lab. Chip 24 (2024) 1076–1087. https://doi.org/10.1039/d3lc00994g.
[52] F. Lopresti, F. Carfì Pavia, I. Vitrano, M. Kersaudy-Kerhoas, V. Brucato, V. La Carrubba, Effect of hydroxyapatite concentration and size on morpho-mechanical properties of PLA-based randomly oriented and aligned electrospun nanofibrous mats, J. Mech. Behav. Biomed. Mater. 101 (2020). https://doi.org/10.1016/j.jmbbm.2019.103449.
[53] F. Lopresti, I. Keraite, A.E. Ongaro, N.M. Howarth, V. La Carrubba, M. Kersaudy-Kerhoas, Engineered membranes for residual cell trapping on microfluidic blood plasma separation systems. A comparison between porous and nanofibrous membranes, Membranes 11 (2021). https://doi.org/10.3390/membranes11090680.
[54] M. Testa, M. Gaggianesi, C. D'Accardo, G. Porcelli, A. Turdo, C. Di Marco, B. Patella, S. Di Franco, C. Modica, S. Di Bella, F. Lopresti, G. Stassi, V. La Carrubba, M. Todaro, A Novel Tumor on Chip Mimicking the Breast Cancer Microenvironment for Dynamic Drug Screening, Int. J. Mol. Sci. 26 (2025). https://doi.org/10.3390/ijms26031028.
[55] M. Testa, M. Loria, F. Lopresti, C. Marco, M. Kersaudy-Kerhoas, F. Bucchieri, M. Pucci, E. Costanzo, S. Scilabra, R. Alessandro, S. Fontana, V. La Carrubba, Rapid prototyping of multicompartment Liver-on-Chip for dynamic administration of tumour derived vesicles within an electrospun scaffold, Lab. Chip 25 (2025). https://doi.org/10.1039/D5LC00353A.
[56] I.R.G. Ogilvie, V.J. Sieben, C.F.A. Floquet, R. Zmijan, M.C. Mowlem, H. Morgan, Reduction of surface roughness for optical quality microfluidic devices in PMMA and COC, J. Micromechanics Microengineering 20 (2010) 065016. https://doi.org/10.1088/0960-1317/20/6/065016.
[57] F. Lopresti, I. Keraite, A.E. Ongaro, N.M. Howarth, V. La Carrubba, M. Kersaudy-Kerhoas, Engineered Membranes for Residual Cell Trapping on Microfluidic Blood Plasma Separation Systems: A Comparison between Porous and Nanofibrous Membranes, Membranes 11 (2021). https://doi.org/10.3390/membranes11090680.
[58] P. Picone, E. Muscolino, A. Girgenti, M. Testa, D. Giacomazza, C. Dispenza, D. Nuzzo, Mitochondria embedded in degalactosylated xyloglucan hydrogels to improve

mitochondrial transplantation, Carbohydr. Polym. Technol. Appl. 8 (2024). https://doi.org/10.1016/j.carpta.2024.100543.
[59] F. Lopresti, S. Campora, S. Rigogliuso, A. Nicosia, A. Lo Cicero, C. Di Marco, S. Tornabene, G. Ghersi, V. La Carrubba, Improvement of Osteogenic Differentiation of Mouse Pre-Osteoblastic MC3T3-E1 Cells on Core–Shell Polylactic Acid/Chitosan Electrospun Scaffolds for Bone Defect Repair, Int. J. Mol. Sci. 25 (2024). https://doi.org/10.3390/ijms25052507.
[60] M. Testa, M. Gaggianesi, C. D'Accardo, G. Porcelli, A. Turdo, C. Di Marco, B. Patella, S. Di Franco, C. Modica, S. Di Bella, F. Lopresti, G. Stassi, V. La Carrubba, M. Todaro, A Novel Tumor on Chip Mimicking the Breast Cancer Microenvironment for Dynamic Drug Screening, Int. J. Mol. Sci. 26 (2025). https://doi.org/10.3390/ijms26031028.
[61] A.M. El-hadi, F.Y. Al-Jabri, Influence of Electrospinning Parameters on Fiber Diameter and Mechanical Properties of Poly(3-Hydroxybutyrate) (PHB) and Polyanilines (PANI) Blends, Polym. 2016 Vol 8 Page 97 8 (2016) 97–97. https://doi.org/10.3390/POLYM8030097.
[62] J. Izdebska-Podsiadły, P. Trokowska, E. Dörsam, Aging of Polylactide Films Exposed to Plasma—Hydrophobic Recovery and Selected Application Properties, Appl. Sci. 13 (2023) 2751–2751.
[63] F. Lopresti, S. Campora, S. Rigogliuso, A. Nicosia, A. Lo Cicero, C. Di Marco, S. Tornabene, G. Ghersi, V. La Carrubba, Improvement of Osteogenic Differentiation of Mouse Pre-Osteoblastic MC3T3-E1 Cells on Core–Shell Polylactic Acid/Chitosan Electrospun Scaffolds for Bone Defect Repair, Int. J. Mol. Sci. 25 (2024). https://doi.org/10.3390/ijms25052507.
[64] F. Carrasco, P. Pagès, J. Gámez-Pérez, O.O. Santana, M.L. Maspoch, Processing of poly(lactic acid): Characterization of chemical structure, thermal stability and mechanical properties, Polym. Degrad. Stab. 95 (2010) 116–125. https://doi.org/10.1016/j.polymdegradstab.2009.11.045.
[65] A. Porfyris, S. Vasilakos, C. Zotiadis, C. Papaspyrides, K. Moser, L. Van der Schueren, G. Buyle, S. Pavlidou, S. Vouyiouka, Accelerated ageing and hydrolytic stabilization of poly(lactic acid) (PLA) under humidity and temperature conditioning, Polym. Test. 68 (2018) 315–332. https://doi.org/10.1016/j.polymertesting.2018.04.018.
[66] R.A. Behmer Hansen, X. Wang, G. Kaw, V. Pierre, S.E. Senyo, Accounting for Material Changes in Decellularized Tissue with Underutilized Methodologies, BioMed Res. Int. 2021 (2021) 6696295. https://doi.org/10.1155/2021/6696295.
[67] X. Huang, Z. Huang, W. Gao, W. Gao, R. He, Y. Li, R. Crawford, Y. Zhou, L. Xiao, Y. Xiao, Current Advances in 3D Dynamic Cell Culture Systems, Gels 8 (2022) 829. https://doi.org/10.3390/gels8120829.
[68] G. Si, X. Chen, Y. Li, X. Yuan, Exosomes promote pre-metastatic niche formation in colorectal cancer, Heliyon 10 (2024) e27572. https://doi.org/10.1016/j.heliyon.2024.e27572.
[69] 65_109, (n.d.).
[70] J. Chuchuy, J. Rogal, T. Ngo, K. Stadelmann, L. Antkowiak, K. Achberger, S. Liebau, K. Schenke-Layland, P. Loskill, Integration of electrospun membranes into low-absorption thermoplastic organ-on-chip, ACS Biomater. Sci. Eng. 7 (2021) 3006–3017. https://doi.org/10.1021/acsbiomaterials.0c01062.
[71] C.H. Beckwitt, A.M. Clark, S. Wheeler, D.L. Taylor, D.B. Stolz, L. Griffith, A. Wells, Liver 'organ on a chip,' Exp. Cell Res. 363 (2018) 15–25. https://doi.org/10.1016/j.yexcr.2017.12.023.
[72] K.M. Kim, Y.J. Choi, J.-H. Hwang, A.R. Kim, H.J. Cho, E.S. Hwang, J.Y. Park, S.-H. Lee, J.-H. Hong, Shear stress induced by an interstitial level of slow flow increases

the osteogenic differentiation of mesenchymal stem cells through TAZ activation, PloS One 9 (2014) e92427–e92427.
[73] I. Kaur, A. Vasudevan, P. Rawal, D.M. Tripathi, S. Ramakrishna, S. Kaur, S.K. Sarin, Primary Hepatocyte Isolation and Cultures: Technical Aspects, Challenges and Advancements, Bioengineering 10 (2023). https://doi.org/10.3390/bioengineering10020131.
[74] T.L. Place, F.E. Domann, A.J. Case, Limitations of oxygen delivery to cells in culture: An underappreciated problem in basic and translational research, Free Radic. Biol. Med. 113 (2017) 311–322. https://doi.org/10.1016/j.freeradbiomed.2017.10.003.
[75] L.D. Buck, S.W. Inman, I. Rusyn, L.G. Griffith, Co-regulation of primary mouse hepatocyte viability and function by oxygen and matrix, Biotechnol. Bioeng. 111 (2014) 1018–1027. https://doi.org/10.1002/bit.25152.
[76] J. Chuchuy, J. Rogal, T. Ngo, K. Stadelmann, L. Antkowiak, K. Achberger, S. Liebau, K. Schenke-Layland, P. Loskill, Integration of electrospun membranes into low-absorption thermoplastic organ-on-chip, ACS Biomater. Sci. Eng. 7 (2021) 3006–3017. https://doi.org/10.1021/acsbiomaterials.0c01062.
[77] E. Capuana, M. Testa, C.D. Marco, F. Lopresti, V. La Carrubba, Impact of Fiber Orientation in Electrospun PLA Scaffolds on Fluid Dynamics in a Custom Microfluidic Device, Adv. Healthc. Mater. (2025). https://doi.org/10.1002/adhm.202500378.
[78] I. Kaur, A. Vasudevan, P. Rawal, D.M. Tripathi, S. Ramakrishna, S. Kaur, S.K. Sarin, Primary Hepatocyte Isolation and Cultures: Technical Aspects, Challenges and Advancements, Bioengineering 10 (2023) 131. https://doi.org/10.3390/bioengineering10020131.
[79] M. Pucci, M. Moschetti, O. Urzì, M. Loria, A. Conigliaro, M.A. Di Bella, R. Crescitelli, R. Olofsson Bagge, A. Gallo, M.F. Santos, C. Puglisi, S. Forte, A. Lorico, R. Alessandro, S. Fontana, Colorectal cancer-derived small extracellular vesicles induce TGFβ1-mediated epithelial to mesenchymal transition of hepatocytes, Cancer Cell Int. 23 (2023). https://doi.org/10.1186/s12935-023-02916-8.
[80] P. Picone, E. Muscolino, A. Girgenti, M. Testa, D. Giacomazza, C. Dispenza, D. Nuzzo, Mitochondria embedded in degalactosylated xyloglucan hydrogels to improve mitochondrial transplantation, Carbohydr. Polym. Technol. Appl. 8 (2024) 100543. https://doi.org/10.1016/j.carpta.2024.100543.
[81] M. Todaro, M. Gaggianesi, V. Catalano, A. Benfante, F. Iovino, M. Biffoni, T. Apuzzo, I. Sperduti, S. Volpe, G. Cocorullo, G. Gulotta, F. Dieli, R. De Maria, G. Stassi, CD44v6 Is a Marker of Constitutive and Reprogrammed Cancer Stem Cells Driving Colon Cancer Metastasis, Cell Stem Cell 14 (2014) 342–356. https://doi.org/10.1016/j.stem.2014.01.009.
[82] A. Turdo, M. Gaggianesi, S. Di Franco, V. Veschi, C. D'Accardo, G. Porcelli, M. Lo Iacono, I. Pillitteri, F. Verona, G. Militello, A. Zippo, V. Poli, L. Fagnocchi, S. Beyes, S. Stella, R. Lattanzio, N. Faldetta, V.L. Lentini, R. Porcasi, G. Pistone, M.R. Bongiorno, G. Stassi, R. De Maria, M. Todaro, Effective targeting of breast cancer stem cells by combined inhibition of Sam68 and Rad51, Oncogene 41 (2022) 2196–2209. https://doi.org/10.1038/s41388-022-02239-4.
[83] A. Turdo, M. Gaggianesi, S. Di Franco, V. Veschi, C. D'Accardo, G. Porcelli, M. Lo Iacono, I. Pillitteri, F. Verona, G. Militello, others, Effective targeting of breast cancer stem cells by combined inhibition of Sam68 and Rad51, Oncogene 41 (2022) 2196–2209.
[84] M. Gaggianesi, A. Turdo, A. Chinnici, E. Lipari, T. Apuzzo, A. Benfante, I. Sperduti, S. Di Franco, S. Meraviglia, E. Lo Presti, F. Dieli, V. Caputo, G. Militello, S. Vieni, G. Stassi, M. Todaro, IL4 Primes the Dynamics of Breast Cancer Progression

via DUSP4 Inhibition, Cancer Res. 77 (2017) 3268–3279. https://doi.org/10.1158/0008-5472.CAN-16-3126.
[85] M. Gaggianesi, S. Di Franco, V.D. Pantina, G. Porcelli, C. D'Accardo, F. Verona, V. Veschi, L. Colarossi, N. Faldetta, G. Pistone, M.R. Bongiorno, M. Todaro, G. Stassi, Messing Up the Cancer Stem Cell Chemoresistance Mechanisms Supported by Tumor Microenvironment, Front. Oncol. 11 (2021) 702642. https://doi.org/10.3389/fonc.2021.702642.
[86] Y. Liu, M.L. Burness, R. Martin-Trevino, J. Guy, S. Bai, R. Harouaka, M.D. Brooks, L. Shang, A. Fox, T.K. Luther, RAD51 mediates resistance of cancer stem cells to PARP inhibition in triple-negative breast cancer, Clin. Cancer Res. 23 (2017) 514–522.
[87] X.-L. Dai, B.-W. Pang, W.-T. Lv, J.-F. Zhen, L. Gao, C.-W. Li, J. Xiong, T.-B. Lu, J.-M. Chen, Improving the physicochemical and pharmacokinetic properties of olaparib through cocrystallization strategy, Int. J. Pharm. 647 (2023) 123497. https://doi.org/10.1016/j.ijpharm.2023.123497.
[88] A. Zilberman, R.C. Cornelison, Microphysiological models of the central nervous system with fluid flow, Brain Res. Bull. 174 (2021) 72–83. https://doi.org/10.1016/j.brainresbull.2021.05.015.
[89] L.A. Ray, J.J. Heys, Fluid flow and mass transport in brain tissue, Fluids 4 (2019) 196–196.
[90] Z. Liu, G. Song, C. Zou, G. Liu, W. Wu, T. Yuan, X. Liu, Acrylamide induces mitochondrial dysfunction and apoptosis in BV-2 microglial cells, Free Radic. Biol. Med. 84 (2015) 42–53.
[91] Z. Xun, D.-Y. Lee, J. Lim, C.A. Canaria, A. Barnebey, S.M. Yanonne, C.T. McMurray, Retinoic acid-induced differentiation increases the rate of oxygen consumption and enhances the spare respiratory capacity of mitochondria in SH-SY5Y cells, Mech. Ageing Dev. 133 (2012) 176–185. https://doi.org/10.1016/j.mad.2012.01.008.
[92] E. Capuana, M. Testa, C.D. Marco, F. Lopresti, V. La Carrubba, Impact of Fiber Orientation in Electrospun PLA Scaffolds on Fluid Dynamics in a Custom Microfluidic Device, Adv. Healthc. Mater. (2025). https://doi.org/10.1002/adhm.202500378.
[93] F. Yang, R. Murugan, S. Wang, S. Ramakrishna, Electrospinning of nano/micro scale poly(l-lactic acid) aligned fibers and their potential in neural tissue engineering, Biomaterials 26 (2005). https://doi.org/10.1016/j.biomaterials.2004.06.051.
[94] H. Nakanishi, J. Ni, S. Nonaka, Y. Hayashi, Microglial circadian clock regulation of microglial structural complexity, dendritic spine density and inflammatory response, Neurochem. Int. 142 (2021) 104905–104905. https://doi.org/10.1016/j.neuint.2020.104905.
[95] C.D. Katsetos, A. Legido, E. Perentes, S.J. Mörk, Class III β-Tubulin Isotype: A Key Cytoskeletal Protein at the Crossroads of Developmental Neurobiology and Tumor Neuropathology, J. Child Neurol. 18 (2003) 851–866. https://doi.org/10.1177/088307380301801205.
[96] P. Binarová, J. Tuszynski, Tubulin: Structure, Functions and Roles in Disease, Cells 8 (2019). https://doi.org/10.3390/cells8101294.
[97] P.T. Williams, Quantile-Dependent Expressivity of Serum Interleukin-6 Concentrations as a Possible Explanation of Gene-Disease Interactions, Gene-Environment Interactions, and Pharmacogenetic Effects, Inflammation 45 (2022) 1059–1075. https://doi.org/10.1007/s10753-021-01601-0.
[98] A. Harada, J. Teng, Y. Takei, K. Oguchi, N. Hirokawa, MAP2 is required for dendrite elongation, PKA anchoring in dendrites, and proper PKA signal transduction, J. Cell Biol. 158 (2002) 541-549-541–549. https://doi.org/10.1083/jcb.200110134.

[99] Y. Sasaki, K. Ohsawa, H. Kanazawa, S. Kohsaka, Y. Imai, Iba1 Is an Actin-Cross-Linking Protein in Macrophages/Microglia, Biochem. Biophys. Res. Commun. 286 (2001) 292–297. https://doi.org/10.1006/bbrc.2001.5388.

[100] J. Lier, W.J. Streit, I. Bechmann, Beyond Activation: Characterizing Microglial Functional Phenotypes, Cells 10 (2021). https://doi.org/10.3390/cells10092236.

[101] P. Picone, F.S. Palumbo, F. Cancilla, A. Girgenti, P. Cancemi, V. Muccilli, A.D. Francesco, M. Cimino, C. Cipollina, M. Soligo, L. Manni, G. Sferrazza, L. Scalisi, D. Nuzzo, Brain biodistribution of myelin nanovesicles with targeting potential for multiple sclerosis, Acta Biomater. 187 (2024) 352–365. https://doi.org/10.1016/j.actbio.2024.08.016.

[102] P. Picone, F.S. Palumbo, S. Federico, G. Pitarresi, G. Adamo, A. Bongiovanni, A. Chaves, P. Cancemi, V. Muccilli, V. Giglio, V. Vetri, S. Anselmo, G. Sancataldo, V. Di Liberto, D. Nuzzo, Nano-structured myelin: new nanovesicles for targeted delivery to white matter and microglia, from brain-to-brain, Mater. Today Bio 12 (2021) 100146–100146. https://doi.org/10.1016/j.mtbio.2021.100146.